Mechanical and Regenerative Braking Integration for a Hybrid Electric Vehicle

by

Steven M. DeMers

A thesis
presented to the University of Waterloo
in fulfillment of the
thesis requirement for the degree of
Master of Applied Science
in
Mechanical Engineering

Waterloo, Ontario, Canada, August 2008

I hereby declare that I am the sole author of this thesis. This is a true copy of the thesis, including any required final revisions, as accepted by my examiners.

I understand that my thesis may be made electronically available to the public.

Abstract

Hybrid electric vehicle technology has become a preferred method for the automotive industry to reduce environmental impact and fuel consumption of their vehicles. Hybrid electric vehicles accomplish these reductions through the use of multiple propulsion systems, namely an electric motor and internal combustion engine, which allow the elimination of idling, operation of the internal combustion engine in a more efficient manner and the use of regenerative braking. However, the added cost of the hybrid electric system has hindered the sales of these vehicles.

A more cost effective design of an electro-hydraulic braking system is presented. The system electro-mechanically controlled the boost force created by the brake booster independently of the driver braking force and with adequate time response. The system allowed for the blending of the mechanical and regenerative braking torques in a manner transparent to the driver and allowed for regenerative braking to be conducted efficiently.

A systematic design process was followed, with emphasis placed on demonstrating conceptual design feasibility and preliminary design functionality using virtual and physical prototyping. The virtual and physical prototypes were then used in combination as a powerful tool to validate and develop the system. The role of prototyping in the design process is presented and discussed.

Through the experiences gained by the author during the design process, it is recommended that students create physical prototypes to enhance their educational experience. These experiences are evident throughout the thesis presented.

Acknowledgements

I would like to thank Drs. Stephan Lambert and Magdy Salama, for without their help, this thesis would not be possible. It was a pleasure to work under the supervision of Dr. Lambert whose guidance and patience were greatly appreciated during my graduate studies.

I would like to acknowledge the AUTO21 Network of Centres of Excellence for funding this project along with the Natural Sciences and Engineering Research Council of Canada (NSERC) for all of their support. This funding allowed me to pursue my educational goals which otherwise would not have been possible.

Lastly, I would like to thank my fellow University of Waterloo researchers, Simon Stark and Samy Ghania, for all their help during this project and my fellow AUTO21 researchers from the University of Windsor and the University of Ontario Institute of Technology.

Contents

List of Tables

List of Figures

Chapter 1

Introduction

1.1 Modern Hybrid Electric Vehicles

With rising gas prices and the overwhelming concern for the environment, consumers and the government have forced the automotive industry to start producing more fuel efficient vehicles with less environmental impact. One promising method that is currently being implemented is the hybrid electric vehicle.

Hybrid vehicles are defined as vehicles that have two or more power sources [25]. There are a large number of possible variations, but the most common layout of hybrid vehicles today combines the power of an internal combustion engine (ICE) with the power of an electric motor and energy storage system (ESS). These vehicles are often referred to as hybrid electric vehicles (HEV's) [25]. These two power sources are used in conjunction to optimize the efficiency and performance of the vehicle, which in turn will increase fuel economy and reduce vehicle emissions, all while delivering the performance the consumer requires. In 1997, the Toyota Prius became the first hybrid vehicle introduced into mass production in Japan. It took another three years for the first mass produced hybrid vehicle, the Honda Insight, to be introduced into the North American market. The release of the Honda Insight was closely followed by the release of the Toyota Prius in North America a couple of months later [35].

Hybrid electric vehicles have the distinct advantage of regenerative braking. The electric motor, normally used for propulsion, can be used as a generator to convert kinetic energy of the vehicle back into electrical energy during braking, rather than wasting energy as heat. This electrical energy can then be stored in an ESS (e.g. batteries or ultracapacitors) and later released to propel the vehicle using the electric motor.

This process becomes even more important when considering the energy density of batteries compared to gasoline or diesel fuel. Energy density is defined as the amount of energy stored in a system per unit volume or mass [44]. To illustrate this point, 4 kilograms (4.5 litres) of gasoline will typically give a motor vehicle a range of 50 kilometres. To store the same amount of useful electric energy it requires a lead acid battery with a mass of about 270 kilograms [25]. This demonstrates the need for efficient regenerative braking to store electrical energy during driving, which in turn will keep the mass of the energy storage system down and improve the performance and efficiency of the HEV.

1.2 Project Scope - AUTO21 E03 RGB

AUTO21, a Network of Centres of Excellence, is focused on improving the global competitiveness of the Canadian automotive industry. This network is funded by the Government of Canada through the Networks of Centres of Excellence (NCE) program. Currently, there are over 265 top researchers working at more than 42 academic institutions and labs around the world [38]. AUTO21 projects are distributed across six research themes:

- Theme A - Health, Safety and Injury Prevention
- Theme B - Societal Issues
- Theme C - Materials and Manufacturing
- Theme D - Powertrains, Fuels and Emissions
- Theme E - Design Processes

- Theme F - Intelligent Systems and Sensors

AUTO21 E03 RGB was a Theme E project with collaboration from four different universities (University of British Columbia, University of Ontario Institute of Technology, University of Waterloo and the University of Windsor). The purpose of this project is to develop and optimize the regenerative braking system utilizing ultracapacitors of a hybrid electric vehicle in order to improve efficiency, along with developing active safety systems for the vehicle. Ultracapacitors were selected because of their high power density which allows them to store energy at an extremely high rate. These high power events are typically found during regenerative braking which allows ultracapacitors to store as much electrical energy as possible. If batteries were used the current would have to be limited during large regenerative braking events wasting energy that could be used to later propel the vehicle. A 2004 Chrysler Pacifica was graciously donated by Chrysler LLC with the end objective of being converted into a HEV and acting as a testing platform for regenerative braking.

1.3 Research Scope - Regenerative Braking Systems

The scope of the research presented is to create a low cost regenerative braking system to be used on future economical hybrid vehicles to study the interaction between regenerative and mechanical braking of the system. This system should be able to control the combination of both regenerative and mechanical braking torque depending on driver demand and should be able to do so smoothly and safely. Controlling the regenerative braking torque can be done using control algorithms and vector control for induction motors. However, controlling the mechanical braking torque independently of the driver pedal force, while maintaining proper safety back-ups, proved to be more of a challenge. To overcome this problem, a system was developed that would attenuate the pressure in the brake booster in order to control the amount of mechanical torque developed by the braking system.

Chapter 2

Background Information

2.1 Hybrid Electric Vehicle Overview

Hybrid vehicles have emerged as one of the short term solutions for reducing vehicle emissions and improving fuel economy. Over the past 10 years almost all of the major automotive companies have developed and released for sale their own hybrid electric vehicles to the public. Table 2.1 summarizes the current hybrid electric vehicles sold in North America.

The popularity of hybrid electric vehicles has grown considerably since the turn of the century. With enormous pressure to become more environmentally friendly and with unpredictable gas prices, the sales of hybrid electric vehicles have increased dramatically in recent years. Figure 2.1 shows North American hybrid electric vehicle sales figures from 2000 to 2006.

2.1.1 Hybrid Configurations

For the past 100 years the objective of the hybrid has been to extend the range of electric vehicles and to overcome the problem of long recharging times [35]. There are three predominant hybrid electric vehicle configurations currently on the market today. These configurations are known as series hybrids, parallel hybrids and series/parallel hybrids.

Company	**Model**	**Vehicle Class**	**Hybrid Type**
Chevrolet	Tahoe	SUV	Full Hybrid
Ford	Escape	SUV	Full Hybrid
GMC	Silverado	Pickup Truck	Micro Hybrid
GMC	Sierra	Pickup Truck	Micro Hybrid
GMC	Yukon	SUV	Full Hybrid
Honda	Accord	Sedan	Mild Hybrid
Honda	Civic	Compact	Mild Hybrid
Lexus	RX 400h	SUV	Full Hybrid
Lexus	GS 450h	Sedan	Full Hybrid
Lexus	LS 600h L	Sedan	Full Hybrid
Mazda	Tribute	SUV	Full Hybrid
Mercury	Mariner	SUV	Full Hybrid
Saturn	Aura GreenLine	Compact	Micro Hybrid
Saturn	Vue GreenLine	SUV	Micro Hybrid
Toyota	Camry	Sedan	Full Hybrid
Toyota	Prius	Compact	Full Hybrid
Toyota	Highlander	SUV	Full Hybrid

Table 2.1: Available hybrid vehicles in North America (2007) [20] - see subsection 2.1.2 for definition of hybrid type

Each configuration has its advantages and disadvantages which will be discussed in the following sections.

Series Hybrids

In series hybrids the mechanical output from the internal combustion engine is used to drive a generator which produces electrical power that can be stored in the batteries or used to power an electric motor and drive the wheels. There is no direct mechanical connection between the engine and the driven wheels. Series hybrids tend to be used in high power systems such as large trucks or locomotives but can also be used for lower power

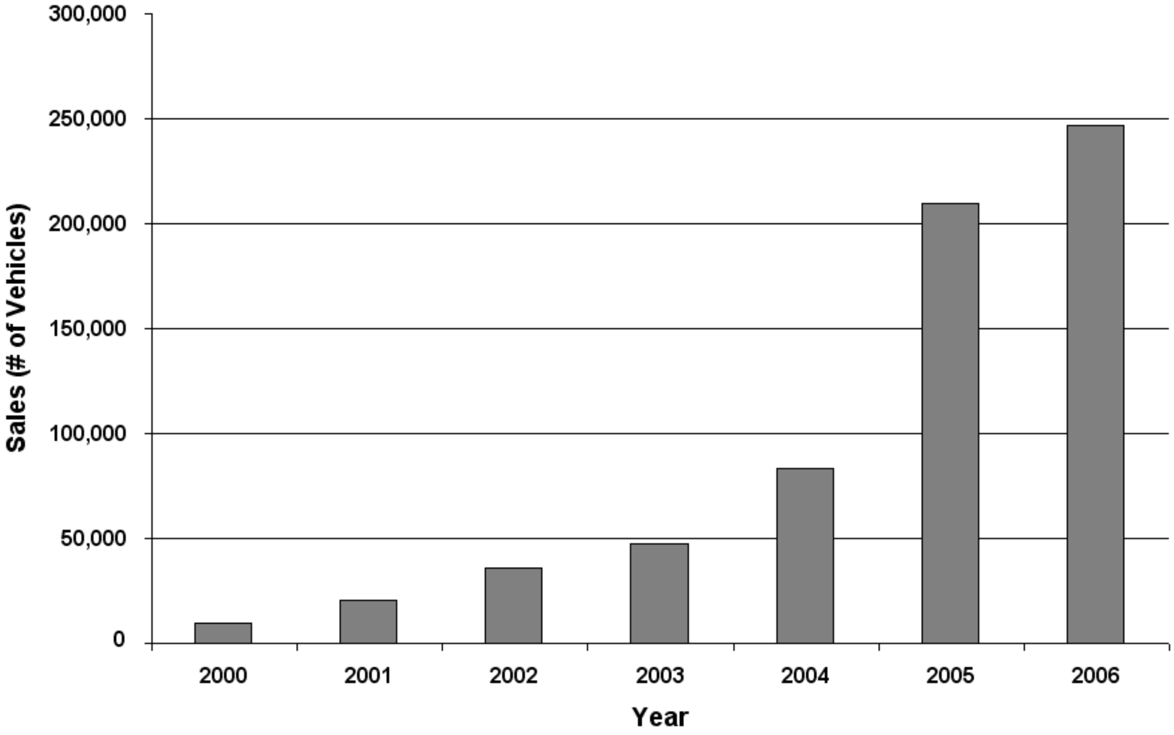

Figure 2.1: North American HEV sales figures (2000-2006) [2]

passenger vehicles [18]. The mechanically generated electrical power is combined with the power from the battery in an electronic controller. This controller then compares the driver demand with the vehicle speed and available torque from the electric motor to determine the amount of power required from each source to drive the vehicle. During braking, the controller also switches the power electronics to regenerative mode, and directs the power being regenerated to the batteries [55].

There are many advantages made possible by the arrangement described above. It is possible to run the ICE constantly at its most efficient operating point and share its electrical output between charging the battery and driving the electric motor. By operating the engine at its most efficient operating point, emissions can be greatly reduced and the most electrical power can be generated per volume of fuel. This configuration is also easier to implement into a vehicle because it is less complex which makes this method more cost effective.

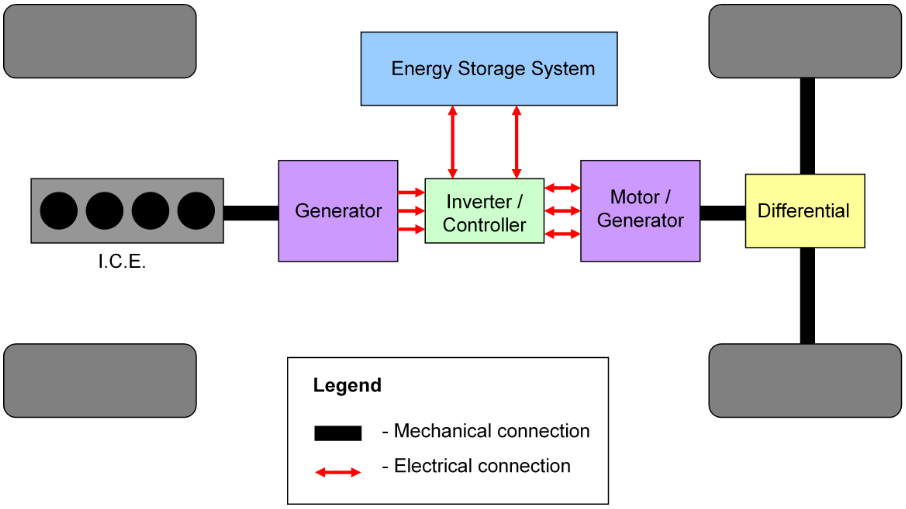

Figure 2.2: Series hybrid architecture [53]

Parallel Hybrids

In parallel hybrid configurations the mechanical energy output from the ICE is transmitted to a gearbox. In this gearbox the energy from the ICE can be mechanically combined with a second drive from an electric motor. The combined mechanical output is then used to drive the wheels [35]. In this configuration there is a direct connection between the engine and the driven wheels. As in series hybrids the controller compares the driver demand with the vehicle speed and output torque and determines the amount of power to be used from each source to meet the demand, while obtaining the best possible efficiency. A parallel hybrid also controls regenerative braking similarly to a series hybrid. Parallel hybrids are usually used in lower power electric vehicles in which both drives can be operated in parallel to provide higher performance [18].

There are a number of advantages of a parallel hybrid over a series hybrid. The most important advantage is that since only one conversion between electrical and mechanical power is made, efficiency will be much better than the series hybrid in which two conversions are required. Since the parallel hybrid has the ability to combine both the engine and electric motor powers simultaneously, smaller electric motors can be used without sacrificing performance, while getting the fuel consumption and emission reduction benefits. Lastly, parallel hybrids only need to operate the engine when the vehicle is moving and do not need a second generator to charge the batteries.

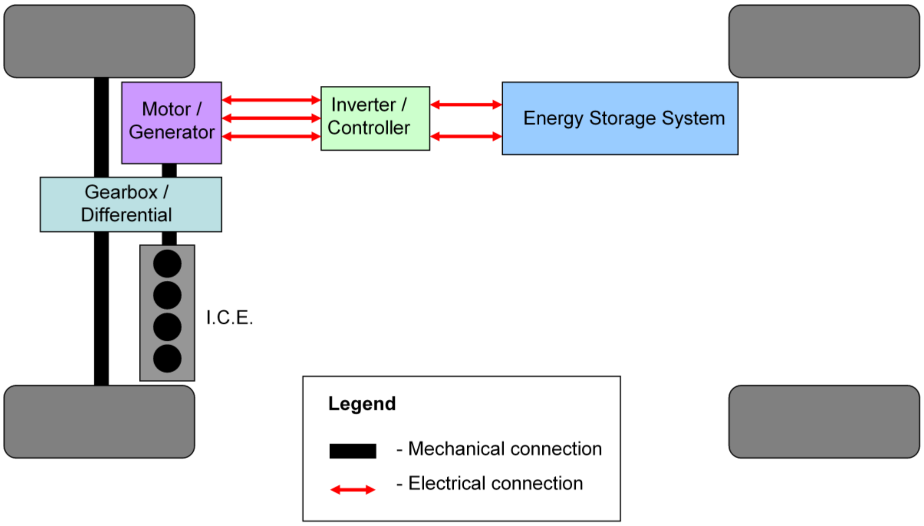

Figure 2.3: Parallel hybrid architecture [53]

Series/Parallel Hybrids

Combined hybrids have the features of both series and parallel configurations. They use a power split device to drive the wheels using dual sources of power (e.g. electric motor only, ICE only or a combination of both). While the added benefits of both series hybrids and parallel hybrids are achieved for this configuration, control algorithms become very complex because of the large number of driving possibilities available.

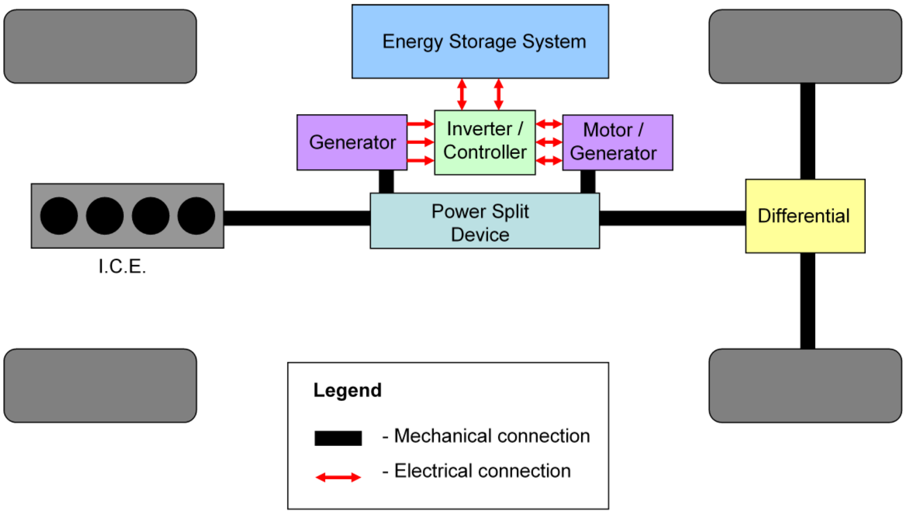

Figure 2.4: Series/parallel hybrid architecture [53]

2.1.2 Degree of Hybridization

Since most HEV's on the road today are either parallel or series/parallel, it is useful to define a variable called the 'degree of hybridization' to quantify the electrical power potential of these vehicles.

$$DOH = \frac{P_{em}}{P_{em} + P_{ice}} \tag{2.1}$$

The degree of hybridization ranges from (DOH = 0) for a conventional vehicle to (DOH = 1) for an all electric vehicle [25]. As the degree of hybridization increases, a smaller ICE can be used and operated closer to its optimum efficiency for a greater proportion of the time, which will decrease fuel consumption and emissions. The electric motor power is denoted by P_{em} and the internal combustion engine power is denoted by P_{ice}.

Micro Hybrid

Micro hybrids have the smallest degree of hybridization and usually consist of an integrated starter generator (ISG) connected to the engine crankshaft. The ISG allows the engine to be shut off during braking and idling to conserve fuel and then spins the crankshaft up to speed before fuel is injected during acceleration. The ISG also provides small amounts of assist to the ICE during acceleration and acts as a generator to charge the batteries during braking. Micro hybrids usually improve fuel economy by about 10 percent compared with non hybrids [53].

Mild Hybrid

Mild hybrids have a similar architecture to the micro hybrid except that the ISG is uprated in power to typically greater than 20 kW. However, the energy storage system is limited to less than 1 kWh [35]. Mild hybrids usually have a very short electric-only range capability but can provide a greater assist to the ICE during accelerations. The electrical components in a mild hybrid are more complex than a micro hybrid and play a greater role in the vehicle operation. Fuel economy can be improved by 20 to 25 percent with a mild hybrid over non hybrid vehicles [53].

Full Hybrid

Full hybrids do away with the ISG and replace it with a separate electric motor and alternator/starter that perform the same function. The electric motor has the ability to propel the vehicle alone, particularly in city (stop and go) driving. The energy storage system is upgraded to improve electric-only range capability and the engine is usually downsized to improve fuel economy and emissions. Full hybrids can achieve 40 to 45 percent fuel consumption reductions over non hybrids [53].

Plug-in Hybrid

Plug-in hybrids are very similar to full hybrids except that they have a much larger ESS that can be connected to an outside electrical utility source for charging. These vehicles use only the electric motor to propel the vehicle within the range of the batteries and then operate like full hybrids once the batteries have discharged to a predefined level.

2.1.3 Fundamentals of Regenerative Braking

One of the most important features of HEV's is their ability to recover significant amounts of braking energy. The electric motors can be controlled to operate as generators during braking to convert the kinetic energy of the vehicle into electrical energy that can be stored in the energy storage system and reused. However, the braking performance of a vehicle also greatly affects vehicle safety. In an emergency braking situation the vehicle must be stopped in the shortest possible distance and must be able to maintain control over the vehicle's direction. The latter requires control of brake force distribution to the wheels [12].

Generally, the braking torque required is much larger than the torque that an electric motor can produce [12]. Therefore, a mechanical friction braking system must coexist with the electrical regenerative braking. This coexistence demands proper design and control of both mechanical and electrical braking systems to ensure smooth, stable braking operations that will not adversely affect vehicle safety.

Energy Consumption in Braking

Braking a 1500 kg vehicle from 100 km/h to 0 km/h consumes about 0.16 kWh of energy based on Equation 2.2.

$$E = \frac{1}{2}mv^2 \tag{2.2}$$

If 25 percent of this energy could be recovered through regenerative braking techniques, then Equation 2.2 can be used to estimate that this energy could be used to accelerate the vehicle from 0 km/h to about 50 km/h, neglecting aerodynamic drag, mechanical friction and rolling resistance during both braking and accelerating. This also assumes that the generating and driving modes of the electric motor are 100% efficient. This suggests that the fuel economy of HEV's can be greatly increased when driving in urban centres where the driver is constantly braking and accelerating. Note that the amount of energy recovered is limited by the size of the electric motor and the rate of which energy can be transferred to the ESS.

2.1.4 Methods of Regenerative Braking

There are two basic regenerative braking methods used today. These methods are often referred to as parallel regenerative braking and series regenerative braking. Each of these braking strategies have advantages and disadvantages that will be discussed in this section.

Parallel Regenerative Braking

During parallel regenerative braking, both the electric motor and mechanical braking system always work in parallel (together) to slow the vehicle down (Figure 2.5a) [48]. Since mechanical braking cannot be controlled independently of the brake pedal force it is converting some of the vehicle's kinetic energy into heat instead of electrical energy. This is not the most efficient regenerative braking method. However, parallel regenerative braking does have the advantages of being simple and cost effective. For this method to be used, the mechanical braking system needs little modification and the control algorithms for the electric motor can be easily implemented into the vehicle. This method also has the added advantage of always having the mechanical braking system as a back-up in case of a failure of the regenerative braking system.

Series Regenerative Braking

During series regenerative braking the electric motor is solely used for braking. It is only when the motor or energy storage system can no longer accept more energy that the mechanical brakes are used [48]. This method requires that the mechanical braking torque be controlled independently of the brake pedal force and has the advantage of being the most efficient by converting as much of the vehicle's kinetic energy into electrical energy (Figure 2.5b). The downfall of this method is that it brings many costs and complexities into the system. For this method to function properly a brake-by-wire system has to be developed which either uses an electro-hydraulic brake (EHB) or an electro-mechanical brake (EMB). Both of these types of brakes require brake pedal simulators and redesigned brake systems which can become costly. Since these systems are brake-by-wire there are also many redundancies required with sensors, processors and wiring for safety which add to the complexity of the system.

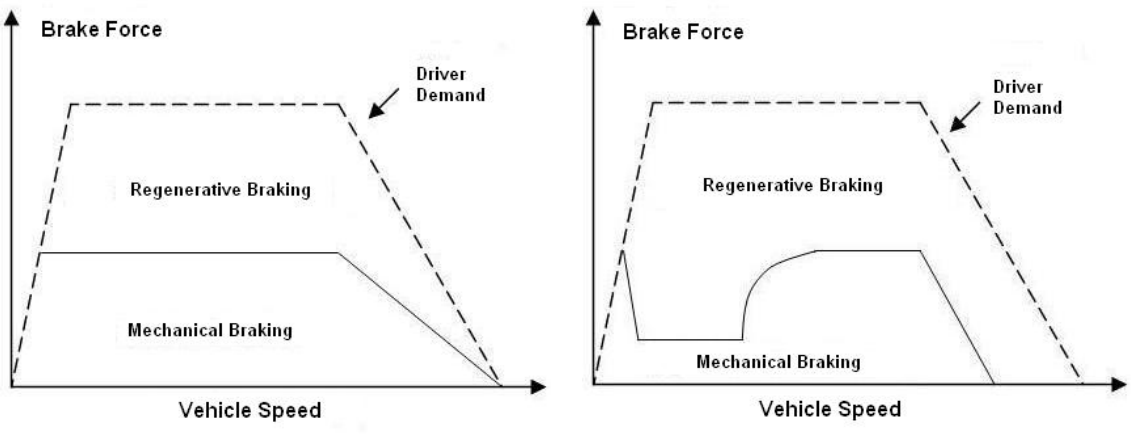

(a) Parallel regenerative braking strategy [26] (b) Series regenerative braking strategy [36]

Figure 2.5: Regenerative braking strategies

2.1.5 Current Regenerative Braking Systems

The current regenerative braking system in most HEV's (e.g. Toyota Prius) is the more costly electro-hydraulic braking (EHB) system. This system uses a brake pedal simulator, which is separate from the hydraulic braking circuit, to establish driver braking demand. The braking demand is then proportioned into a regenerative and mechanical braking demand. The mechanical braking demand is then sent to a system that contains a high pressure hydraulic pump, accumulator and proportional control valves. The proportional control valves allow the brake line fluid to flow to each wheel at predefined pressures determined by the braking demand.

2.2 Standard Automotive Braking System

The brake system for passenger vehicles has changed very little in the past eighty years [17]. It was decided that hydraulic braking systems would be an efficient method of transmitting the driver's foot-pedal force to individual brakes at each wheel. The driver's force is converted to a hydraulic pressure which is then transmitted to each wheel brake where it is then converted into torque to stop the rotation of the wheels.

Heisler states, "The purpose of the brakes is to retard or stop the vehicle in motion by converting the kinetic energy of the moving vehicle into rotational frictional torque at the brake-shoes or brake-pads. This energy will then change into heat... Hence the brakes should be able to dissipate large quantities of heat without undue temperature rise and should be rigid enough to absorb the large braking torques encountered" [17].

2.2.1 Brake Pedal

The brake pedal acts as a second class lever and is used to transmit force from the driver's foot to slow or stop the vehicle. The brake pedal lever usually multiplies the driver applied force by approximately four times which helps reduce the amount of effort the driver needs to stop the vehicle, reducing fatigue [17]. The brake pedal also acts as a feedback to the driver so they can safely control the amount of braking during slippery conditions. Also, a 'soft' feeling brake pedal can warn the driver of a possible failure in the brake system before it occurs.

2.2.2 Brake Booster

The purpose of the brake booster is to increase the pedal force applied by the driver to make braking more comfortable and safer for the driver. The brake booster has the ability to increase the pedal force anywhere from two to four times depending on the size of the diaphragm [14]. The brake booster is located between the brake pedal and the master cylinder.

The brake booster consists of a body which is divided by a diaphragm into a constant pressure chamber and a dynamic (or variable) pressure chamber. There is a control valve mechanism that regulates the pressure inside the dynamic pressure chamber. A valve operating rod attached to the brake pedal controls the valve mechanism and a pushrod connects the brake booster with the master cylinder (Figure 2.6).

The brake booster operates using a pressure differential between the constant pressure chamber and the dynamic pressure chamber. During non-braking events, both pressure chambers are under the same vacuum created by the throttling of the air in the intake manifold which is usually between 40 and 60 kPa absolute. This produces no pressure differential. During braking events, the pedal pushes the operating rod causing a valve to open, introducing atmospheric air into the dynamic pressure chamber. This causes a higher pressure on the dynamic pressure side of the diaphragm compared to the constant pressure side. This pressure differential then forces the pushrod attached to the diaphragm into the master cylinder causing the boost from the brake pedal force.

Brake Booster Operation

There are three main conditions during brake booster operation: the apply, hold and release stages. There is also a stage in which the brake booster is not operating, occurring when the brakes are not applied [1].

Brakes Not Applied

When the brakes are not applied, the air valve connected to the valve operating rod is pulled to the right by the air valve return spring. The control valve is pushed to the left by the control valve spring causing the air valve to contact the control valve. This prevents the atmospheric air from entering the dynamic pressure chamber and causing any braking force. The piston's vacuum valve is separated from the control valve in this position, providing an opening between passage A and passage B (Figure 2.7a). This passage allows vacuum into the dynamic pressure chamber since the constant pressure chamber is always under vacuum. This results in the piston being pushed to the right by the piston return spring.

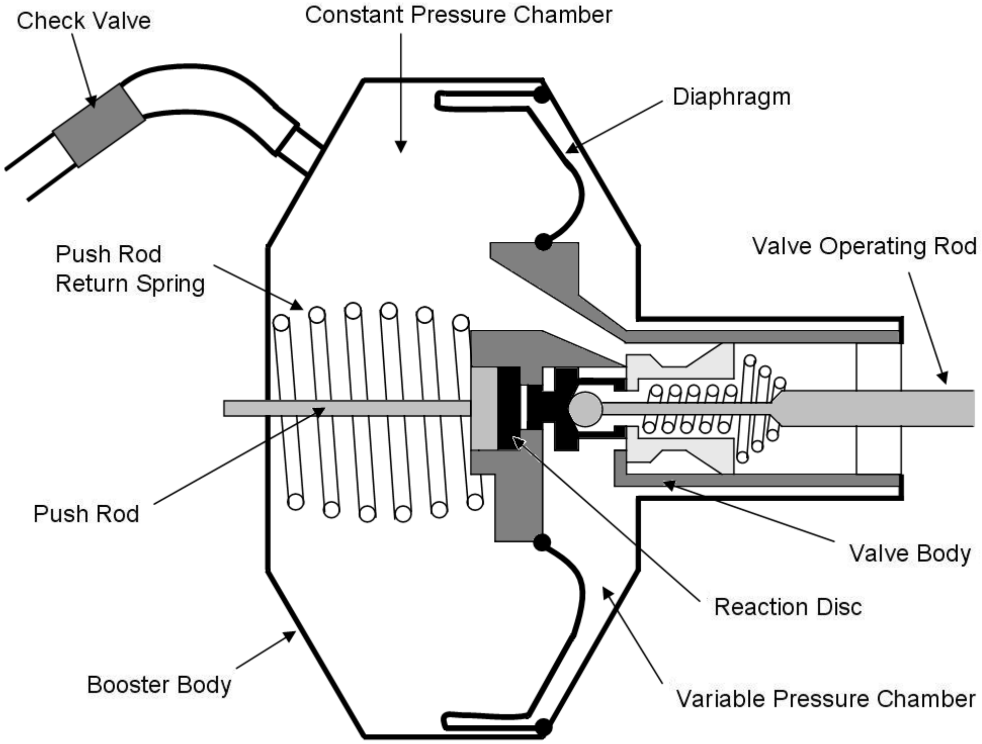

Figure 2.6: Brake booster overview [3]

Brakes Applied

When the brakes are applied, the valve operating rod pushes the air valve to the left. This causes the control valve (which is pushed against the air valve by the control valve spring) to move to the left until it touches the vacuum valve. This blocks off the opening between passage A and passage B (Figure 2.7b). As the air valve moves further to the left, it moves away from the control valve, allowing atmospheric pressure to enter the dynamic pressure chamber through passage B.

Brakes Held

When the brakes are held, the pressure difference between the constant pressure chamber and the dynamic pressure chamber causes the piston to move to the left resulting in the

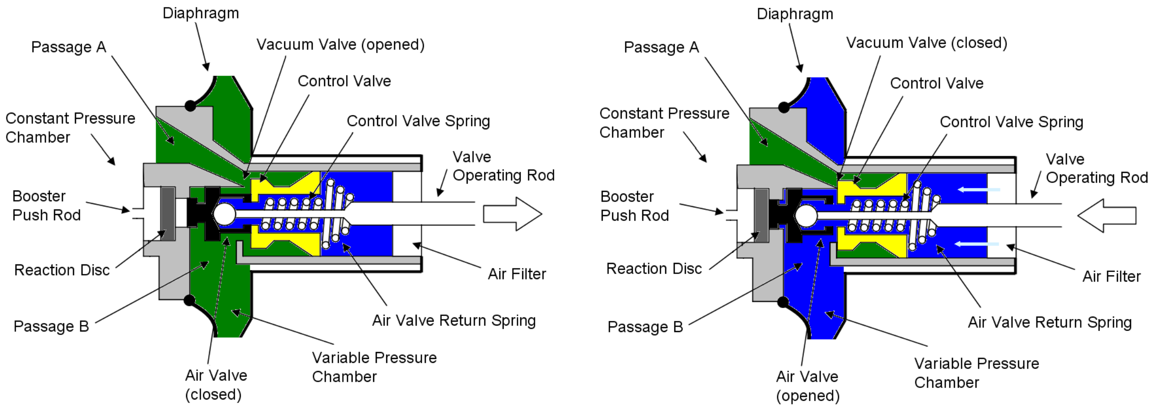

(a) Brakes not applied (b) Brakes applied

Figure 2.7: Brake booster operation: brakes not applied and brakes applied [17]

reaction disc to move the booster push rod to the left exerting a braking force. As the piston moves left it also causes the control valve to move left until it contacts the air valve, blocking atmospheric air from entering the dynamic pressure chamber while vacuum is still blocked by the control valve (Figure 2.8a). The amount of air (pressure) that enters the dynamic pressure chamber depends on the movement of the piston which depends on the force applied to the brake pedal by the driver.

Brakes Released

When the brakes are released, the valve operating rod and the air valve are moved to the right by the air valve return spring. This causes the air valve to contact the control valve, blocking atmospheric pressure from entering the dynamic pressure chamber. At the same time the control valve spring retracts causing the control valve to move away from the vacuum valve connecting passage A with passage B (Figure 2.8b). This allows the pressure from the dynamic pressure chamber to flow into the constant pressure chamber eliminating the pressure difference and returning the booster to the brakes-not-applied stage.

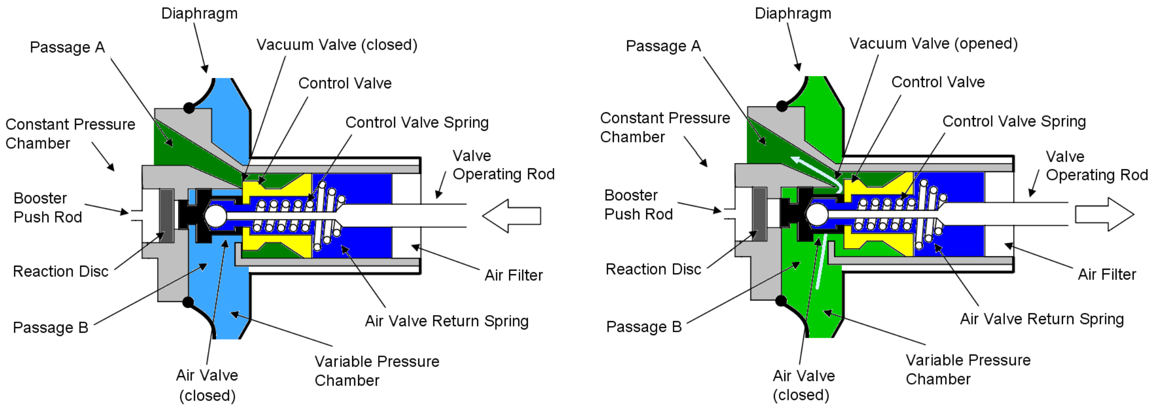

(a) Brakes held

(b) Brakes released

Figure 2.8: Brake booster operation: brakes held and brakes released [17]

2.2.3 Master Cylinder

The function of the master cylinder is to convert the force created by the brake pedal and brake booster into hydraulic pressure by means of a cylinder and piston. The simplest construction of a master cylinder has two chambers: a cylinder pressure chamber and a reservoir chamber [17]. The reservoir chamber compensates for any change of brake fluid volume due to temperature change or brake pad wear. The cylinder pressure chamber which is full of fluid at all times, contains a piston connected to a pushrod which has a reduced diameter in the middle. Both ends of the piston are fitted with seals to prevent any leakage of fluid.

Master Cylinder Operation

The master cylinder has two different modes of operation, occurring when the brakes are applied and when the brakes are released.

Brakes Applied

When applying the brakes, the brake pedal and brake booster forces travel through the pushrod and push the piston along the cylinder. This seals off the compensation port which is connected to the reservoir chamber and compresses the fluid in the cylinder (Figure 2.9).

The compression will cause an increase of the fluid pressure inside the master cylinder which in turn will push open a check valve and force fluid into the brake lines [17].

Brakes Released

When releasing the brake pedal, the return spring inside the cylinder pressure chamber forces the piston back to its original position. This causes a pressure drop in the master cylinder which distorts the primary seal and uncovers the recuperation holes. This allows fluid from around the piston to flow into the pressure chamber and temporarily balance the pressure difference between the two sides. At the same time, fluid is returning from the brake lines which pushes the check valve away from its rubber seat and flows back into the master cylinder [17].

For safety reasons all master cylinders on today's vehicles are dual-circuit systems. This means that they have two separate hydraulic brake circuits which operate from a master cylinder with two independent pressure chambers. Should a failure occur in one of the hydraulic circuits, the other will still remain operational, however with a reduced amount of braking force (Figure 2.9). The two common dual-circuit configurations are the front to rear brake line split and the diagonally front to rear brake line split. The latter has the advantage that no matter which circuit fails, there will always be at least one front brake that remains operative [17]. This is important because the deceleration during braking causes weight to transfer from the rear axle to the front axle allowing the front brakes to apply a larger braking force.

2.2.4 Brake Proportioning Valve

During the deceleration of a vehicle, there is a transfer of weight from the rear axle of the vehicle to the front axle of the vehicle. The amount of brake force that can be applied prior to wheel lock depends on the amount of weight on each wheel. If the brake line pressure from the master cylinder were the same at all four wheels, it would cause the rear axle to lock up first during heavy braking manoeuvres and possibly cause the vehicle to become unstable. To counteract this problem, motor vehicles are equipped with some type of brake

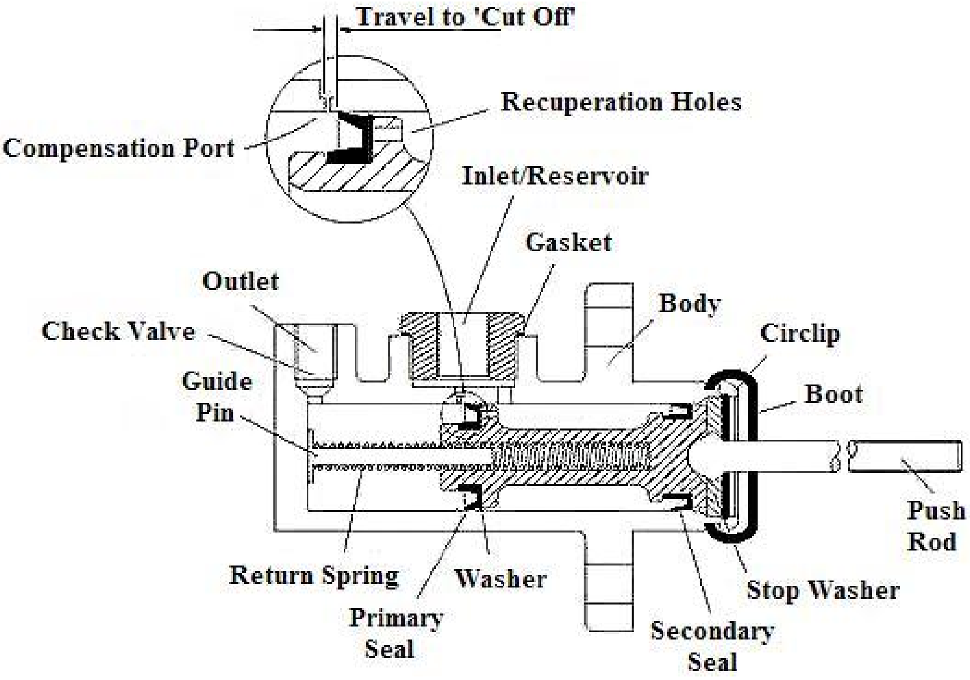

Figure 2.9: Master cylinder overview [42]

line pressure limiter valve or proportioning valve [28].

The limiter valve allows both the front and rear brakes to receive equal pressures up to a certain predefined pressure and then, after that, only the front brake line pressure increases. The downfall of this system is that once the front brakes lock, no further increase in vehicle deceleration is possible because the rear brake line pressure will be constant no matter how high the brake pedal force.

With a proportioning valve, the front and rear brake line pressures are identical up to the knee point pressure. After the knee point, the rear brake line pressure increases at a lower rate compared to the front brake line pressure. In newer vehicles the knee point can be altered either electronically or mechanically depending on the deceleration of the vehicle or the load carried by the rear axle of the vehicle [17].

2.3 Electric Motors and Power Electronics

Hybrid electric vehicles have brought many new specialties to the automotive industry. It has become extremely important to make the electric motors, power electronics and energy storage systems as lightweight and efficient as possible in order to extend the electric range of HEV's. This section will describe the basic components and operation of the electric drive system in a hybrid electric vehicle and how this system can be used for regenerative braking.

2.3.1 Electric Motors

Electric motors used for vehicle propulsion have many necessary characteristics that have to be met for use in hybrid electric vehicles. They have to be as small and lightweight as possible while delivering high stall torque to assist in acceleration, and maintain this torque over a wide range of motor speeds. They should also be very efficient to limit the size of the ESS while maintaining a high level of reliability over the lifetime of the vehicle. With so many important characteristics to be considered, it is not surprising that no electric motor has become the motor of choice for HEV's. However, over the past few years there are four classes of electric motors that have typically been used for hybrid propulsion systems:

- permanent magnet brushed DC motor
- permanent magnet brushless DC or AC synchronous motor
- AC induction motor
- switched reluctance motor

For the AUTO21 E03 RGB project, it was decided previously that an AC induction motor would be used for the hybrid vehicle conversion because of its low cost and reliability. For this reason the common hybrid vehicle electric motors will briefly be explained followed by more control basics of the induction motor only.

Permanent Magnet Brushed DC Motor

The brushed DC motor is the simplest form of electric motor. It is widely used in many applications and is the easiest to control [25]. The classical DC motor is equipped with a stator consisting of permanent magnets and a rotor/axle consisting of brushes, coil/armature and a commutator. When the coil is powered, the current passing through the coil produces a magnetic field around the armature. The permanent magnets of the stator then either attract or repel the armature creating a rotating torque. As the coils become in line with the magnets, the commutator then switches the direction of the current through the coil, reversing the magnetic field. This process continues until the power is cut off. In modern brushed DC motors more than one coil is used meaning the commutator consists of several segments and more than one pair of permanent magnets is used to increase the average turning-moment. Controlling the brushed DC motor can be easily achieved by controlling the supply voltage to the motor, which proportionally controls the rotational speed of the motor. These motors have the advantages of being simple, cheap and easy to control [35].

Permanent Magnet Brushless DC or AC Synchronous Motor

The brushless DC motor actually uses alternating current, however this alternating current must be variable frequency and therefore is derived from a DC supply. For a brushless DC motor, the rotor consists of a permanent magnet and the stator contains the coil. There are no brushes or commutator. Instead, switches are used to reverse the magnetic field in the coils and force the rotor to rotate. Unlike the brushed DC motor, the rotor has the constant magnetic field. The rotor is attracted or repelled by the stator depending on the position of the rotor, causing a rotating torque. The switching of the current must be synchronized with the position of the rotor. This is generally done using sensors connected to an inverter which control the AC frequency. Brushless DC motors have the advantages of being very lightweight and efficient. They are also very reliable because they do not have brushes and can have high motor speeds [35].

Switched Reluctance Motor

The basic operation of a switched reluctance motor is quite simple. The iron stator and rotor are magnetized by a current through the coil on the stator. If the rotor is out of line with the magnetic field of the stator, a torque will be produced to rotate the rotor and minimize the air gap (reluctance) between the two to make the magnetic field symmetrical [25]. When the rotor is aligned with the stator, the current is switched off and its momentum is allowed to carry the rotor to a position where the current can be reapplied. This process is then repeated for continuous motion. To control this motor, the current in the coil does not need to alternate, so essentially the speed can be varied by altering the length of time that the current is on during each power pulse. Like the brushless DC motor, the switching of the current 'on' and 'off' must be synchronized with the position of the rotor using sensors. Switched reluctance motors have the advantages of being low cost and efficient as well as being very reliable and having the ability to run at very high motor speeds. Also, since it does not use permanent magnets, there will be less back electro magnetic field (EMF) created in the coils. In brushed DC and brushless DC motor this back EMF is proportional to the speed of rotation of the rotor and will reduce the current flowing in the coil. This reduced current will then reduce the magnetic field strength and hence reduce the torque created as the speed increases [25].

AC Induction Motor

Induction motors are widely used machines that require an AC power supply. The typical three phase induction motor consists of three coils or pairs of poles (P) wound around the outer part of the motor or stator. The rotor usually consists of copper or aluminum rods (conductors) that are short circuited at the ends creating a cage-like structure. This is the reason induction motors are also known as squirrel cage motors. The three windings are arranged so that a positive current produces a magnetic field (flux) in each coil 120 degrees apart. If these coils are then fed with a three phase alternating current, the resultant magnetic field rotates proportional to the frequency of the current. This induces an electromagnetic field and current in the rotor windings in such a direction that its own magnetic field opposes the change that produced it (Lenz's Law). This induced current in the rotor then produces a force which turns the rotor and 'chases' the rotating magnetic

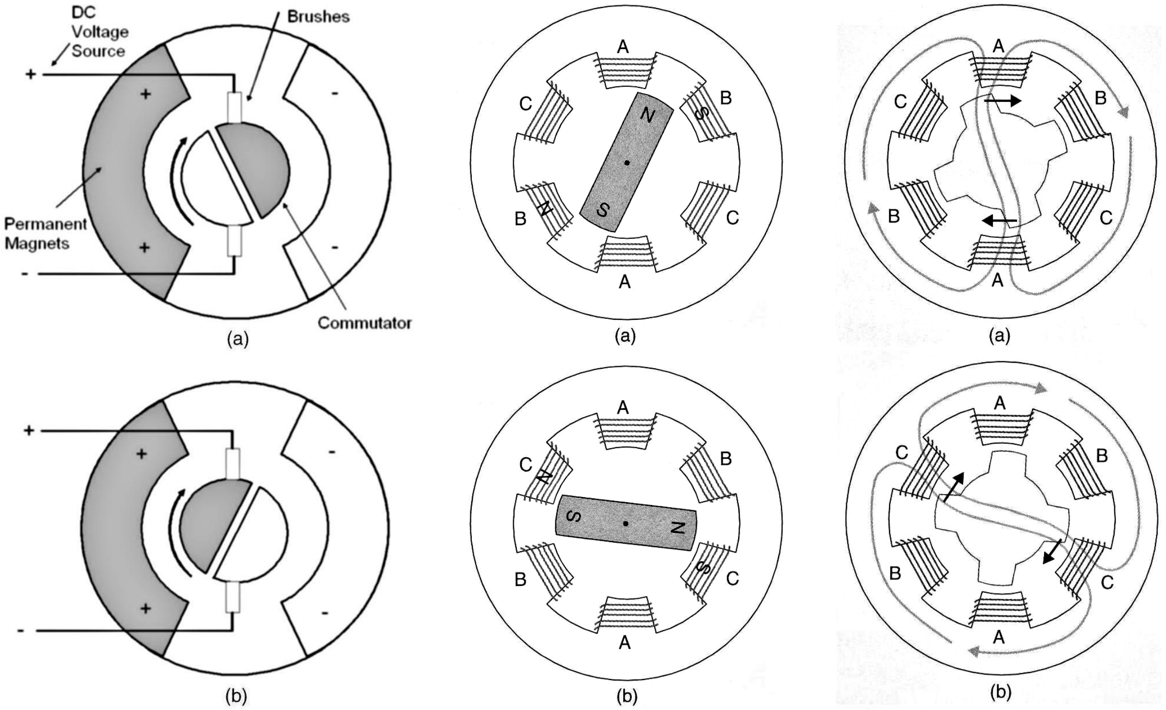

(a) Brushed DC motor (b) Brushless DC motor (c) Switched reluctance motor

Figure 2.10: Electric motors [25]

field in the stator caused by the alternating current (Figure 2.11). The speed at which the magnetic field rotates, in rpm, is the synchronous speed (N_s) given by Equation 2.3. Where f is the frequency in hertz and P is the pairs of poles or coils. Torque is produced only when there is a difference between the rotor speed (N) and the synchronous speed, given by the slip (S), which can be calculated using Equation 2.4. Torque and slip are related differently for every motor, however all induction motors follow the similar trend that as slip increases so does the torque.

$$N_s = \frac{120 \times f}{P} \tag{2.3}$$

$$S = \frac{N_s - N}{N_s}\ \% \tag{2.4}$$

Induction motors have the advantages of being low cost and extremely reliable as well as allowing dynamic torque control with the proper controlling algorithms. Characteristics of the electric motors mentioned above are shown in Table 2.2.

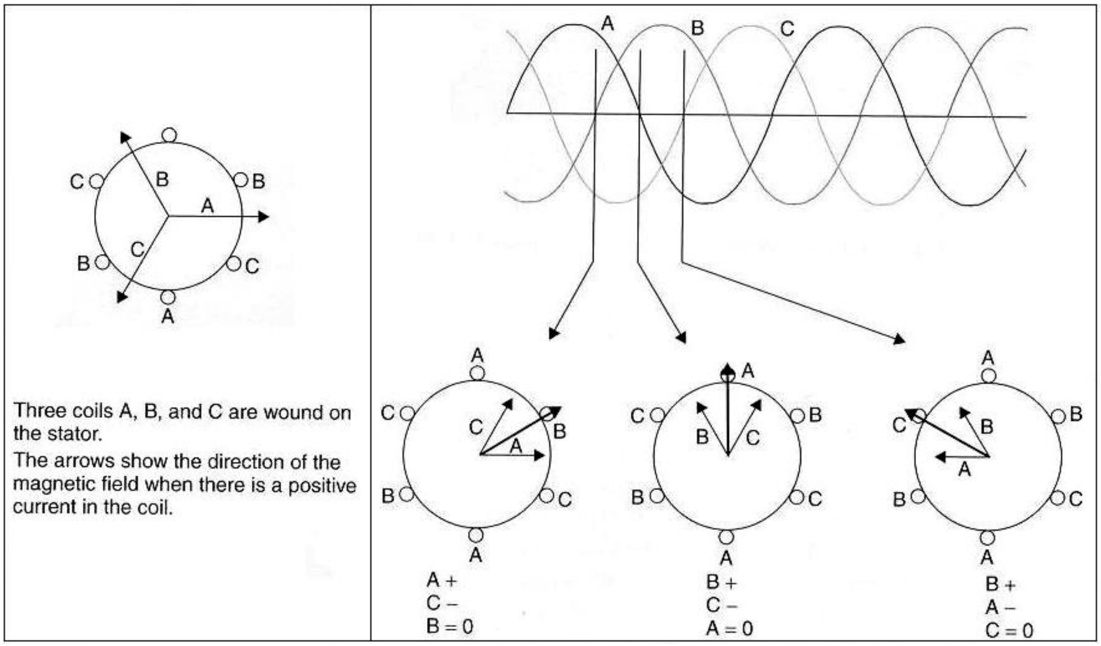

Three coils A, B, and C are wound on the stator.
The arrows show the direction of the magnetic field when there is a positive current in the coil.

Figure 2.11: Rotating magnetic field produced within an induction motor [25]

2.3.2 Power Electronics

Power electronics is the technology associated with the efficient conversion, control and conditioning of electric power from its available input into the desired electrical output [4]. With most electric motors requiring variable frequency AC power and all the electric

Motor	**Efficiency**	**Weight**	**Cost**	**Speed**
Brushed DC	75-85%	High	Medium	up to 6,000 rpm
Brushless DC	93-97%	Low	Medium	up to 10,000 rpm
Switched Reluctance	92-95%	Medium	High	up to 80,000 rpm
AC Induction	87-93%	Medium	Low	up to 8,000 rpm

Table 2.2: Characteristics of common electric motors for hybrid vehicles [55],[35]

energy storage systems using DC power, power electronics have come to the forefront with hybrid electric vehicles. It is necessary to control and convert the DC power efficiently into AC power during driving events and to be able to convert AC power back to DC power during regenerative braking. The basis of power electronics revolves around power switching devices that are used during the power conversions (Table 2.3). Power metal oxide silicon field effect transistors (MOSFET's) and insulated gate bipolar transistors (IGBT's) have become the most popular switching devices for hybrid vehicles; MOSFET's are used for lower current mild hybrids and IGBT's are used for higher current power-assist and full hybrids.

Transistor Type	**Maximum Voltage (V)**	**Maximum Current (A)**	**Maximum Frequency (kHz)**	**Cost**
Two-stage Darlington	1400	800	20	Low
Thyristor	3000	2000	1	Low
MOSFET	1000	100	10000	High
IGBT	1200	400	100	High

Table 2.3: Characteristics of common power switching devices [55]

Three Phase Induction Motor Controller

Three phase inverters are used to convert DC power into variable frequency three phase AC power using pulse width modulation (PMW). The circuit consists of six power switching devices (power transistors) with snubber circuits and feedback diodes arranged in a three phase bridge (Figure 2.12). The current to the motor is controlled by pulse width modulation using a digital signal processor (DSP). A DSP is a specialized microprocessor designed specifically for digital signal processing, generally for real time computing. It can convert analog feedback signals back into digital signals for processing and then convert these digital signals back to analog signals for output to the system [35].

The DSP uses vector control as described below to control the pulse width, frequency and phase of the current by outputting signals to the power switches of the inverter. This will optimize the alternating current output sent to each phase of the motor. The fast feedback diode is connected in parallel with each power transistor and provides a return path for the motor current when the power transistor switches off. The snubber circuit controls the shape of the switching waveform and suppresses electrical transients. There is also a filter capacitor bank connected across the input from the DC source. The capacitor banks function is to filter DC input voltage and to provide a low impedance path for the high frequency currents generated during PWM switching [52].

Pulse Width Modulation

There are many different PWM techniques used for hybrid propulsion drives and the goal of this section is not to cover them in great detail but rather to give a brief overview of PWM in general. The motivation for PWM is to convert DC bus power into variable frequency three phase AC power with the lowest possible losses while making optimum use of the available power supply [35]. This is accomplished using the motor controller described above with the switching sequence shown in Figure 2.13. The switching of the power transistors is precisely controlled by the DSP. The switches operate in three pairs. If one of the switches of the pair is ‘on’ then the other switch must be ‘off’ to prevent short-circuiting the power supply. When one of the switches is turned ‘on’, current is able to flow to or from the motor at the bus voltage. When the switches are ‘off’, the current

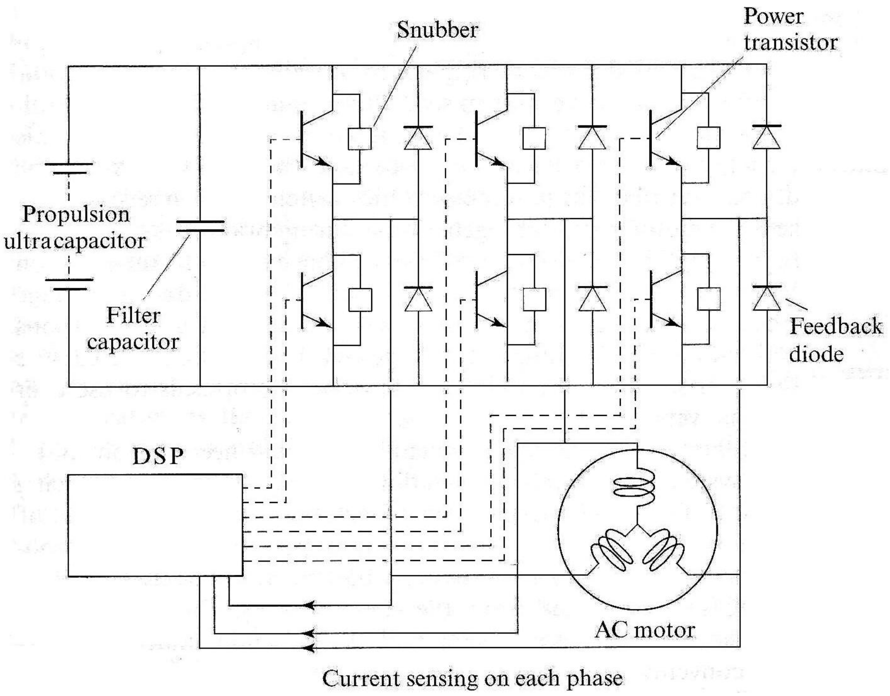

Figure 2.12: Induction motor drive circuit [55]

that continues to flow because of the load inductance is allowed to flow through the free wheeling diodes in parallel with the power switches. To create alternating current, the duty cycle or pulse width of the switches is controlled. This is usually accomplished by comparing the ideal AC current wave with a sawtooth wave form, when the two wave forms intersect; the switch is turned ‘on’ or ‘off’ (Figure 2.14).

If the pulse width is small, the average current flowing will be small and if the pulse width is large the average current will be large [31]. As can be seen in Figure 2.15, the pulse width is modulated in an ascending and descending order to mimic the reference AC wave shown. The frequency of cycle can then be changed to control the speed and torque of the motor. In reality there will be many more pulses per cycle than Figure 2.15 shows to ensure that a smooth sinusoidal current is obtained.

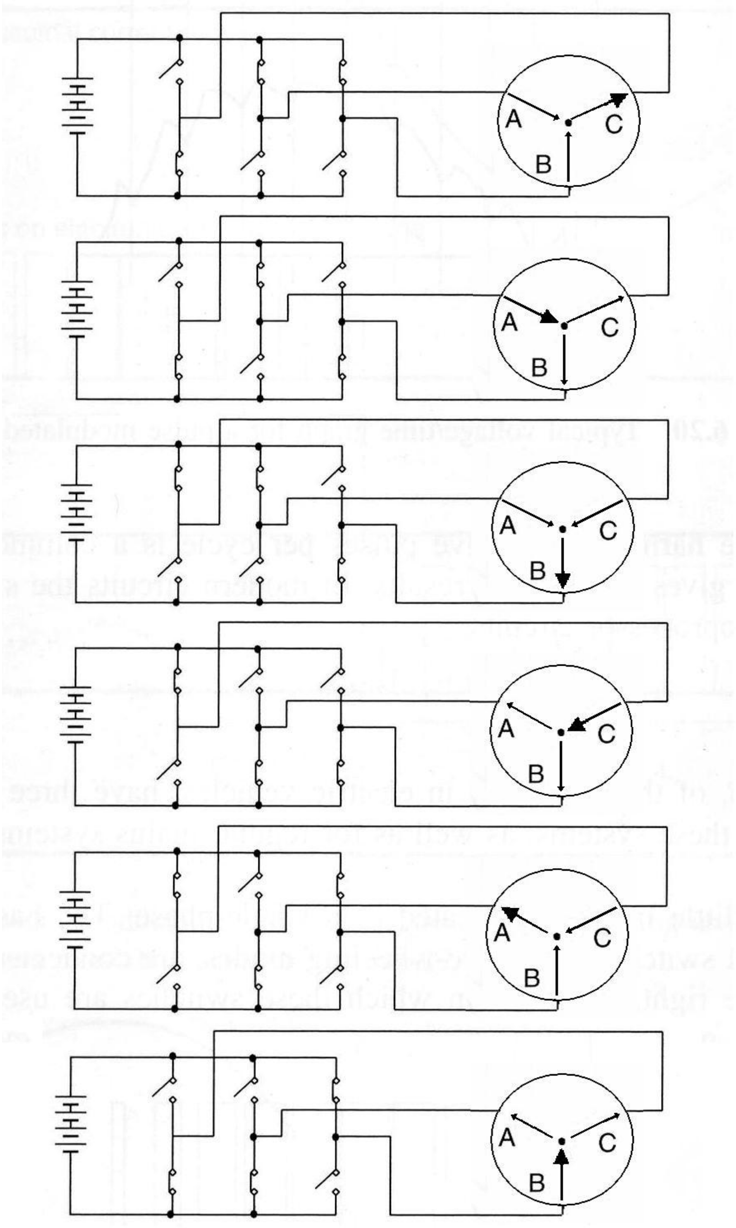

Figure 2.13: Three phase inverter switching sequence [25]

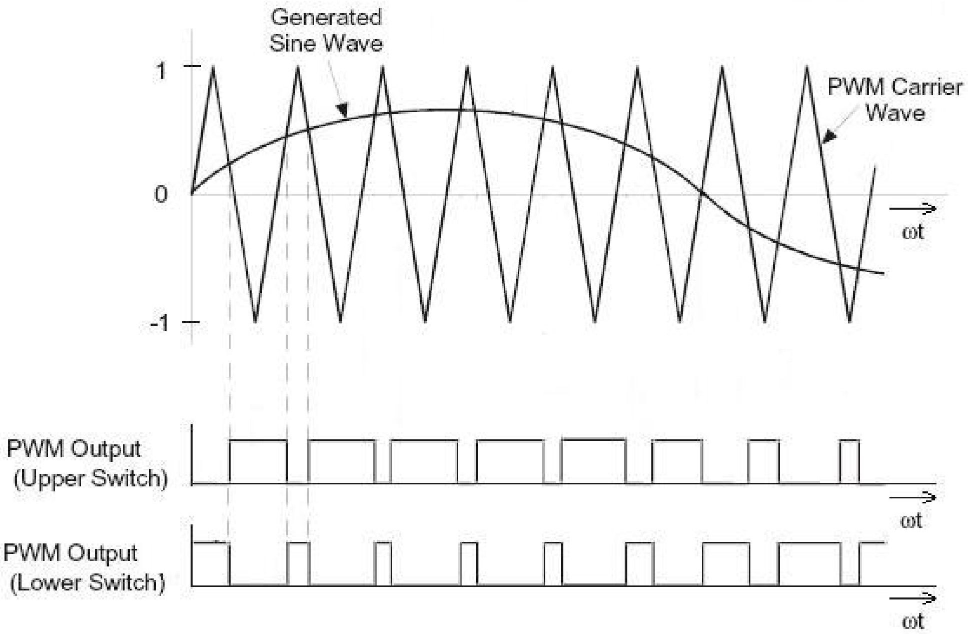

Figure 2.14: Generation of pulse width modulation signal [27]

Vector Control

AC induction motors' poor dynamic behaviour can be overcome by vector control and its computationally intensive algorithms [11]. This, coupled with closed loop control and precise pulse width modulation, requires a relatively powerful microprocessor to make vector control a practical proposition. Scalar control involves controlling only the magnitude of the control variables, with no concern for the coupling effects among these variables. Scalar control, such as the Constant Volts/Hertz method when applied to an AC induction motor, is relatively simple to implement but gives a sluggish response because of the inherent coupling effect due to torque and flux both being functions of current and frequency [11]. Vector control, on the other hand, involves adjusting the magnitude and phase alignment of the vector quantities of the motor. Vector control decouples the vectors of field current and armature flux so that they may be controlled independently to provide fast transient response.

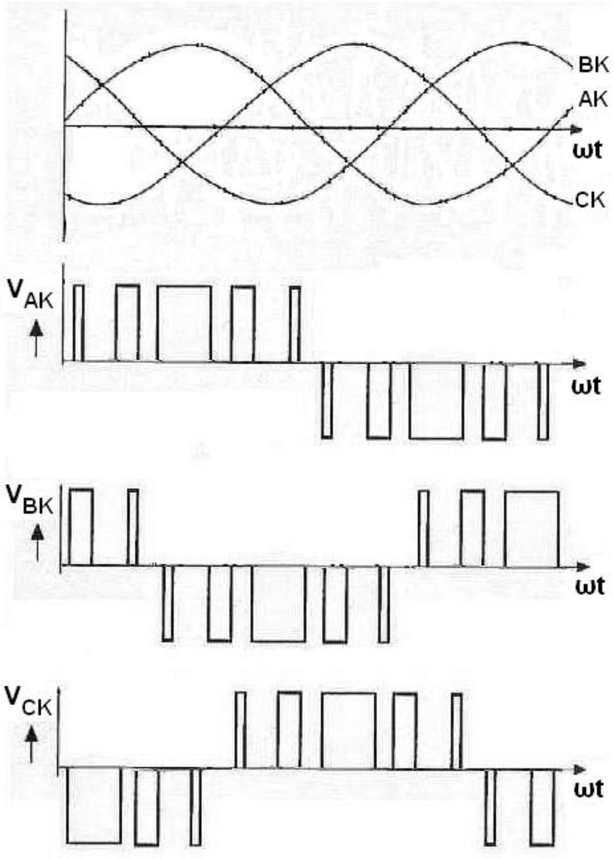

Figure 2.15: Output from three phase inverter [35]

As described above, in a typical induction motor a three phase current is applied to three stationary stator coils. The resulting flux from the stator induces alternating currents in the conductors of the rotor to create its own field. These fields then interact to create torque. Unlike other electric motors, the rotor currents can not be controlled directly in an induction motor, but are derived from the interaction between the stator field and the resultant currents induced in the rotor conductors. In a DC motor the field flux (Φ_f) produced by the field current (I_f) is perpendicular to the armature flux (Φ_a) produced by the armature current (I_a). These fields are decoupled and therefore when the armature current is adjusted to control torque, the field flux remains unaffected, enabling a fast transient response [50]. Vector control recreates these orthogonal components in the induction motor to control the torque-producing current separately from the magnetic flux producing current. This is how an induction motor achieves the responsiveness of a DC machine.

Clarke and Park Transformations

It is possible to represent a three phase induction motor as an equivalent two phase motor using direct/real (d) and quadrature/imaginary (q) axes for both the stator and rotor [27]. Figure 2.16 shows a $d-q$ representation of an induction motor where d_s-q_s represent the direct and quadrature axes of the stationary stator frame and d_s^r-q_s^r represents the rotor flux known as the rotating reference frame.

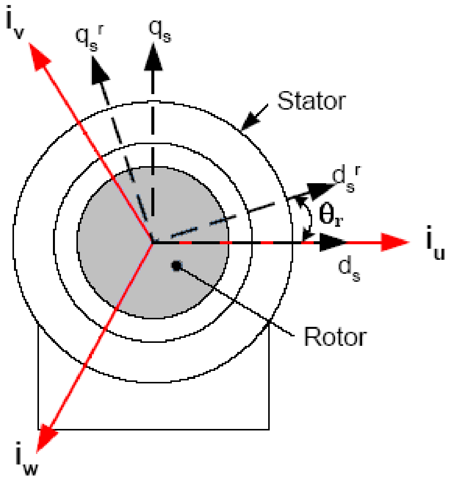

Figure 2.16: Direct and quadrature axes for an AC induction motor [11]

If one of the three phase stator currents (i_u) is placed coincident with d_s, then it can be shown that the vector sum of the three stator currents (i_u, i_v and i_w) can be expressed in terms of d_s and q_s (some texts refer to these axes as α and β) in the stator reference frame [50].

$$
\begin{aligned}
i_{ds} &= k\left(i_u - \frac{1}{2}i_v - \frac{1}{2}i_w\right) \\
i_{qs} &= k\left(\frac{\sqrt{3}}{2}(i_v - i_w)\right)
\end{aligned}
\tag{2.5}
$$

where $k = \frac{2}{3}$ is the transformation constant resulting from reducing the three currents to two currents.

Knowing that in a 3 phase balanced system (with isolated neutral) $i_u + i_v + i_w = 0$ and substituting in for $k = \frac{2}{3}$ then Equation 2.5 can be rewritten.

$$
\begin{aligned}
i_{ds} &= i_u \\
i_{qs} &= \frac{1}{\sqrt{3}}(i_u) + \frac{2}{\sqrt{3}}(i_v)
\end{aligned}
\tag{2.6}
$$

Equation 2.6 represents the transformation of the three phase stator currents into the two phase orthogonal vector representation (d_s and q_s). This mathematical transformation is known as a Clarke transform [27]. From equation 2.6 it can be seen that only two of the phase currents (i_u and i_v) are needed to perform this transformation.

Now that the three phase stator current has been transformed to a two phase current in the stationary stator frame, a Park transform is then used to relate the components from the stationary stator frame to the rotating reference frame of the rotor [27]. The Park transform provides the direct axis and quadrature axis components (i^r_{ds} and i^r_{qs}) of the stator current in a synchronously rotating reference frame that rotates at an angular velocity (ω) and at an angle (θ_r) with respect to the d_s-q_s axes (Equation 2.7). As a result, these coordinates in the rotating reference frame do not vary with time.

$$\begin{aligned} i^r_{ds} &= i_{qs}\sin(\theta_r) + i_{ds}\cos(\theta_r) \\ i^r_{qs} &= i_{qs}\cos(\theta_r) - i_{ds}\sin(\theta_r) \end{aligned} \tag{2.7}$$

Referring back to the DC motor mentioned above, using vector control, i^r_{ds} is analogous to field current (I_f the flux component) and i^r_{qs} is analogous to armature current (I_a the torque component), so that torque (T) is proportional to $i^r_{qs}i^r_{ds}$. As long as i^r_{ds} maintains alignment with the rotor's flux vector and i^r_{qs} is 90 degrees in advance, then flux and current can be controlled independently of each other.

Motoring and Generating

The term motoring is used to describe the operating mode where energy is supplied to the electric motor to propel the vehicle [19]. Generating is used to describe the operating condition in which the kinetic energy of the vehicle is converted to electrical energy [19]. This process is also known as regenerative braking. In an induction motor, these two modes can be described using the rotating stator flux speed (ω_s) and the motor speed (ω_m). During motoring, $\omega_s > \omega_m$ (positive slip) resulting in a positive torque produced by the electric motor. However, during regenerative braking $\omega_s < \omega_m$ (negative slip) causing the induced voltages and currents in the rotor to be of reversed polarity producing an electromagnetic torque that opposes the rotation of the rotor (decelerates the rotor).

The transition from motoring to generating can be illustrated using Figure 2.17. During steady state positive torque operation assume the operating point of the electric motor is at point 1 for a specific speed (ω_m) and condition. To switch to regenerating mode during braking, the motor drive frequency is instantly switched from f_1 to f_2 (point 2) and since the motor can not change speed instantly because of inertia this causes $\omega_s < \omega_m$ which produces a negative braking torque and generates electricity to be stored in the ESS. As the vehicle slows, the motor drive frequency must be continually decreased to sustain regenerative braking using the motor controller (PWM) and power electronics.

Regenerative braking can be sustained as long as the vehicle has kinetic energy, the SOC is below a certain level and the driver requests braking.

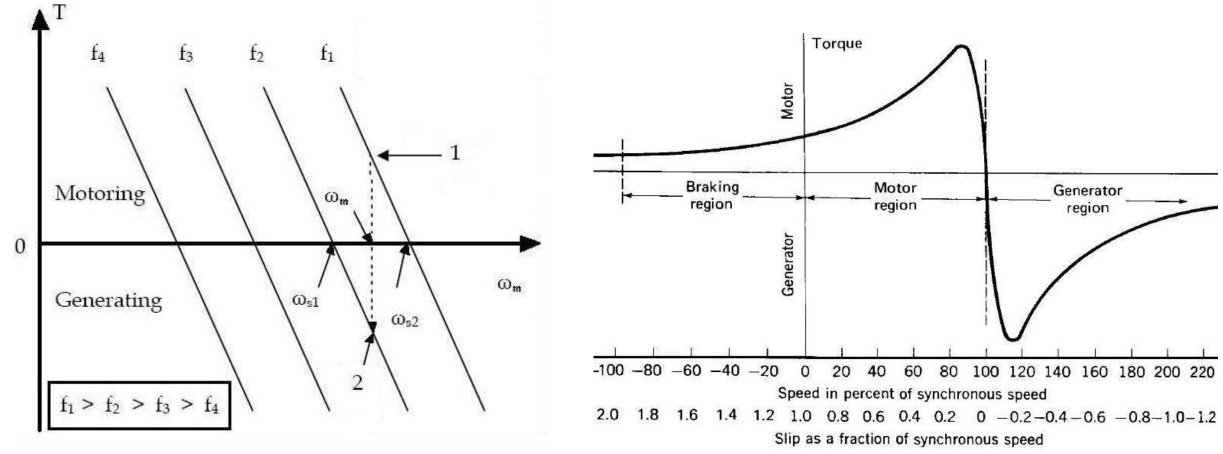

(a) Switching from motoring to generating [39]

(b) Torque curve [27]

Figure 2.17: Regenerative braking operation

2.3.3 Energy Storage Systems

Over the history of the electric and hybrid electric vehicle, the energy storage system has always been the factor limiting the success of this form of propulsion [55]. The main issue with electrical energy storage systems is their energy density. Energy density is defined as the amount of energy stored in a given system per unit mass [25]. The conventional lead acid battery has an energy density of about 35 Wh/kg compared to a useful energy density of more then 2000 Wh/kg for gasoline [35]. For this reason, the electric drive range for electric and hybrid electric vehicles has always been limited by the size and mass of the energy storage system. The two major energy storage systems considered for the AUTO21 E03 RGB project have been batteries and ultracapacitors.

Batteries

Batteries consist of a series of electrochemical (voltaic) cells that store chemical energy and release it in electrical form. Each voltaic cell consists of a positive electrode (cathode) and a negative electrode (anode) connected in series by a conductive electrolyte. The electrolyte dissociates into positive and negative ions and allows these ions to flow to the electrodes. The anode then chemically reacts with the ions (oxidizes) to produce free electrons and a voltage potential. When the cathode and anode are electrically connected, the free electrons can then flow to the cathode, where it chemically reacts with the ions (reduces) producing a current [18]. The three battery types that are currently being developed for hybrid electric vehicles are nickel metal hydride (NiMH), lithium ion (Li-ion) and lithium polymer (Li-Pol). Equation 2.8 shows typical battery chemistry for nickel metal hydride and lithium ion batteries (Note: LiNiO2, LiMnO2 or LiFePO4 can also be used as cathodes for lithium ion batteries).

$$\begin{gathered} NiOOH + MH \Rightarrow Ni(OH)_2 + M \\ Li_xMn_2O_4 + 6C \Rightarrow Li_xC_6 + Mn_2O_4 \end{gathered} \tag{2.8}$$

Though batteries can store substantial amounts of energy they are not capable of releasing this energy quickly, and therefore have low power densities. Batteries store energy chemically and are limited by the time it takes for a chemical reaction to produce electricity. This reaction time, along with the internal resistance of the cell, lowers the power density of batteries.

Ultracapacitors

Ultracapacitors are devices in which two conducting plates are separated by a porous insulator and an electrolyte solution [10]. The conducting plates are coated with a material of extremely high surface area. This produces a high capacitance energy storage system using the electrolytic ions when a low voltage is applied between the plates (Figure 2.18). The insulator allows the electrolytic ions to flow but does not allow a voltage drop or short circuit.

The charge Q (Coulombs) and energy E (Joules) stored in a capacitor of a given

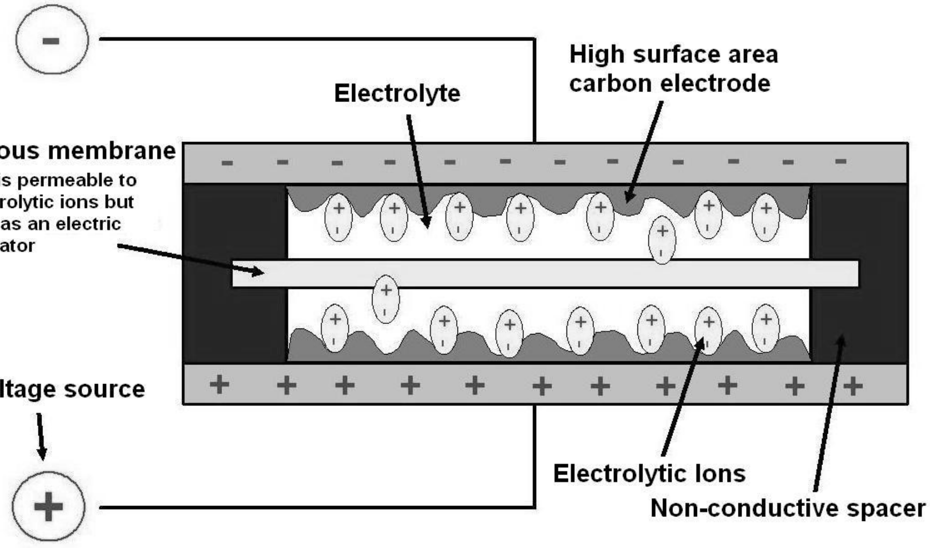

Figure 2.18: Cross section of an ultracapacitor

capacitance C (Farads) and a voltage V (Volts) is given by Equation 2.9:

$$Q = C \cdot V$$
$$E = \frac{1}{2} C V^2 \tag{2.9}$$

The high capacitance of ultracapacitors results from the large surface area and small separation distance illustrated in Equation 2.10.

$$C = \epsilon \frac{A}{d} \tag{2.10}$$

Capacitance is proportional to the plate surface area (A) of the conducting plates (which is very high because of the high surface area of the carbon) and inversely proportional to the distance between the plates, which in modern ultracapacitors is extremely small. The permittivity of the material between the plates is denoted by ϵ. It describes how an electric field affects and is affected by a dielectric medium, and is determined by the ability of a material to polarize in response to the field, and thereby reduce the total electric field inside the material [55].

Since ultracapacitors use very low voltages, it can be seen from Equation 2.9 that energy storage will be limited. The voltage of the ultracapacitors can be increased if many are put in series but this will not increase the stored energy as might be expected because when capacitors are put in series their capacitance decreases according to Equation 2.11.

$$\frac{1}{C} = \frac{1}{C_1} + \frac{1}{C_2} \tag{2.11}$$

Although ultracapacitors have lower energy densities than batteries, they do have much higher power densities because there is no chemical reaction that needs to take place. A comparison between batteries and ultracapcitors is shown in (Table 2.4). This high power density is ideal for regenerative braking in which a large amount of power needs to be stored to increase the regenerative braking capacity of hybrid electric vehicles.

Battery Type	**Maximum Energy Density (Wh/kg)**	**Maximum Power Density (W/kg)**	**Discharge Cycles Before Replacement**
NiMH	70	200	2000+
Li-ion	120-150	120-150	1000+
Li-Pol	200	350	1000
Ultracaps	4	3000	100000+

Table 2.4: Characteristics of typical HEV energy storage systems [35]

Chapter 3

Design Solution

3.1 Design Methodology

Before the design for a project can begin, the need for that product must be established to identify market research-specific deliverables to meet customer demands [54]. The results of this project definition phase are then used to focus the generation and evaluation of conceptual designs. During the conceptual design phase, designs will be generated and evaluated iteratively based on the project definition with the goal of choosing the best design. Once a concept has been chosen, it is embodied during the preliminary design phase and continuously refined with the aid of virtual and physical prototypes until a demonstratively working system is developed.

3.1.1 Project Definition

Although HEV's have improved emissions and fuel economy over traditional automobiles, the added cost of the hybrid system deters some customers from purchasing these vehicles [18]. One of the more expensive systems added to HEV's is the electro-hydraulic braking system [45] mentioned in Chapter 2.

As part of a larger research programme to investigate the application of ultracapacitors for regenerative braking [33], a low-cost approach to the integration of mechanical and regenerative braking was pursued. The new hybrid brake system must integrate regenerative and mechanical braking in a manner that is transparent to the driver (keep torque fluctuations below 5 Nm), and maximizes regenerative braking potential. Ideally, mechanical braking should vary from 0% to 100% of demand, independent of the pedal force. It must also have an adequate response time to address driver demand and moment to moment variations in regenerative braking. A maximum response time of 0.6 seconds is suggested from regulations [16].

Figure 3.1 schematically represents a typical braking event considered for the project. The driver demand curve is created by the force exerted on the brake pedal and is directly proportional to requested torque. As time elapses, the angular speed of the electric motor will slow, which will reduce available regenerative braking. The total required brake force must be supplemented by the mechanical braking system. At some point, regenerative braking will no longer be efficient and full mechanical braking will be required. It was decided that a reasonable time response (Δt) to go from maximum to full mechanical braking would be less than 0.4 seconds.

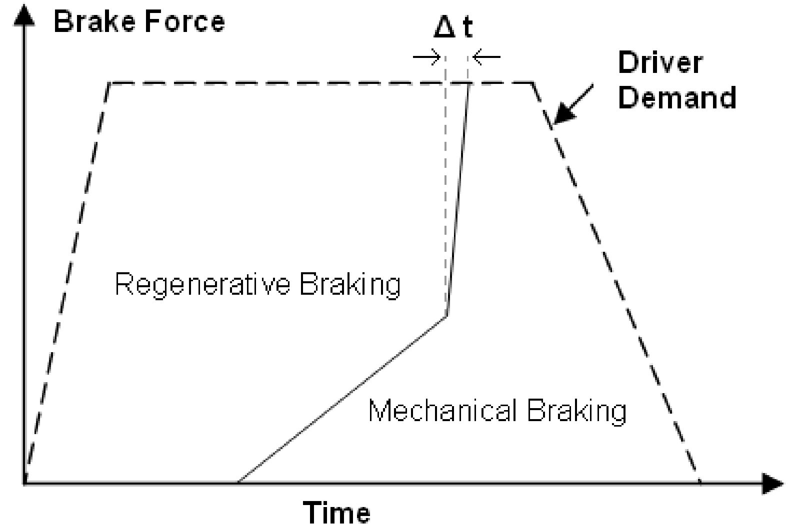

Figure 3.1: Required distribution of the regenerative and mechanical braking force

3.1.2 Conceptual Design

During the conceptual design phase, existing and conceptual designs were considered in order to choose a design that best fits the project definition.

The current EHB system in most HEV's (e.g. Toyota Prius) uses a brake pedal simulator, which is separate from the hydraulic braking circuit, to establish driver braking demand. The braking demand is then sent to a system that contains a high pressure hydraulic pump, accumulator and proportional control valves. The proportional control valves allow the brake line fluid to flow to each wheel at predefined pressures determined by the braking demand.

The simplest alternate concept considered involved downsizing a standard automotive braking system and supplementing the extra braking torque with regenerative braking. This system required no major modifications to the existing brake system and the regenerative braking could easily be controlled using simple algorithms. However, this does not achieve the desired braking flexibility of controlling the regenerative and mechanical braking independent of the brake pedal force.

The second concept was an electro-mechanical brake system that used small electric motors in the brake caliper to push the brake pads against the brake rotor to create braking torque. This eliminates the hydraulic system from the standard braking system. However, a hydraulic back-up system would still need to be installed in case of primary system failure. This system requires a brake pedal simulator as a method of establishing braking demand.

The last concept was a new electro-mechanical brake booster design (Figure 3.2), not currently used in the automotive industry. The idea for this concept was first suggested by Chris Mendes, a former master's student at the University of Waterloo. A similar concept was found following a patent search [34]. The concept was refined and implemented by the author. It operates by using two electro-mechanical valves to attenuate the boost, and hence braking force, created by the brake booster.

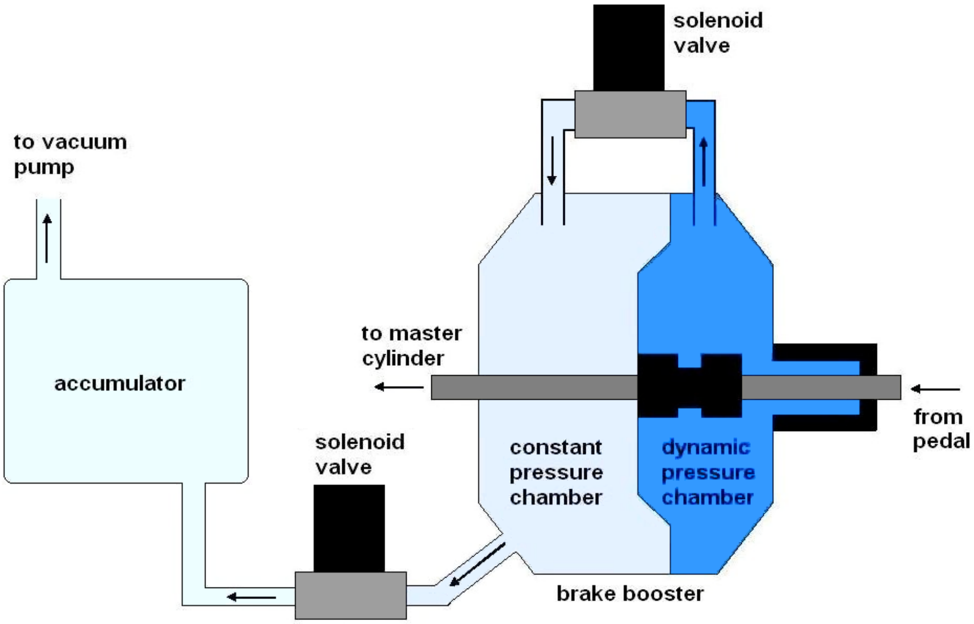

Figure 3.2: Electro-mechanical brake booster concept

After careful consideration, the electro-mechanical brake booster was chosen. The concept uses an inexpensive, low pressure pneumatic system that can be easily sourced, it requires no extra back-up systems in case of failure, and has the best potential to meet all the requirements of the previously mentioned project definition.

In standard automotive brake boosters, the vacuum created in the intake manifold is used to create a vacuum in both chambers of the brake booster. When the driver applies the brake, air enters the dynamic pressure chamber of the brake booster according to the force exerted on the brake pedal. This results in a pressure difference between the two chambers which creates an added boost to the driver's pedal force.

The proposed system electro-mechanically controls the pressure differential created within the brake booster using two valves. The first valve allows atmospheric air to enter the brake booster, which will reduce the vacuum created and the effective mechanical braking torque. The second valve allows air to leave the brake booster using a vacuum accumulator, which will increase the boost created. Solenoid valves were chosen as the first option because of their low cost and high reliability. Even though they cannot infinitely vary the flow like a proportional control valve, the discrete 'on' and 'off' stages of the solenoid valves should be small enough that they are not noticeable to the driver.

Cost Benefits of Brake Booster Attenuation Concept

Most HEV's on the road today use electro-hydraulic brake systems. These are series regenerative braking systems which are desirable for regenerative braking efficiency, however they contain many components and can be rather costly. Figure 3.3 represents a typical electro-hydraulic brake system used on current HEV's [22].

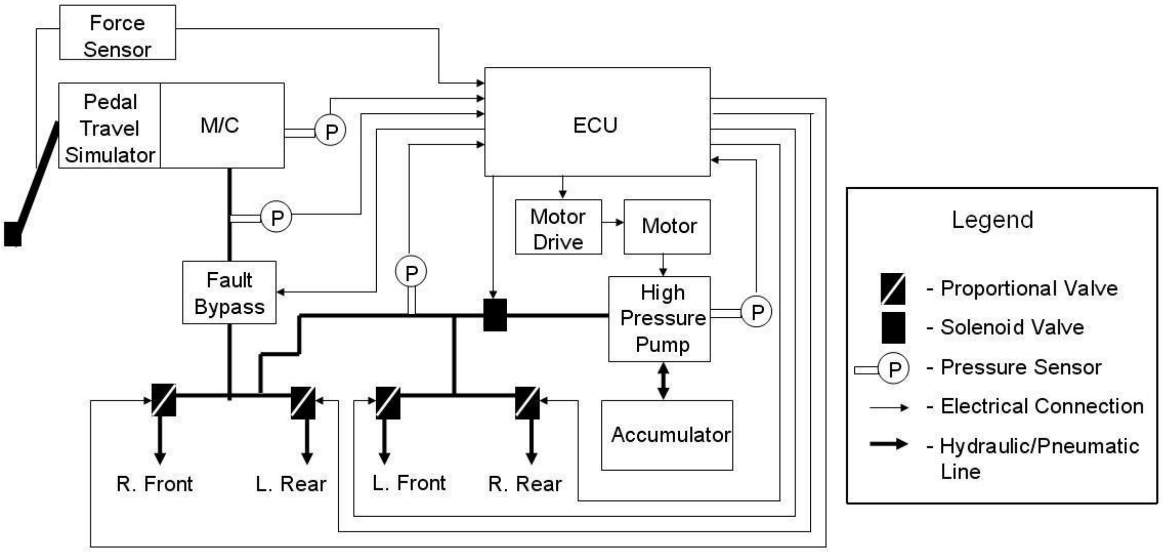

Figure 3.3: EHB schematic [22]

It is easy to see the complexity of this design. In contrast, Figure 3.4 shows the brake booster attenuation concept which uses no proportional solenoid valves, no brake pedal simulator, no fault bypass and has no need for a costly high pressure pump or high pressure accumulator.

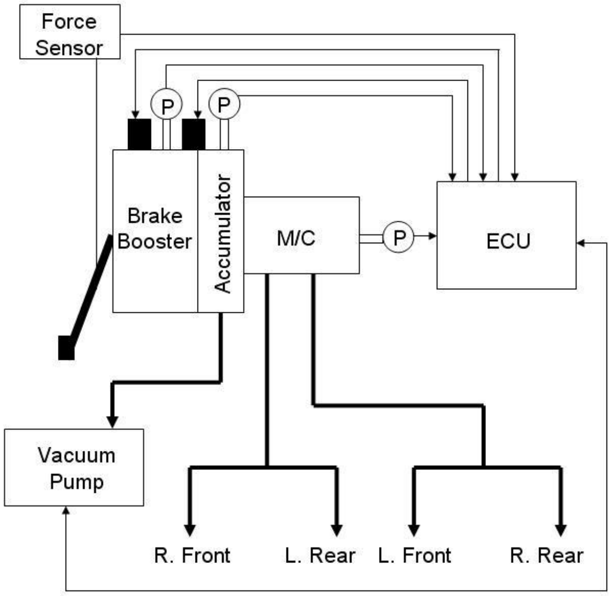

Figure 3.4: Brake booster attenuation schematic

Efficiency of Brake Booster Attenuation Concept

As mentioned above, series regenerative braking systems have the ability to brake the vehicle using only the electric motor. By using the brake booster attenuation concept, the entire boost created by the brake booster can be removed if necessary, leaving only the small pedal force to create pressure in the brake lines. During light to moderate braking events (less then 50 N of pedal force) the springs in the brake booster will oppose the pedal force resulting in no brake line pressure. During heavier braking events, the attenuation system has the ability to reduce the brake line pressures by up to 6 times. This will allow the attenuation system to reduce the mechanical braking to negligible amounts, resulting in increased regenerative braking performance.

3.1.3 Proof of Conceptual Design

Since standard automotive brake boosters use a variable pressure differential to boost pedal force, it was assumed that the same principle could be used for the electro-mechanical brake concept. However, it had to be verified that the electro-mechanical valves could provide an adequate response time. To evaluate the time response, a simple virtual prototype was created that modelled an estimated brake booster volume of 2.5 litres, an infinite accumulator held at 30 kPa, and a valve with a flow factor of 1.6. It was decided that reducing the pressure in the brake booster from atmospheric pressure (101.3 kPa) to 75 kPa would correspond to full mechanical braking. This virtual test was then carried out physically using a brake booster volume of 2.5 litres, a 4 litre accumulator initially at 30 kPa, and a valve with a flow factor of 1.63. A schematic of the proof of concept is shown in Figure 3.5.

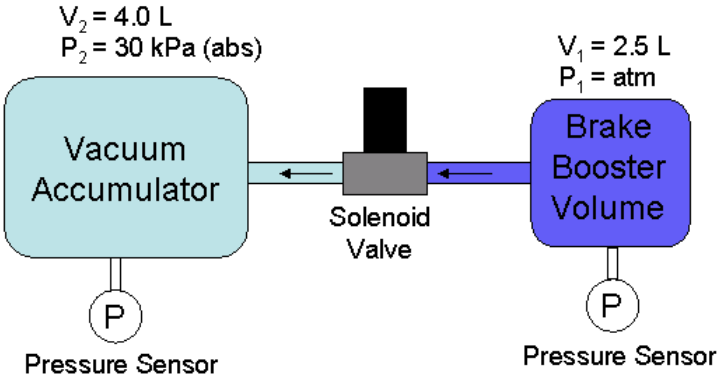

Figure 3.5: Proof of concept schematic

The results from these tests can be seen in Figure 3.6. A 10 second test was run in which the valves were activated after 8 seconds and were closed after the pressure dropped below 75 kPa. The figure is enlarged around the region of the graph that shows the response time of the system. It is shown that both the simple virtual and physical prototypes have response times less than 0.4 seconds to demonstrate the feasibility of the concept.

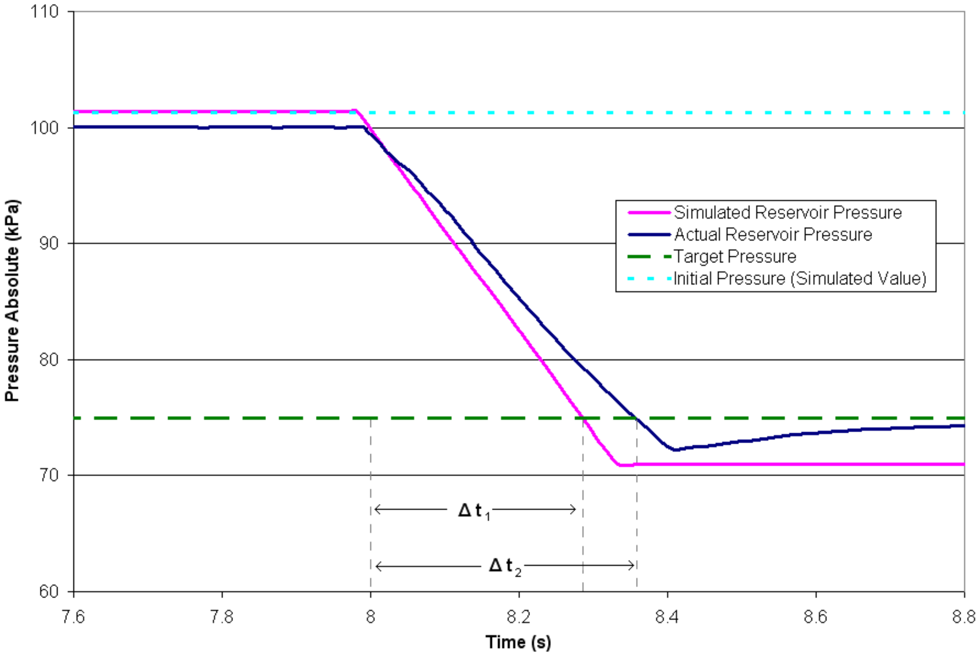

Figure 3.6: Virtual and physical prototype response time test

Chapter 4

Preliminary Design

4.1 Introduction

The focus of the preliminary design phase is to establish the configuration and to demonstrate the ability of the system to function as described in the project definition. It was decided that both virtual and physical mechanical/regenerative braking prototypes would be created to demonstrate the functionality of the system. These prototypes were also used in combination as a powerful tool to validate and develop the system in an efficient and confident manner.

4.1.1 Prototype Configuration

In order to simulate the regenerative braking system in a hybrid electric vehicle, a testbench was created. The prototype system used a flywheel to simulate the inertia of the vehicle, which was connected to a three phase AC induction motor with suitable power electronics, vector control and an ESS to allow for regenerative braking and accelerating of the flywheel. A standard automotive braking system was added to the testbench, which included the brake pedal, brake booster and master cylinder. The brake booster was then modified to implement the electro-mechanical brake booster and electro-mechanical valves were added. The testbench configuration is shown in Figure 4.1.

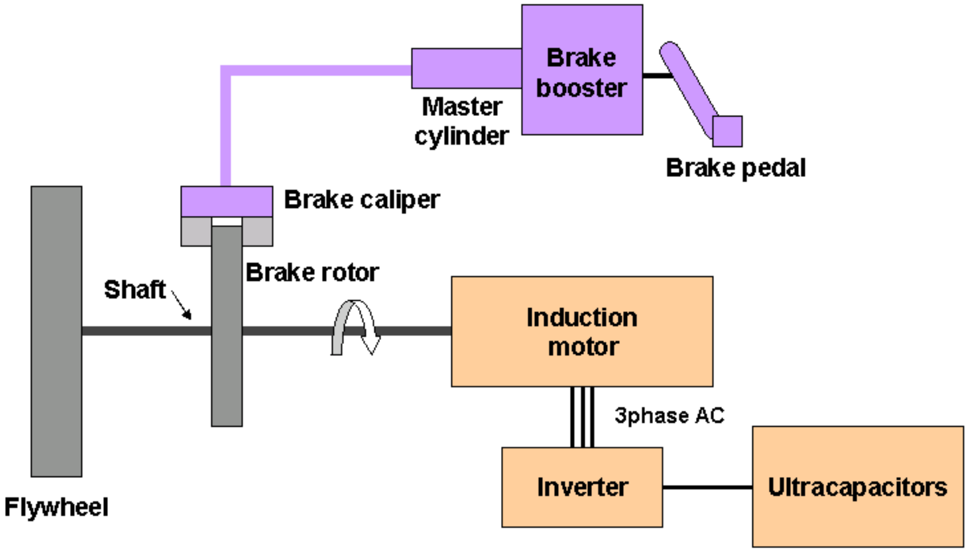

Figure 4.1: Prototype configuration

4.2 Virtual Prototype

The simulation of the mechanical/regenerative braking testbench was created through collaboration among Simon Stark, Samy Ghania and the author. The simulation of the virtual prototype was created in Matlab 7.3.0 (R2006b). The models created in Matlab are displayed in Appendix A, along with the physical constants of the system. Simon Stark focused mainly on the simulation of the energy storage system and the regenerative braking controls while Samy Ghania created the power electronics and vector control. The author was responsible for the simulation of the mechanical system and the control of the brake booster attenuation system. The main scope for this simulation was to demonstrate the functionality of the concept in a cost and time efficient manner along with providing a method of optimizing the system. An overview of the simulation system is shown in Figure 4.2. There are two inputs to the system and four major systems. The first input is the accelerator pedal. This input sends a signal to the controller (Acc) which determines the amount of electric motoring torque (T_{elec_req}) that is required from the electric motor system. The electric motor system then produces the torque (T_{elec}) that drives the flywheel. Once the flywheel has been accelerated to an arbitrary speed, the brake input (F_p) can then be applied. This signal, along with the angular speed of the flywheel (ω) and the state of charge (SOC), are used in the controller to distribute the braking force between the electric motor system, which has already been discussed and the mechanical system (T_{mech_req}). The braking force from the mechanical system (T_{mech}) is then combined with the braking torque from the electric motor system (T_{elec}) to produce the total torque applied to the flywheel (T_{total}).

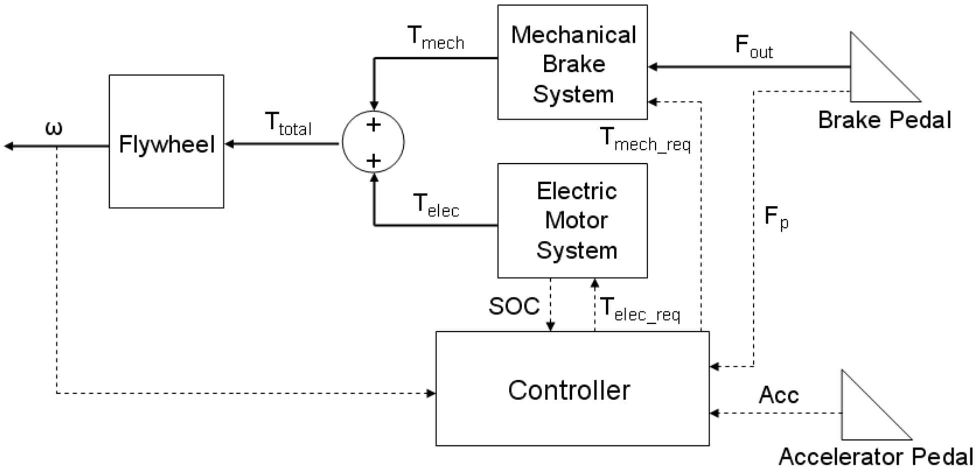

Figure 4.2: Testbench schematic

4.2.1 Mechanical Brake System

The mechanical braking system shown in Figure 4.3 has two inputs: one being the physical brake force created by the pedal (F_{out}) and the other being a requested torque control signal (T_{mech_req}) from the mechanical braking controller. The mechanical braking controller uses valve 1 and valve 2 to vary the boost created by the brake booster (F_{boost}). The boost and pedal force are combined in the brake booster and serve as the input to the master cylinder. The master cylinder then converts this input force into a pressure (P_{mc}) that creates the output braking torque (T_{mech}) in the brake caliper. The mechanical braking controller uses the master cylinder pressure as a feedback when controlling the boost created by the brake booster.

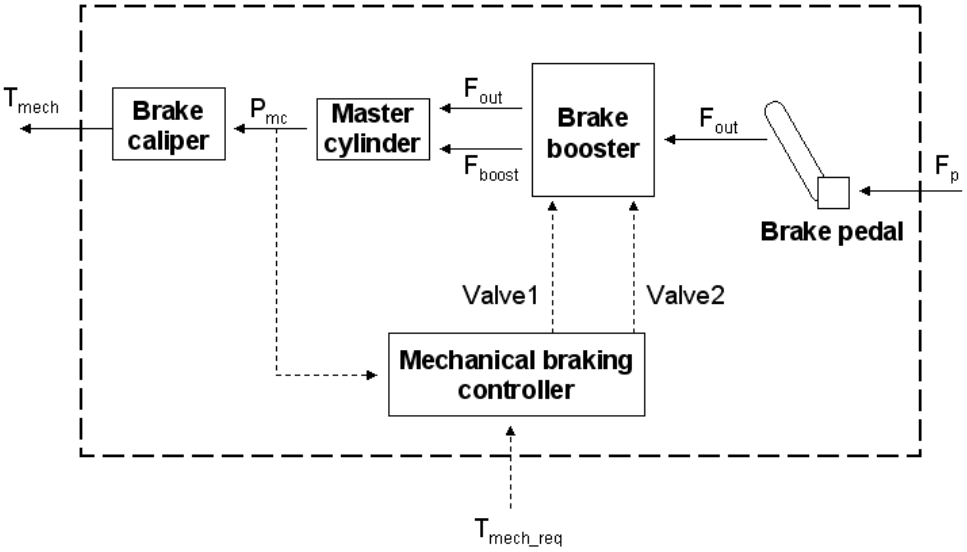

Figure 4.3: Mechanical system schenmatic

The goal for the simulation of the mechanical brake system is to develop reduced order models of the concept that can be used to evaluate the feasibility of the design. These models can then be used to size the components for the physical prototype. Despite the complexity of the braking process, approximate models have been used successfully for years to study brake system lags and their effects [30].

Brake Pedal

The braking simulation of the system begins with a braking force input applied to the brake pedal (F_p). Assuming small angles (θ) the output force from the pedal (F_{out}) can be calculated using Figure 4.4 and Equation 4.1.

To allow for the compliance of the brake pedal and shaft, a first order lag or time constant (τ_p) [57] is used to give the brake pedal a more realistic response (Equation 4.1). Although time delays and first order lag characteristics are not designed into brake systems, pedal travel and spring preloads have been. These characteristics are design factors that contribute to the 'feel' of a brake system [1].

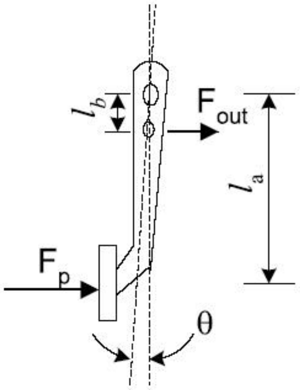

Figure 4.4: FBD of brake pedal [57]

$$F_{out} = \frac{l_a}{l_b}\, F_p$$

$$F_{out}(t) = \frac{l_a}{l_b}\, F_p \left(1 - e^{\frac{-t}{\tau_p}}\right) \tag{4.1}$$

Brake Booster

In a conventional brake booster the force output from the brake pedal (F_{out}) enters the brake booster where a pressure differential between the constant and dynamic pressure chambers creates a boost force (F_{boost}). This force is then added to the force of the pedal, and output to the master cylinder. A schematic of this process is shown in Figure 4.5

In order to reduce some of the complexities of the brake booster created by spring preloads and air flow dynamics, the brake booster was modelled using air chamber thermodynamics [6]. The boost force is created by the pressure differential between the dynamic and constant pressure chambers (P_a and P_v). This pressure differential creates a force using the diaphragm which is added to the pedal force. Knowing the area of the diaphragm (A_d), the boost can be calculated using Equation 4.2.

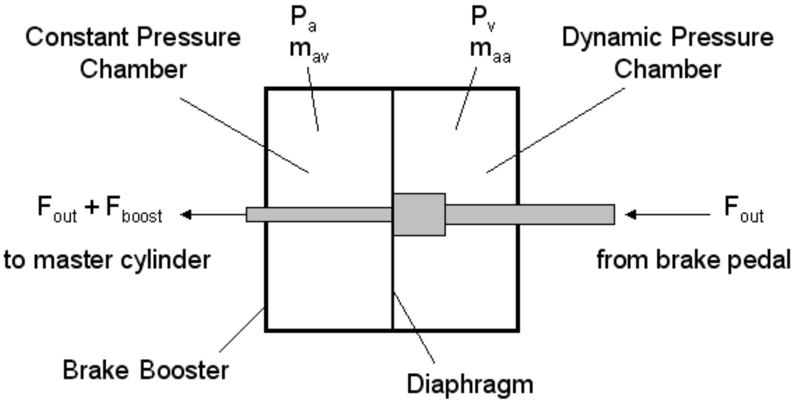

Figure 4.5: Brake booster schematic

$$F_{boost} = (P_v - P_a)A_d \tag{4.2}$$

The air in the brake booster is considered to be an ideal gas undergoing isothermal expansion or compression, which results in the pressure in each chamber being related to the mass of air in the chamber and the diaphragm motion using Equation 4.3 [15].

$$\begin{aligned} P_v &= \frac{m_{av}RT}{(V_{vo} - A_d x_{mc})} \\ P_a &= \frac{m_{aa}RT}{(V_{ao} + A_d x_{mc})} \end{aligned} \tag{4.3}$$

Here V_{vo} and V_{ao} represent the volumes of the constant and dynamic chambers in the fully released position. The displacement of the power piston into the master cylinder is represented by x_{mc} while m_{av} and m_{aa} denote the mass of air in the constant and dynamic chambers.

Since a pressure difference causes the flow into the dynamic chamber, the mass air flow can be determined from the stage of operation using Equation 4.4) [29].

$$\dot{m}_{aa} = \begin{cases} C_{aa}(P_{atm} - P_a) & \text{apply} \\ C_{av}(P_v - P_a) & \text{release} \\ 0 & \text{hold} \end{cases} \tag{4.4}$$

Where C_{aa} and C_{av} are linearized flow resistances between the dynamic chamber and atmospheric air along with the flow resistance between the dynamic chamber and constant pressure chamber. The symbol, P_{atm}, is used for atmospheric pressure.

Brake Booster Attenuation

In standard automotive braking systems, the boost created by the brake booster is dependent on the pedal force. In order to control the boost independently of the brake pedal force, an electro-mechanical brake booster was created that used two valves to attenuate the pressure differential (and hence boost) created by the brake booster. Figure 4.6 shows a schematic of the brake booster attenuation system. During a braking event, the system can open valve 1 which forces atmospheric air into the constant pressure chamber reducing the pressure differential which inturn reduces the boost. If valve 2 is opened, the vacuum accumulator will draw air out of the constant pressure chamber increasing the pressure differential and the boost created. It was decided that two different types of valves would be considered: solenoid valves and proportional valves.

Using Solenoid Valves (Alternate I)

Solenoid valves were the first choice for this system. They are inexpensive, reliable and abundant, however they operate discretely (‘on’ or ‘off’) so they do not offer a lot of control. The solenoid valves used to attenuate the pressure in the constant pressure chamber of the brake booster were modelled using flow factors from current market solenoid valves and first order lag characteristics were used to simulate the reaction time of the valves opening and closing. The time constants used for the lag characteristics were taken directly from

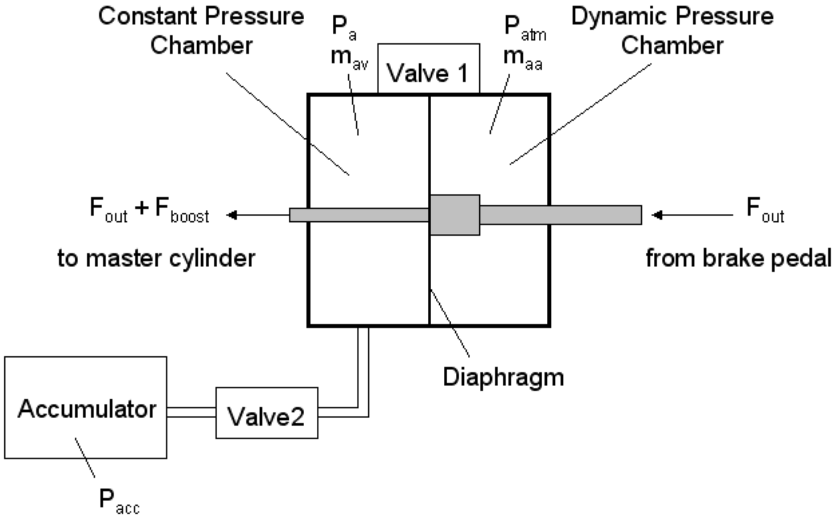

Figure 4.6: Brake booster attenuation schematic

the reaction times of current valves. The solenoid valves were mathematically modelled using Equation 4.5.

$$\dot{m}_{av} = \begin{cases} C_{vacc}(P_v - P_{acc}) & \text{increase mechanical braking torque} \\ C_{va}(P_{atm} - P_v) & \text{decrease mechanical braking torque} \\ 0 & \text{hold mechanical braking torque} \end{cases} \tag{4.5}$$

Where C_{vacc} and C_{av} represent the linearized flow resistances between the constant pressure chamber and the accumulator along with the flow resistance between the constant pressure chamber and atmospheric air. The volume of the accumulator is assumed large compared to the brake booster, resulting in a constant pressure (P_{acc}).

Using Proportional Control Valves (Alternate II)

In order to improve the dynamic response of the brake booster attenuation system, the on/off solenoid valves used in the initial simulation were replaced with proportional control valves. These valves can infinitely vary the air flow through the valve between two points by moving the solenoid within the valve between the fully open and fully closed positions. Mathematically, this means that the flow resistances C_{vacc} and C_{av} can be varied between zero and a maximum value.

Master Cylinder

To model the master cylinder, a force balance was used that combined the input force from the brake pedal and brake booster with the hydraulic forces from the master cylinder [57]. In Figure 4.7 it is shown that the force from the brake booster is applied to a piston in the master cylinder. As the piston moves, the volume of the master cylinder decreases which causes an increase in the brake fluid pressure. This pressure creates the major opposing force on the piston. There is a spring inside the cylinder that is compressed as the piston moves, creating an opposing force that is used to return the piston to its initial position after the braking event is complete. Finally there is a damping force created by the brake fluid when the piston is moving which limits any oscillations in the system.

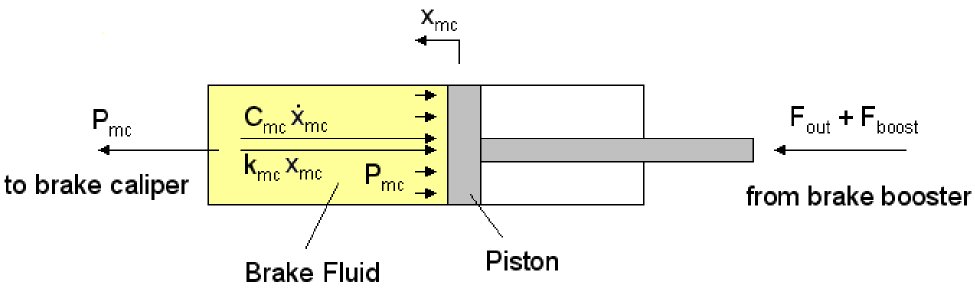

Figure 4.7: Master cylinder schematic

Equation 4.6 was developed by summing the forces applied to the piston. This equation could then be used to solve for the velocity of the piston ($\dot{x}_{mc}$). This velocity could then be used in Equation 4.7 to calculate the derivative of the master cylinder pressure ($\dot{P}_{mc}$) which could be integrated to find the master cylinder hydraulic pressure (P_{mc}).

$$F_{boost} + F_{out} - c_{mc}\dot{x}_{mc} - k_{mc}x_{mc} - P_{mc}A_{mc} = m_{mc}\ddot{x}_{mc} \tag{4.6}$$

$$\dot{P}_{mc} = \beta_{mc}\frac{A_{mc}\dot{x}_{mc}}{V_{mc}} \tag{4.7}$$

Where m_{mc} is the mass of the piston and fluid in the master cylinder, c_{mc} is the damping coefficient of the fluid, k_{mc} is the return spring and fluid spring constant, A_{mc} is the cross sectional area of the master cylinder piston, β_{mc} is the effective bulk modulus and V_{mc} is the volume of the master cylinder, brake lines and brake caliper.

Brake Lines and Brake Caliper

The main purpose of the brake lines and brake caliper is to convert the hydraulic pressure from the master cylinder into braking torque. This is accomplished by using the brake line pressure to squeeze a brake pad against a rotating brake rotor. Figure 4.8 shows how the forces act in a standard automotive braking system.

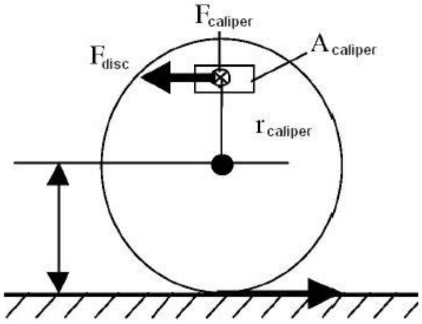

Figure 4.8: Brake caliper and disc forces [57]

To simulate the torque created by the brake pads pressing against the brake disc a first order lag characteristic was assumed between the pressure in the master cylinder and the torque created [43]. The braking torque (T_b) is generated by the frictional force (F_{disc}) of the brake pad against the brake rotor at a distance ($r_{caliper}$) away from the center of rotation. This is shown is Equation 4.8. The frictional force was calculated from Equation

4.9 using the normal force against the brake rotor ($F_{caliper}$) and the friction coefficient of the brake pad against the rotor (μ_{pad}). Using Equation 4.10 the brake caliper converts the master cylinder pressure into a force ($F_{caliper}$) by using the cross sectional area of the caliper piston ($A_{caliper}$) [41].

$$T_b = F_{disc} r_{caliper} \tag{4.8}$$

$$F_{disc} = \mu_{pad} F_{caliper} \tag{4.9}$$

$$F_{caliper} = P_{mc} A_{caliper} \tag{4.10}$$

Combining the previous three equations, the braking torque can be calculated in terms of the master cylinder pressure and later with the first order lag considered. These two steps are shown in Equation 4.11.

$$\begin{gathered} T_b = \mu_{pad} A_{caliper} r_{caliper} P_{mc} \\ T_b(t) = \mu_{pad} A_{caliper} r_{caliper} P_{mc} \left(1 - e^{\frac{-t}{\tau_b}}\right) \end{gathered} \tag{4.11}$$

Flywheel

A flywheel was used to simulate the inertia of a vehicle. The braking torque from above was equated to the product of the polar moment of inertia of the flywheel and shaft (J) and the angular acceleration of the flywheel (α). This equation was then integrated to calculate the angular velocity of the flywheel (ω) and fed back into the simulation model. It was assumed that the frictional torque created by the bearing would be negligible compared to the much larger braking torques.

$$T_b = J\alpha \tag{4.12}$$

Integrating into Matlab

A model of the mechanical braking system was developed in Matlab/Simulink. This was simply done by converting the equations above into Laplace transforms. The Laplace transforms were then implemented into Simulink using the basic transfer function blocks and mathematical blocks. The accelerator and braking inputs were created using signal generators in Simulink and the outputs were stored in Matlab. To solve the model a variable time step ODE45 solver was selected.

4.2.2 Power Electronics System

The power electronics system consisted of three major components: induction motor, inverter and ultracapacitor stack. The ultracapacitor stack is used as the energy storage system, while the inverter converts the direct current into three phase alternating current to power the motor. A schematic of the power electronics system is shown in Figure 4.9.

The power electronics system was modelled using Matlab/Simulink with Samy Ghania and Simon Stark. Predefined power electronic blocks were used for the motor, inverter and ultracapacitor systems within Matlab/Simulink.

Induction Motor, Inverter and Ultracapacitor Stack

To simulate the induction motor, a predefined Matlab/Simulink asynchronous machine was used from the power systems library. A squirrel cage rotor and angular velocity input were selected from the presets and the internal parameters of the motor were selected based on information obtained from the Baldor ZDWNM3609T induction motor data specification sheet summarized in Table 4.1.

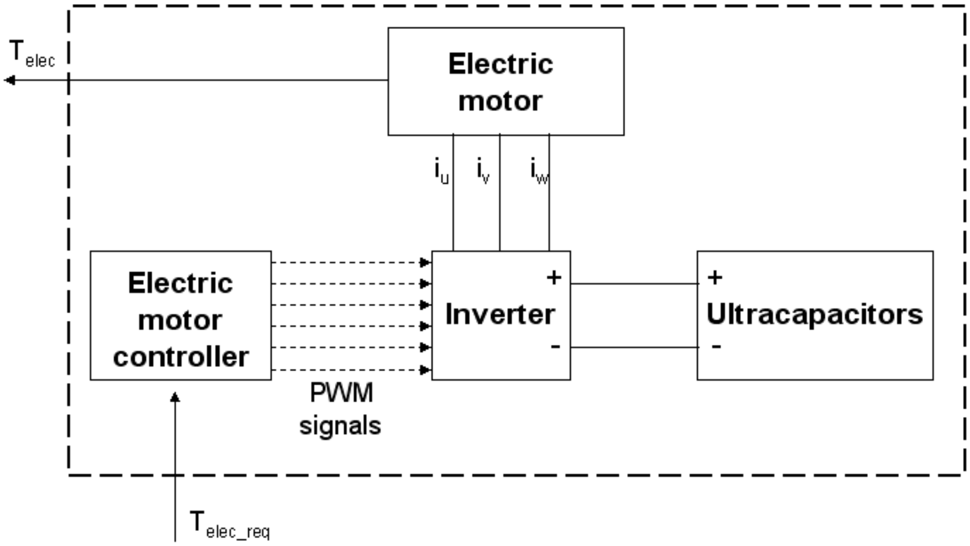

Figure 4.9: Power electronics schematic

Parameter	**Value**
Horsepower	2 hp
Angular Speed	1725 rpm
Resistance Inductance	3.04 ohm
Self Inductance	164 ohm
Leakage	5.51 ohm

Table 4.1: Baldor ZDWNM3609T induction motor parameters

A predefined Matlab/Simulink block was also used to model the inverter used in the regenerative braking system. A universal bridge in the power systems library was used, which consisted of a snubber circuit connected in parallel with a switching device. IGBT's were selected as the switching devices.

The ultracapacitor stack was modelled using a simple series resistor capacitor branch from the Simulink library. The capacitance was calculated using equations from Chapter 2.3 and the Maxwell BCAP008 ultracapacitor data sheet summarized in Table 4.2.

Parameter	Value
Capacitance	1800 F
Voltage	2.5 V
Internal Resistance	0.0009 ohm
Rated Current	450 A
Power	2080 W/kg

Table 4.2: Maxwell BCAP008 ultracapacitor parameters

Integrating into Matlab

The power electronics system was modelled using Matlab/Simulink with the help of Samy Ghania and Simon Stark. A discrete time step of 1 e^{-5} seconds was used for the simulation with the ODE23 solver. This short time step was required because of the high frequency (1 kHz) of the PWM signals. As mentioned above, predefined Simulink power electronic blocks were used for the motor, inverter and ultracapacitor systems.

4.2.3 Control Systems

The purpose of the control systems was to distribute and blend the torque from the mechanical braking system and the regenerative braking system. There were three different controllers used for the system. The overall controller distributed the required torque between the mechanical and regenerative braking systems, while the mechanical brake control system and the electric motor control system controlled the physical mechanical and regenerative brake torque generated. An overview of these systems is shown in Figure 4.10.

Overall Controller

The objective of the overall controller was to distribute the braking torque between the mechanical braking system and the regenerative braking system in the most efficient manner possible. There were two control systems created to blend the mechanical and regenerative braking of the testbench. The first system created by the author was a simple

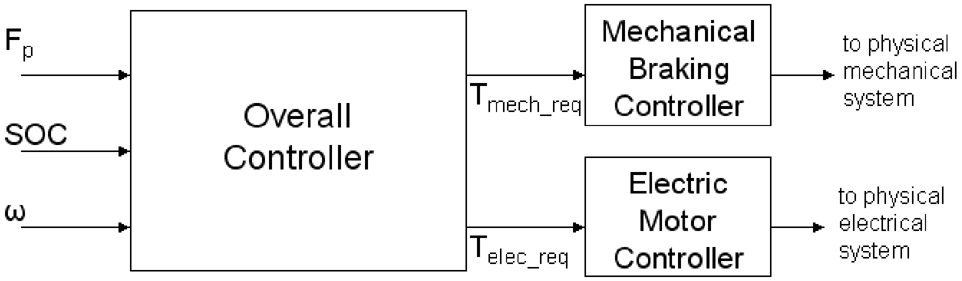

Figure 4.10: Overview of the control systems

parallel regenerative braking scheme developed in Matlab/Simulink where the amount of regenerative braking was always equal to the amount of mechanical braking. This system is common on vehicles that cannot attenuate the mechanical braking. The second control system for the regenerative braking testbench was developed by Simon Stark and the author and was based on a series regenerative braking scheme. This system was developed to show the advantages of the brake booster attenuation system over a brake system that cannot independently control the mechanical braking. To develop this control system, an interactive design and simulation program called Stateflow was used within Matlab/Simulink. Stateflow is a graphical design and development tool for simulating complex reactive systems based on finite state machine theory [21]. The purpose of this system was to control the brake distribution between the regenerative braking system and the mechanical braking system using inputs from the system and outputs from the Stateflow control chart. Figure 4.11 shows an overview of the inputs and outputs of the control system.

The Stateflow chart contains three input ports and two output ports. The three input ports are listed as follows:

- pedal force (F_p)
- ultracapacitor state of charge (SOC)
- rotational velocity of the electric motor (ω)

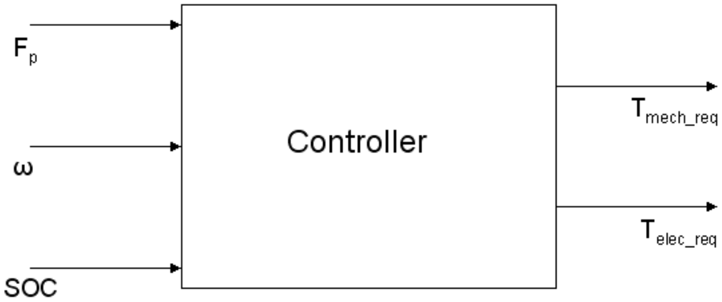

Figure 4.11: Controller inputs and outputs

These three inputs can then be used to calculate the following inputs to the Stateflow control chart:

- driver brake torque demand (T_{demand}) which is proportional to F_p
- maximum regenerative braking torque available (T_{max_regen}) which is proportional to ω
- ultracapacitor state of charge (U_{SOC}) which is equivalent to SOC
- angular velocity of the electric motor (ω_{motor}) which is equivalent to ω
- rate of change of pedal force with time (dF_{pedal}) which is the derivative of F_p

The two outputs are used to distribute the braking torque between the mechanical and regenerative brakes and are listed below:

- regenerative braking torque (T_{elec_req})
- mechanical braking torque (T_{mech_req})

Besides the inputs and outputs there were also two threshold constants used within the Stateflow control chart. They are listed as follows:

- maximum rate of change of pedal force with time ($dF1$)

- maximum state of charge (SOC)

The Stateflow control chart consisted of two major states: the ‘Off’ state and the ‘Brake’ state (Figure 4.12). The ‘Brake’ state is only active when the brakes are applied and the angular velocity of the electric motor is not zero. During all other events, the control system is in the ‘Off’ state giving outputs of zero from the control system. A simple overview control schematic is shown in Figure 4.13.

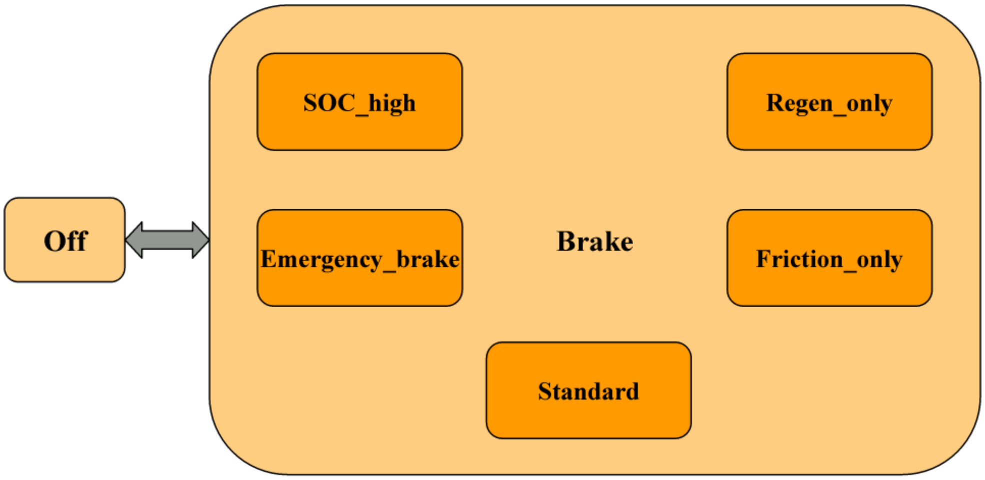

Figure 4.12: Stateflow control system simplified [49]

The ‘Brake’ state consists of five different substates that can transition among each substate depending on the input conditions to the Stateflow control system (Figure 4.12). The five substates are as follows:

- $Standard$ Substate
- $Regen\_only$ Substate
- $Friction\_only$ Substate
- $Emergency\_brake$ Substate
- SOC_high Substate

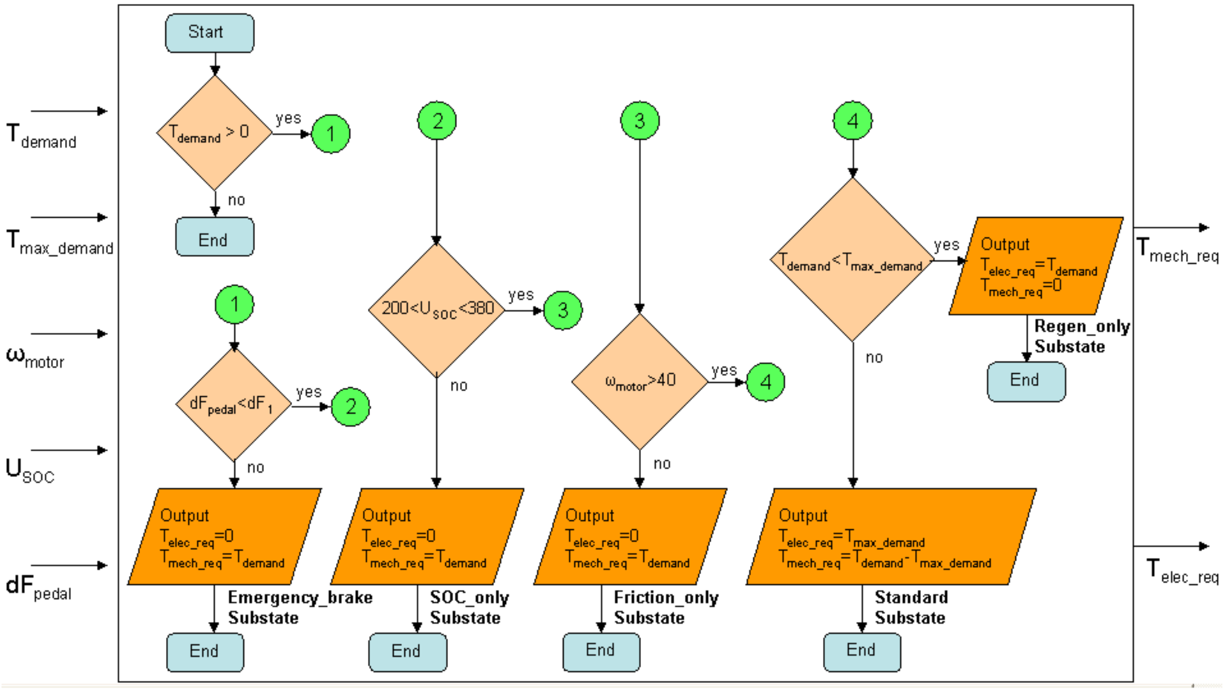

Figure 4.13: Overall control scheme

Standard Substate

The *standard* substate is activated during normal braking operations when the driver demanded brake torque (T_{demand}) is greater than the maximum regenerative brake torque available (T_{max_regen}) at the current angular speed. During this substate, the maximum regenerative braking torque available is output as the regenerative braking torque (T_{elec_req}) to ensure high regenerative braking efficiency, while the remainder of the demanded braking torque is supplemented by the mechanical braking system (T_{mech_req}).

Regen_only Substate

During braking operations when the driver demanded brake torque is less than the maximum regenerative brake torque available, the entire demanded brake torque is delivered by the regenerative braking system to store as much energy in the energy storage system as possible. The maximum regenerative braking torque available is calculated using a look-up table based on the flywheel angular velocity. The look-up table was developed experimentally using the simulation. The flywheel was accelerated to the maximum angular velocity where a larger than possible regenerative braking torque was requested. The actual regenerative braking torque was then measured with the flywheel angular velocity and used for the look-up table.

$Friction\_only$ **Substate**

The $friction\_only$ substate is activated when the angular velocity of the flywheel drops below a predefined value in which there is not enough kinetic energy to produce high enough voltages to be fed back into the ESS. If regenerative braking was to be used during this period, energy would actually be absorbed from the ESS because the regenerative voltage would be too low and there is no DC to DC converter used to boost the voltage from the motor during the simulation.

$Emergency\_brake$ **Substate**

During braking events when the rate of change of the pedal force with time (dF_{pedal}) is above a predefined value ($dF1$), no regenerative braking is used and all the braking torque is produced by the mechanical braking system. This is done to ensure that no longitudinal or lateral instabilities will occur from the blending of the mechanical and regenerative braking if this system was incorporated into a vehicle.

SOC_high **Substate**

If the state of charge (U_{SOC}) of the ESS goes above a predefined level, the control system will discontinue regenerative braking and use mechanical braking exclusively. This is done as a precaution to ensure that the ESS is never damaged by overcharging.

Mechanical Brake Controller

The purpose of the mechanical brake controller was to control the torque created by the mechanical brake system so that it would follow the torque received from the overall controller.

Solenoid Valves (Alternate 1)

As mentioned above, the mechanical braking torque can be controlled by either opening valve 1 or valve 2. To control the solenoid valves, a Schmidt trigger was developed. The controller converts the required mechanical torque signal (T_{mech_req}) into its corresponding brake line pressure demand (P_{demand}) using a look-up table. The brake line pressure (P_{mc}) from the mechanical brake system is then used as a feedback to the system and compared with P_{demand}. If the master cylinder pressure is 7 percent greater than the brake line pressure demand, valve 1 would be activated which would bring atmospheric air into the constant pressure chamber of the brake booster reducing the pressure differential and thus the brake line pressure. If the brake line pressure demand is 7 percent greater than the master cylinder pressure, valve 2 would be activated which would draw air out of the brake booster into the accumulator resulting in an increase in brake line pressure. An overview of the Schmidt trigger control scheme is shown in Figure 4.14.

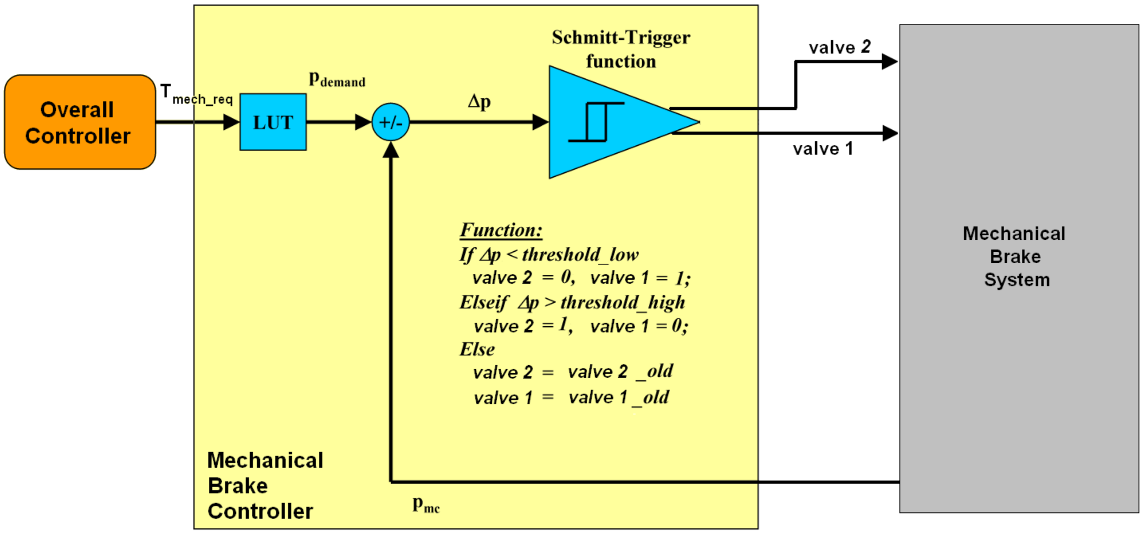

Figure 4.14: Schmidt trigger control scheme [49]

Proportional Control Valves (Alternate 2)

In order to control the proportional control valves, a PID controller was implemented. The coefficients for this controller can be seen in Table 4.3. This controller fully opens valve 1 if the master cylinder pressure (P_{mc}) is 20 percent greater than the brake line pressure demand (P_{demand}) and fully opens valve 2 if the brake line pressure demand (P_{demand}) is 20 percent greater than the master cylinder pressure (P_{mc}). If the error is between the predefined values then the controller varies the air flow proportional to the error measured. By using these proportional control valves, the system can follow the requested brake line pressures more accurately. An overview of the PID control scheme is shown in Figure 4.15.

Coefficient	Value
Proportion	10
Integral	0.2
Derivative	0.1

Table 4.3: PID controller coefficients

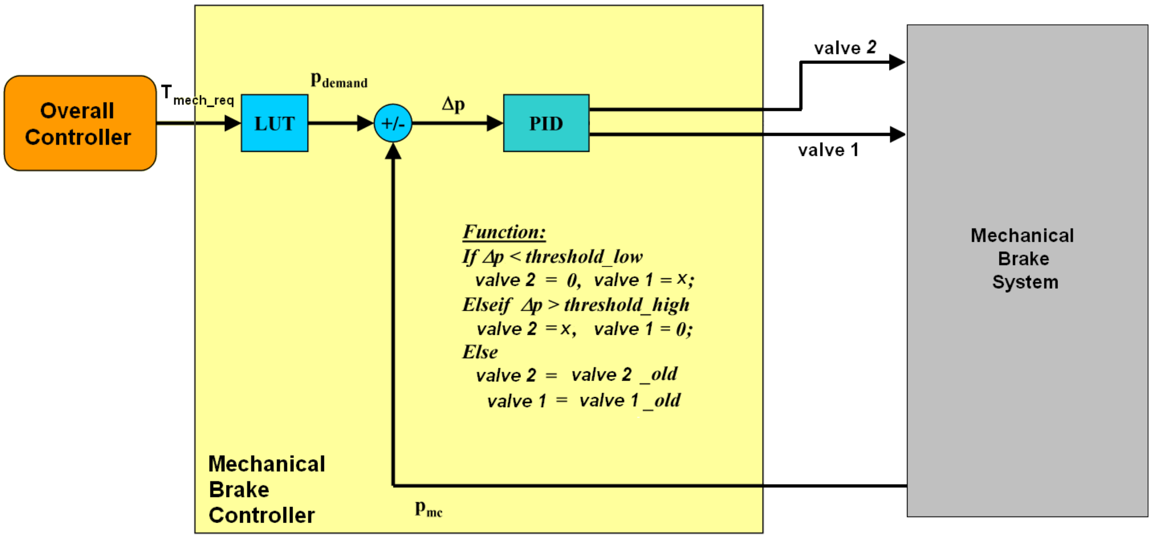

Figure 4.15: PID control scheme [49]

Electric Motor Controller

The purpose of the electric motor controller is to control the actual torque output from the three phase AC induction motor so that it will follow the torque received from the overall controller. In order to accomplish this task a closed loop vector control was created.

Implementation of Vector Control

The simulation of the vector control was implemented by Samy Ghania and the author using Matlab/Simulink. In this section, the basics of vector control will be described using block diagrams and traditional methods. It has been shown in Chapter 2 that i^r_{ds} and i^r_{qs} must be controlled to provide good dynamic control of the induction motor [11]. Using closed loop control, calculated values of i^r_{ds} and i^r_{qs} are compared with the actual values measured from the motor. To obtain the motor values, the measured three phase stator currents are transformed into direct and quadrature components of the rotating reference frame. The resulting error term is then transformed into an updated three phase current signal. This updated three phase current signal is then converted into a PWM signal using relays and logic operators and sent to the simulink inverter model where the actual three phase current is output. Figure 4.16 shows a control block diagram of this process.

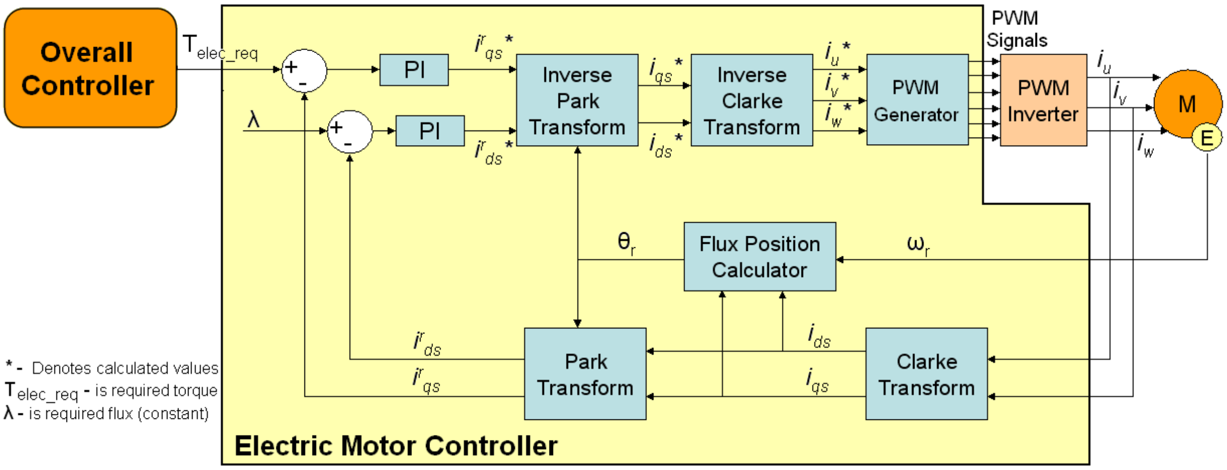

Figure 4.16: Block diagram for vector control of an induction motor [11]

The flux position calculator is used to produce the correct field orientation by ensuring the alignment of i_{ds} with the rotor flux [50]. The angular position of the rotor flux can either be measured directly using sensors embedded in the motor or measured indirectly. The indirect method involves calculating the angle of slip between the stator and rotor fields using known characteristics of the rotor and summing this with the physical position of the rotor, which is usually measured using an incremental encoder fitted to the motor shaft. The difference between the actual and calculated i^r_{ds} and i^r_{qs} components are then input to proportional integral (PI) controllers for optimum closed loop control. The outputs from the PI controllers are then transformed back to the static frame using the inverse Park transform and transformed from the static frame to the three phase components using the inverse Clarke transform (Equations 4.13 and 4.14).

$$
\begin{gathered}
i_u = i_{ds} \\
i_v = \frac{\sqrt{3}}{2}(i_{qs}) - \frac{1}{2}(i_{ds}) \\
i_w = -i_u - i_v
\end{gathered}
\tag{4.13}
$$

$$
\begin{aligned}
i_{ds} &= i^r_{ds}\cos(\theta_r) - i^r_{qs}\sin(\theta_r) \\
i_{qs} &= i^r_{ds}\sin(\theta_r) + i^r_{qs}\cos(\theta_r)
\end{aligned}
\tag{4.14}
$$

Regenerative Braking

To initiate regenerative braking in the system, a negative torque value has to be requested by the control system. This will cause the torque component of current (i^r_{qs}) to decrease which will in turn reduce the frequency of the three phase current. Since the inertia of the system will not allow the speed to change instantaneously, negative slip will be created, resulting in the motor generating current. When the rotational speed of the flywheel is reduced below a certain value, the voltage produced during regenerative braking will be less than the ultracapacitor stack voltage and will draw energy away from the ultracapacitors. Since no DC-DC converter was used to boost the voltage produced during regenerative braking, a switch was implemented into the model to cut power between the induction motor/controller and the ultracapacitor stack. The switch was triggered when the velocity of the flywheel dropped below a predefined value (30 rad/s) creating an open circuit.

4.3 Simulation Results

The simulation results were used to demonstrate the regenerative braking efficiency advantages of using the brake booster attenuation system over a simpler parallel regenerative braking system. The results also showed the functionality of the system to distribute and blend the braking forces between the mechanical and regenerative braking systems, using the requirements of the project definition.

4.3.1 Regenerative Braking Feasibility

To ensure regenerative braking was possible with the induction motor before the testbench was built, simulations were conducted using the Matlab/Simulink program described in the section on the virtual prototype. From these simulations, it was possible to refine the vector controls and PWM during regenerative braking as well as analyzing the effects of different conditions on regenerative braking efficiency. Unless specified, all simulations in this section involved accelerating the flywheel for the first seven seconds of the simulation to approximately 70 rad/s before the brake was applied. This was done to ensure that the same amount of kinetic energy was given to the flywheel for each test conducted. This then allowed different regenerative braking events to be conducted and the results to be compared against each other.

Vector Control

It was found that during the commencement of regenerative braking shown in Figure 4.17a, the torque controlling component (i_{qs}^r) had to be exponentially ramped down to create a smooth transition from motoring mode into generating mode. During regenerative braking, the flux controlling current (i^r_{ds}) was held constant. Ramping down the torque controlling current in the vector control, in reality caused the rotating stator flux speed to be less than the motor speed, producing negative slip. This caused increased three phase currents from the motor shown in Figure 4.17b, which were then fed into the ESS, raising the SOC.

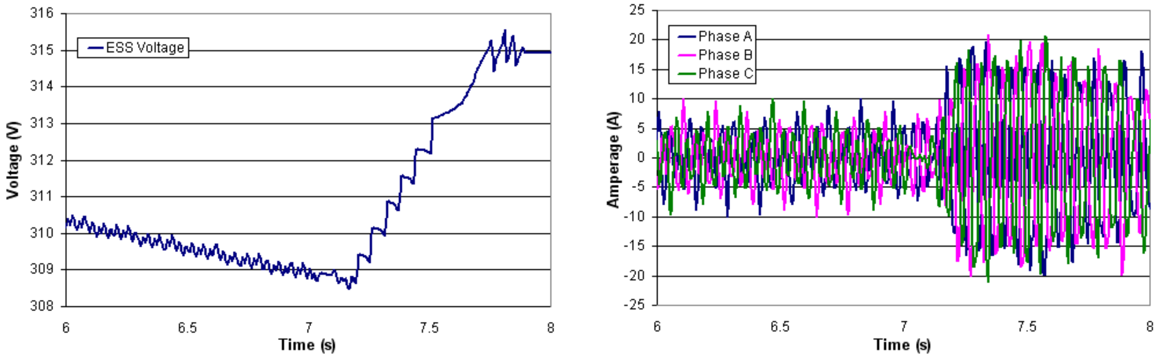

(a) SOC during commencement of regenerative braking

(b) Ramping of three phase currents

Figure 4.17: Commencement of regenerative braking - effects on the three phase currents and the ESS voltage, regenerative braking begins at t = 7s and only a portion of the process is shown

The simulation was also used to evaluate how the regenerative braking system reacted when the angular velocity of the flywheel was low. From the simulations, it was found that regenerative braking of the flywheel below certain angular velocities resulted in voltages that were too low to be fed back into the ESS and actually consumed energy during braking. To remedy this problem, an ideal switch was added to the system that would create an open circuit with the ESS when the angular velocity of the flywheel was below 30 rad/s. The results with and without the power switch are shown in Figure 4.18. During approximately the first second of regenerative braking, energy is stored in the ESS. However, after this time if the switch is not used, energy flows out of the ESS again.

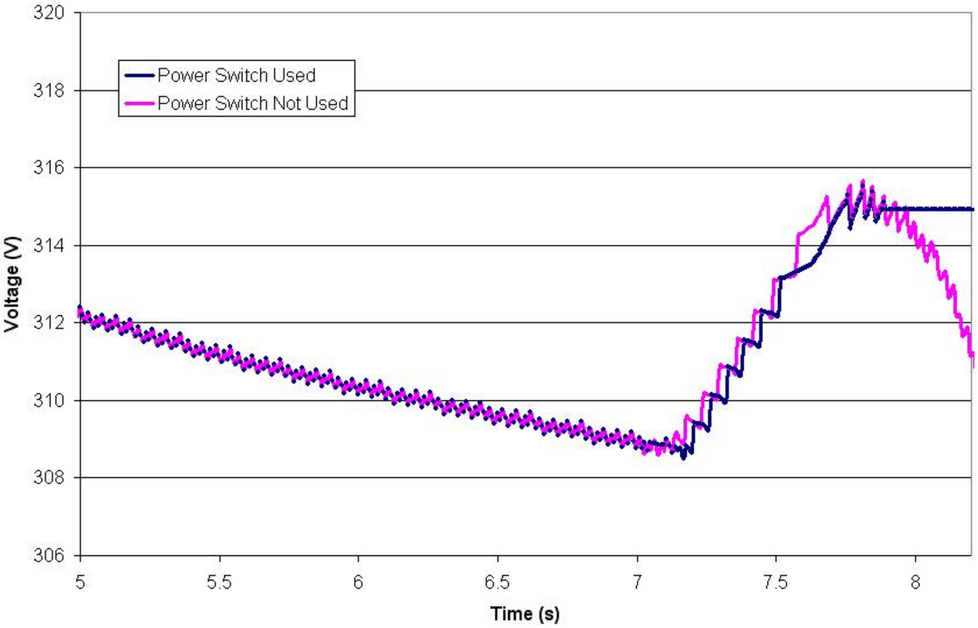

Figure 4.18: Ultracapacitor stack voltage with and without power switch - regenerative braking begins at t = 7s and only a portion of the process is shown

Regenerative Braking Efficiency

Once the vector control was optimized, it was found that different braking conditions contributed greatly to the overall efficiency of the regenerative braking system. The regenerative braking efficiency can be calculated using Equation 4.15 shown below. Where $SOC_{initial}$ is the initial state of charge, SOC_{final} is the final state of charge and SOC_{lowest} is the lowest state of charge.

$$\eta_{regen} = \frac{SOC_{final} - SOC_{lowest}}{SOC_{initial} - SOC_{lowest}} \tag{4.15}$$

It was found that light braking events over longer periods were more efficient than quick, hard braking operations. Figure 4.19 shows the SOC of the ultracapacitor bank when accelerating the flywheel from 0 to 70 rad/s and then braking the flywheel at t = 7s using different driver braking demands. The reason for this trend can be explained by the pedal force applied by the driver. During these tests, the brake booster attenuation system always requested zero braking demand which causes the boost from the brake booster to be zero. However, the pedal force was still able to transmit a small braking force through the brake booster causing mechanical braking torque. As the braking demand increased the amount of mechanical braking increased which reduced the amount of electrical energy stored in the ultracapacitors and thus the regenerative braking efficiency.

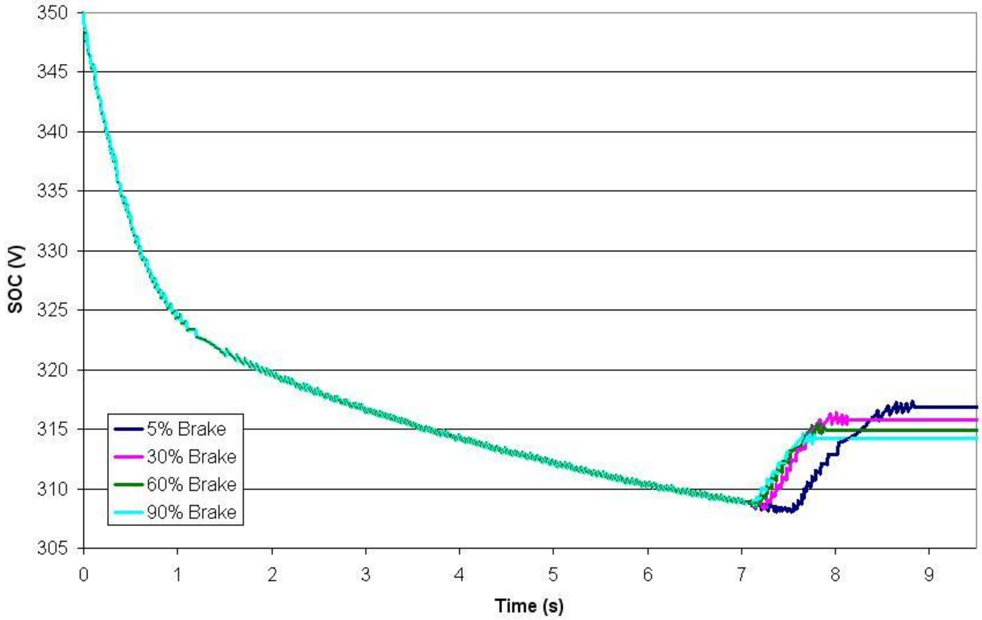

Figure 4.19: Energy recaptured into the ESS using different driver braking demands

In Table 4.4 the regenerative braking efficiencies from Figure 4.19 are shown. It can be concluded from these numbers that to maximize regenerative braking, light driver braking demands should be employed.

Since a DC to DC converter was not used in these simulations, the regenerative energy was no longer able to flow into the ESS effectively when the flywheel dropped below approximately 40 rad/s. This resulted in lower than expected regenerative braking efficiencies during the simulation. However, in a test done where the flywheel is accelerated from 40 rad/s up to 70 rad/s and then braked back down to 40 rad/s, the efficiency of this cycle was much higher than the previous results. Figure 4.20 shows the results of this test and Table 4.4 shows the efficiencies.

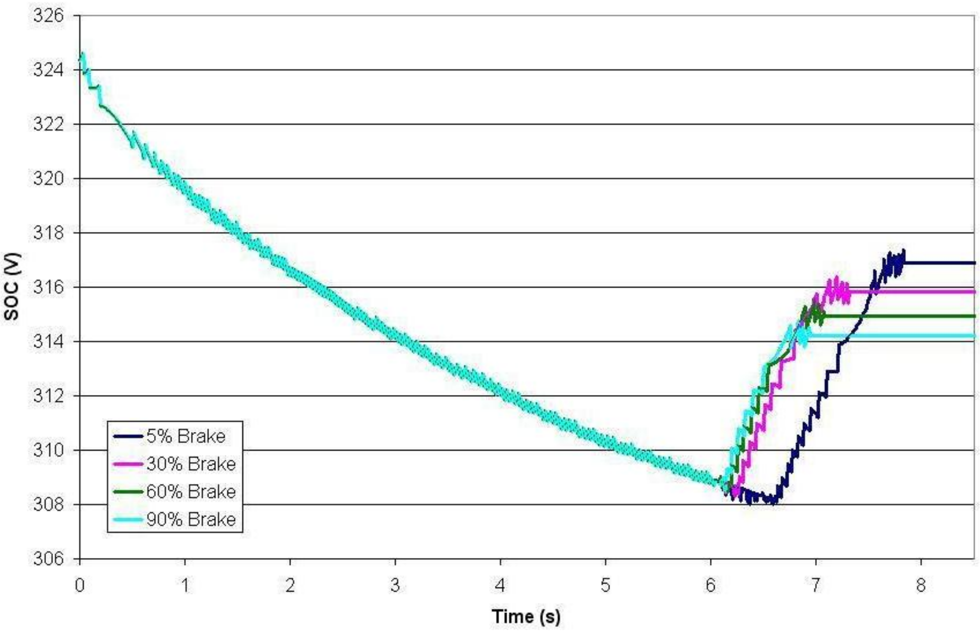

Figure 4.20: Energy recaptured into the ESS using different driver braking demands - new drive cycle

	Driver Braking Demand			
	90% Demand	**60% Demand**	**30% Demand**	**5% Demand**
Efficiency	13.77%	15.21%	17.74%	21.13%
Efficiency - new cycle	34.60%	38.43%	44.52%	51.22%

Table 4.4: Regenerative braking efficiency using different driver braking demands

4.3.2 Brake Booster Attenuation Concept (Alternate I)

To ensure that the solenoid valves could be used to control the pressure in the brake booster and subsequently the mechanical braking torque, the valves were modelled in the brake booster system and a Schmidt trigger control scheme was implemented. In Figure 4.21 the first test of this system can be seen. The results from this test showed many concerns with both the control scheme and the valve models. In Figure 4.22 the Schmidt trigger was modified to open and close the valves sooner than required to take into consideration the time delay of the valves caused by the valve inertia. This removed the oscillations from the system as it tracked the control signal. The transfer functions representing the valves were then modified to more realistically model the flow of air during the valve opening operation and the valve closing operation. The results from the final test showed that the mechanical torque from the simulation tracked the control signal much better. The modifications to the Schmidt trigger reduced the oscillations created when the pressure in the brake booster was electro-mechanically controlled and allowed for a much smoother braking torque.

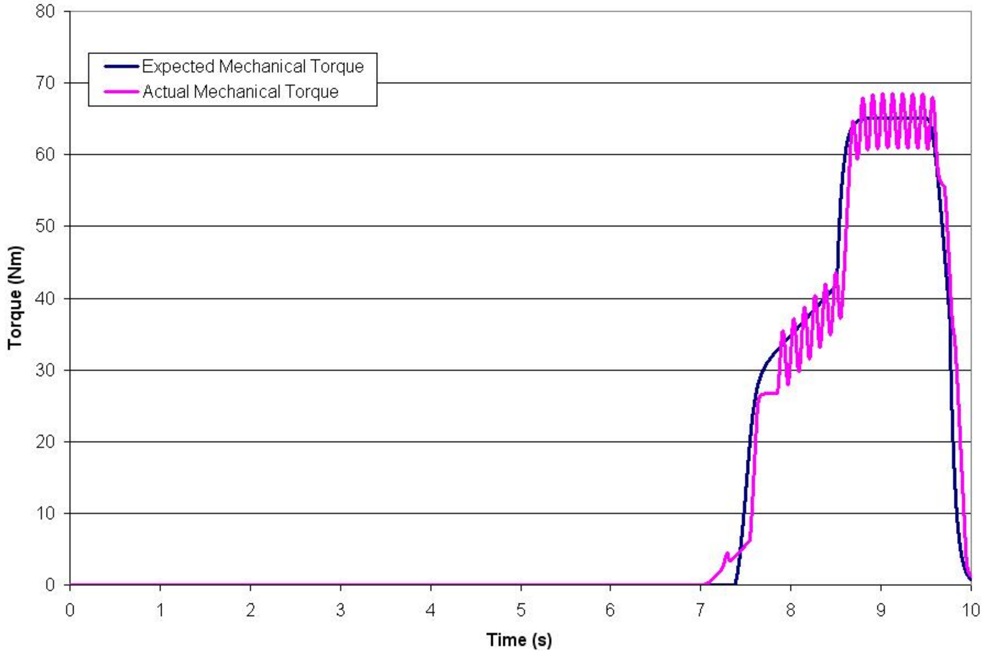

Figure 4.21: Results from first brake booster attenuation test - brake applied at t = 7s

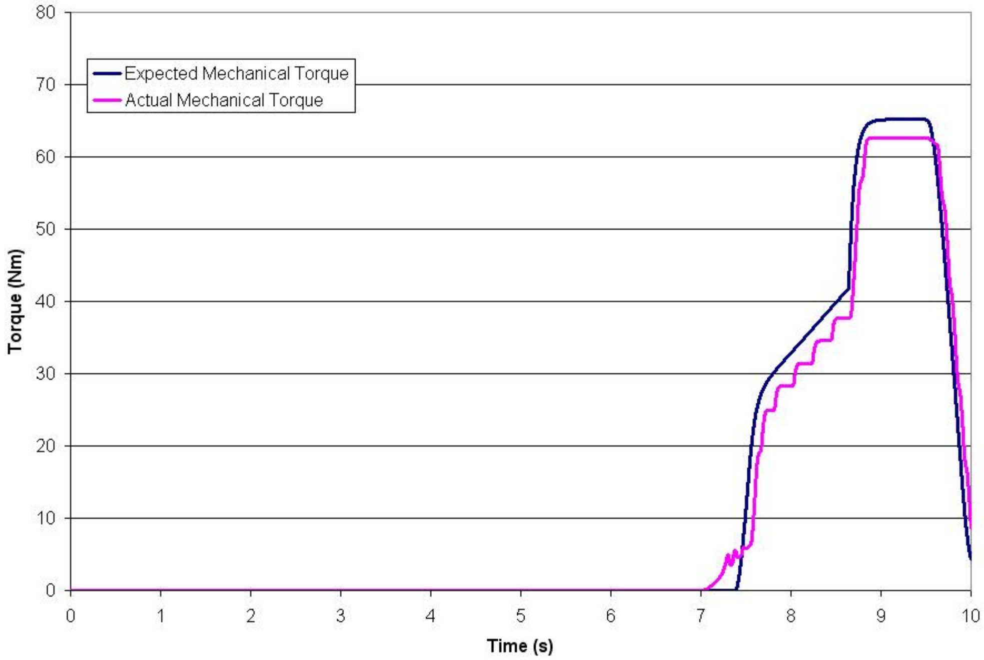

Figure 4.22: Results from brake booster attenuation test after Schmidt trigger and valve modifications - brake applied at t = 7s

Simulations were also used to substantiate the claim that brake booster attenuation could improve the regenerative braking efficiency for an HEV when compared to a parallel regenerative braking discussed in Chapter 2. To test this claim, two test simulations were set up using identical braking demands of 60 percent for both systems. In the first test run, the brake booster attenuation concept was used and in the second test run, a simple parallel braking strategy was implemented. The results from these simulations are shown in Figure 4.23 using the state of charge of the ultracapacitor bank.

From these results it was also possible to calculate the regenerative braking efficiencies and it was found that the efficiency of the simulation using brake booster attenuation was 34.6%, whereas the simulation using a simple parallel regenerative braking strategy showed a regenerative braking efficiency of 17.7% or approximately half. The efficiencies of both systems were dependent on the braking demand, however the proportion of the brake booster attenuation system being approximately twice as efficient stayed the same.

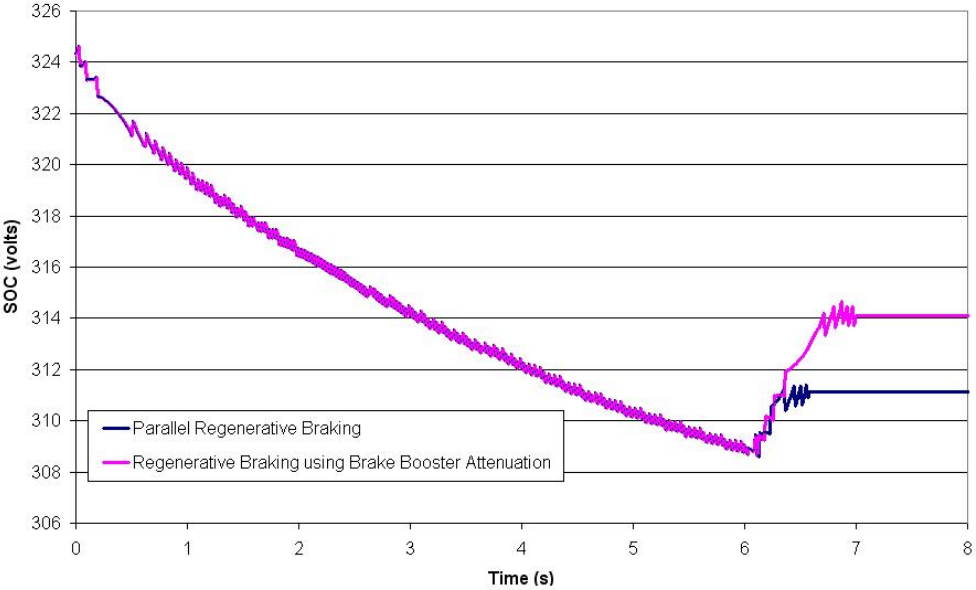

Figure 4.23: Comparison of energy recaptured between parallel and brake booster attenuation braking - Drive cycle accelerated the flywheel from 40 rad/s to 70 rad/s and back to 40 rad/s at t = 6s using a 90% braking demand

4.3.3 Brake Booster Attenuation Concept (Alternate II)

To improve the dynamic response of the system, it was decided to replace the solenoid valves used in Alternate I with proportional control valves and a PID controller. Since the solenoid valves used in Alternate I can only be either 'on' or 'off' a Schmidt trigger was used instead of a PID controller and therefore little tuning could be conducted. However, tuning the PID controller was possible with Alternate II and was completed before the two systems could be compared.

PID Controller Tuning

In order to control the flow rate of the proportional control valves, the error between the actual and required brake line pressure was input into a PID controller and a flow rate was output in Matlab/Simulink. The flow rate was saturated at the maximum flow rate of the valves and when the error was less than one percent, the valves were closed. Since the complexity of the system made creating the plant transfer function difficult, the controller was tuned by trial and error. The first test was conducted with the proportional, integral and differential gains all equal to one. A simple step input was used as the control signal and the results from this test can be seen in Figure 4.24.

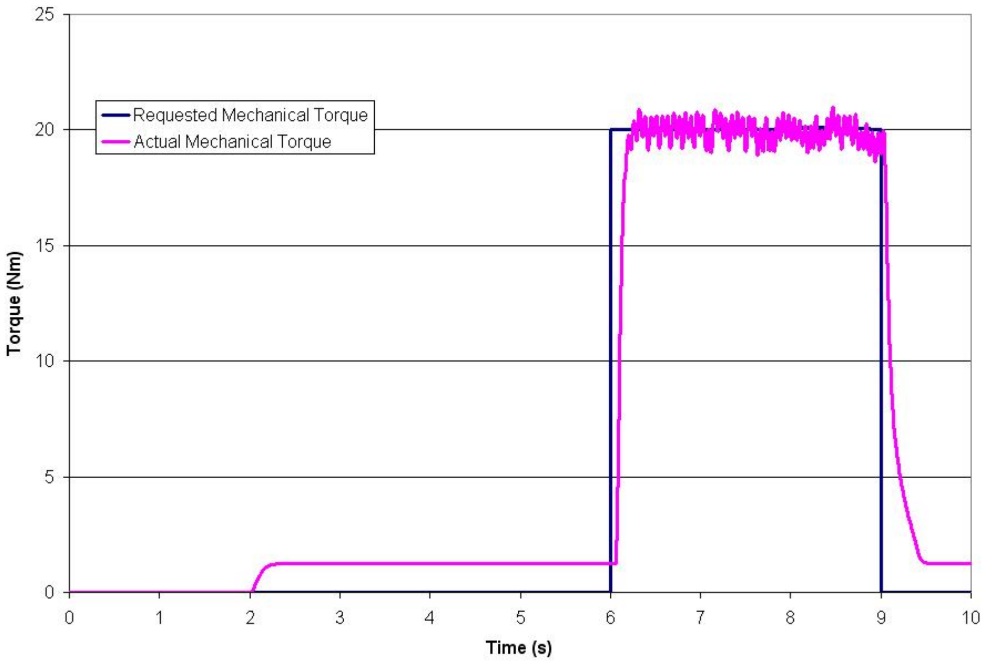

Figure 4.24: Comparison of the actual and expected mechanical braking torque - before PID controller was tuned

It was obvious from the first test that the current PID settings caused the response of the system to be extremely noisy during constant torque events. To eliminate this noise, both the integral and differential gains were reduced significantly and the system was retested. This completely eliminated the noise created during the constant torque portion of the simulation. The last step was to try and improve the response time of the system. To do this, the proportional gain of the controller was increased. However, the inherent lag of the inertia and air dynamics of the brake booster did not allow for much improvement. The results from the final test are shown in Figure 4.25. The proportional control valves have the ability to allow the actual brake torque to follow the required brake torque with less than 1 percent error compared to the 7 percent error of the Alternate I system. However the cost of these valves can vary from 3 times to 10 times more expensive than ordinary solenoid valves.

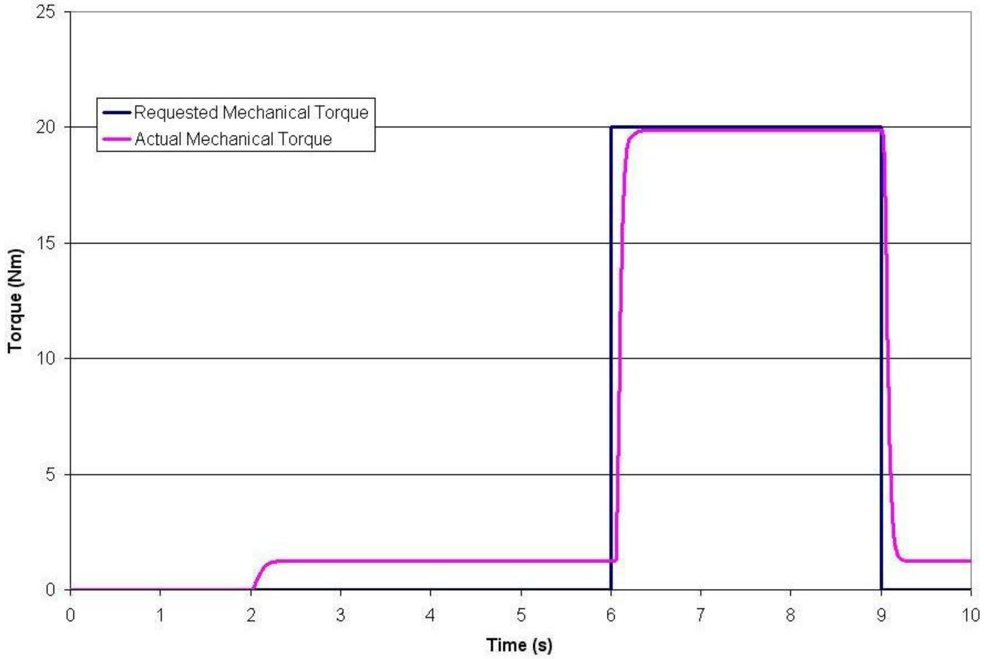

Figure 4.25: Comparison of the actual and expected mechanical braking torque - after PID controller was tuned

4.3.4 Brake Distribution Control System

Once the brake booster attenuation system and the electric motor vector control were optimized, it was then possible to test how well the brake distribution control system was able to distribute and blend the braking torque between the regenerative and the mechanical braking systems. For this test, simulations were run in which the electric motor drove the flywheel (negative torque in figures) for the first seven seconds after which a regenerative braking command was conducted (positive torque). The control signals were then compared with the actual results of the simulations. These simulations were first run using the Alternate I system and then resimulated using the Alternate II system.

Brake Booster Attenuation Concept (Alternate I)

Blending and Tracking of the Mechanical and Regenerative Braking Torques

Figure 4.26 shows the results from the total braking torque expected from the control system and the actual braking torque of the simulation. The results show that the actual total braking torque tracks the control signal very well; there is a slight time lag between the actual and control signal but this was well within acceptable ranges. The blending of the mechanical and regenerative braking torques was accomplished very smoothly. There was a slight ripple during the constant braking portion of the test while blending the two braking torques (from 7.5 to 9.5 seconds), however it was small, less than 2 Nm (3.33%) and was below the 5 Nm limit set in the project definition of Chapter 3.

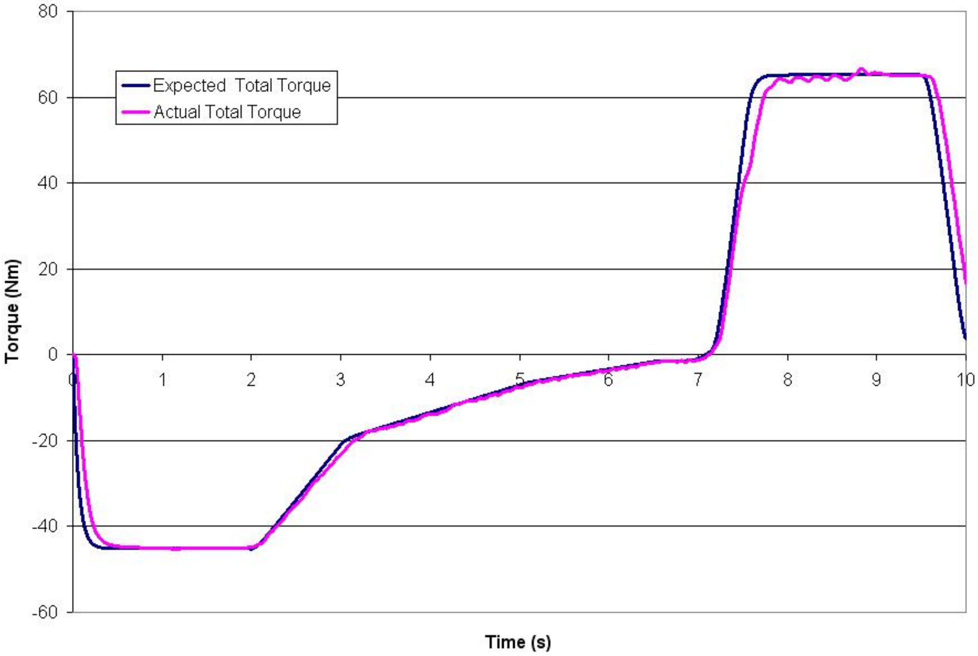

Figure 4.26: Comparison of the actual and expected total brake torque - brake applied at t = 7s

Figure 4.27 shows the results from rotational speed expected by the control system and the actual rotational speed from the simulation. The curve shows a smooth transition between the regenerative and the mechanical braking system, while keeping the stopping time within 0.2 seconds of the expected time. The control system could be modified to increase the amount of torque required to reduce the error between the expected and actual time, but the error was so small that it was not deemed necessary.

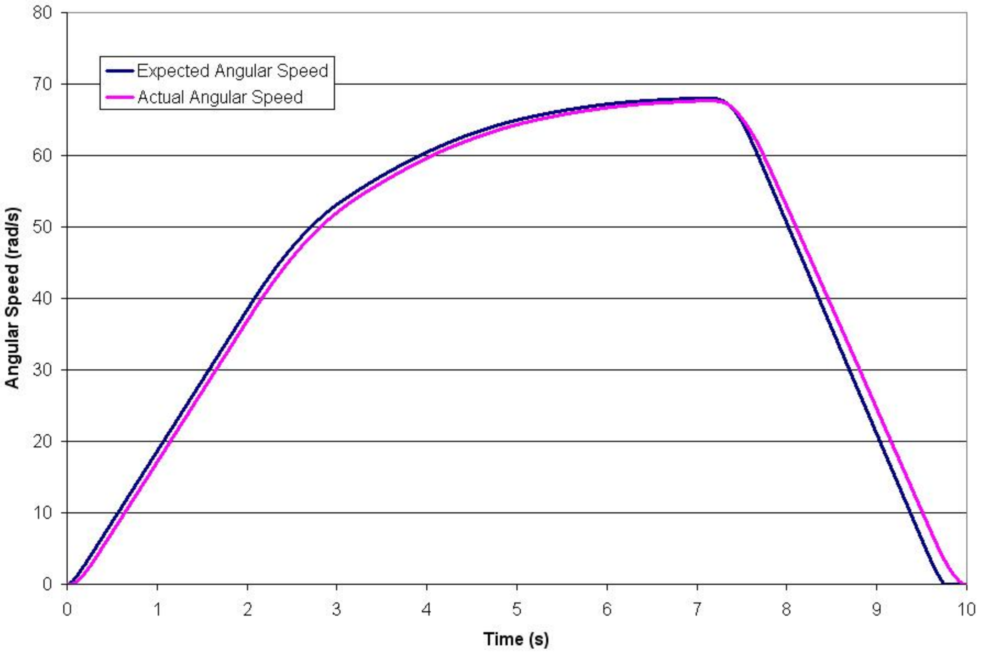

Figure 4.27: Comparison of the actual and expected angular velocity

Mechanical Friction Brake Comparison

As seen in a previous section, the mechanical friction brake tracked the control signal very well (Figure 4.22). However, there was some discrepancy during the initiation of the braking sequence. During this period, the control system wanted the entire braking torque to be completed by the regenerative braking system. This resulted in the brake booster attenuation creating a zero pressure differential between the constant and dynamic pressure chambers in the brake booster. However, some of the pedal force was still transferred through the brake booster and created the small brake force seen during the initiation of the braking event. Since the transferred force was less than 10 percent of the total braking force, it was deemed acceptable.

Motor Torque and Regenerative Brake Comparison

Figure 4.28 shows the comparative results of the expected regenerative brake and motor torque from the control system, and the actual torque taken from the simulation. From this figure, it is shown that during motoring (negative torque) the actual torque follows the control torque extremely well with a very small time lag. The transition from motoring to regenerative braking occurs very smoothly and the actual regenerative braking torque follows the control torque as well as it did during the motoring portion. It is important to realize that the regenerative braking torque is not large enough to perform all of the braking event even at high flywheel speeds. The reason for this lack of regenerative braking torque is that the power rating of the motor was selected based on acceleration and not braking. This results in a system that will not fully use the regenerative braking capacity of the ultracapacitors and will thus lose some regenerative braking efficiency.

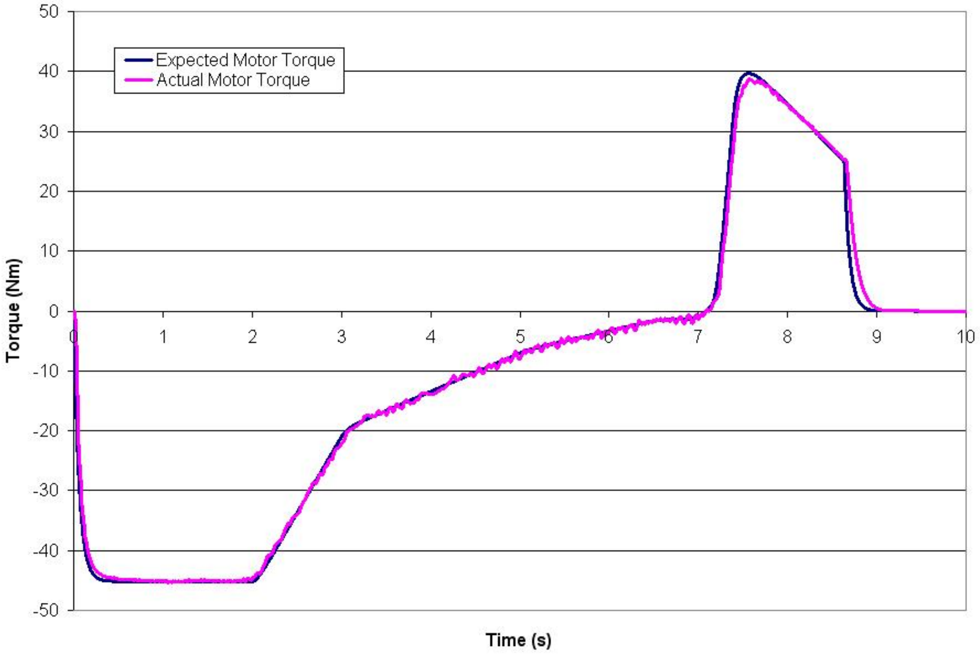

Figure 4.28: Comparison of the actual and expected electric motor torque - brake applied at t = 7s

Brake Booster Attenuation Concept (Alternate II)

Blending and Tracking of the Mechanical and Regenerative Braking Torques

The results from the simulation of the expected and actual total torques using the proportional control valves can be seen in Figure 4.29. When comparing these results with the results found previously in Figure 4.26, it can be seen that the tracking of the system with the proportional control valves is almost identical to the tracking of the system with the solenoid valves. However, the benefits of the system with the proportional control valves can easily be seen during the constant braking torque portion of the curve (around 8.5 seconds). During this portion, the blending of the two braking torques is done almost seamlessly with the only ripple occurring when the system changes to only mechanical braking.

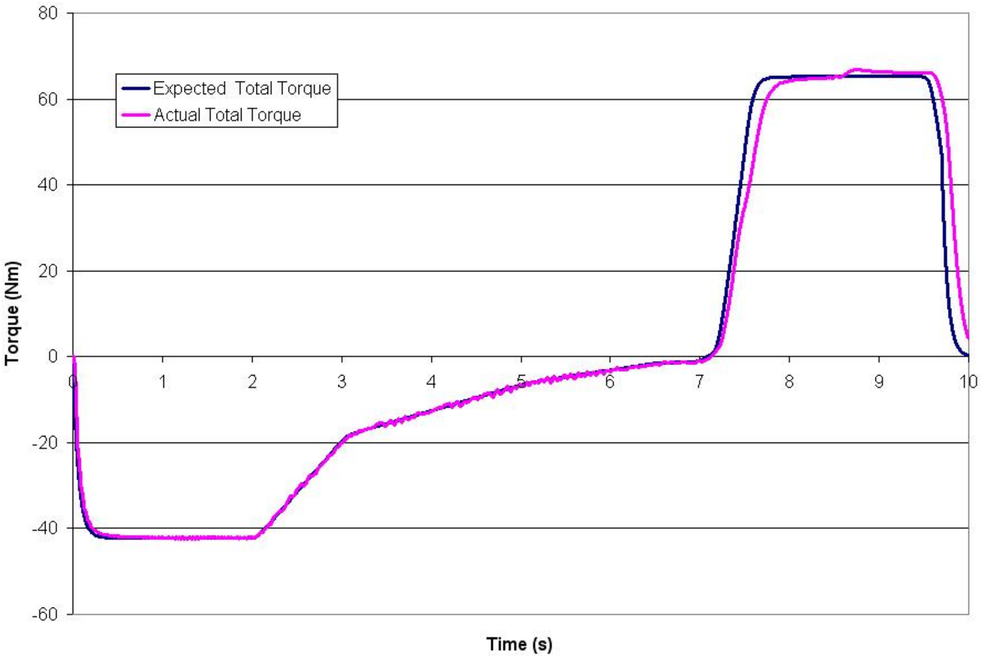

Figure 4.29: Comparison of the actual and expected total brake torque - brake applied at t = 7s

The benefits of this system can also be seen when comparing the angular velocity results of both systems. In Figure 4.30 the results from the Alternate II system show how well the actual angular velocity tracks the expected angular velocity. Both the actual and expected angular velocities from the simulation come to a stop at almost identical times, whereas in Figure 4.27 it can be seen that the actual stopping time lags the expected stopping time by about 0.2 seconds.

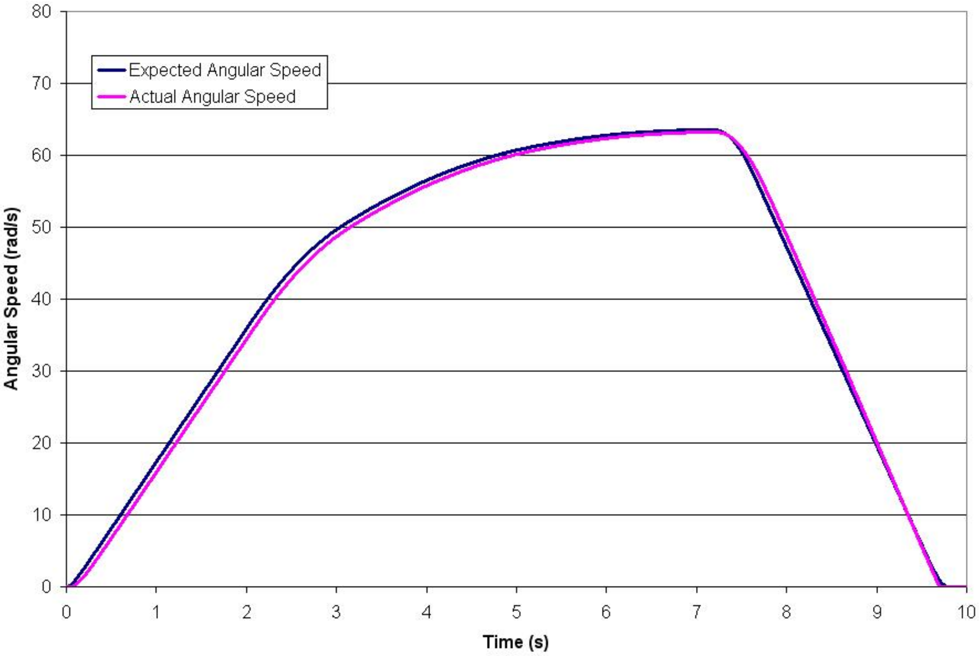

Figure 4.30: Comparison of the actual and expected angular velocity

Mechanical Friction Brake Comparison

The most distinguishable results can be seen when comparing the mechanical brake torques for both the Alternate I and Alternate II systems (Figures 4.22 and 4.31 respectively). Since the flow rates of the proportional control valves can be continuously varied, the mechanical braking torque is much smoother and tracks much more accurately in the Alternate II system when compared to the Alternate I (solenoid valve) system.

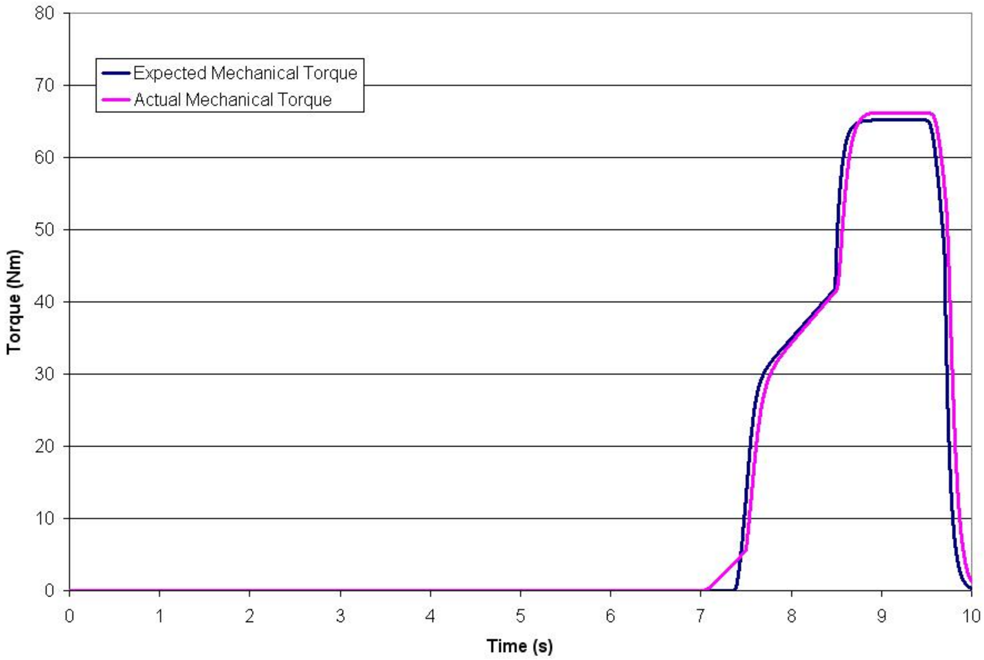

Figure 4.31: Results from brake booster attenuation test after Schmidt trigger and valve modifications - brake applied at t = 7s

Motor Torque and Regenerative Brake Comparison

Since there was no change made to the electric motor system between Alternate I and Alternate II, it was expected that the results found during the Alternate II test would be very similar to the results found in Figure 4.28 of the Alternate I system. The results from the Alternate II test are shown in Figure 4.32. As with the Alternate I concept, it is important to notice that the electric motor cannot produce enough regenerative braking torque to slow the flywheel as the driver expected. This results in the mechanical brake system supplementing the extra torque required which will waste some of the kinetic energy as heat instead of converting it into electrical energy to store in the ultracapacitor stack.

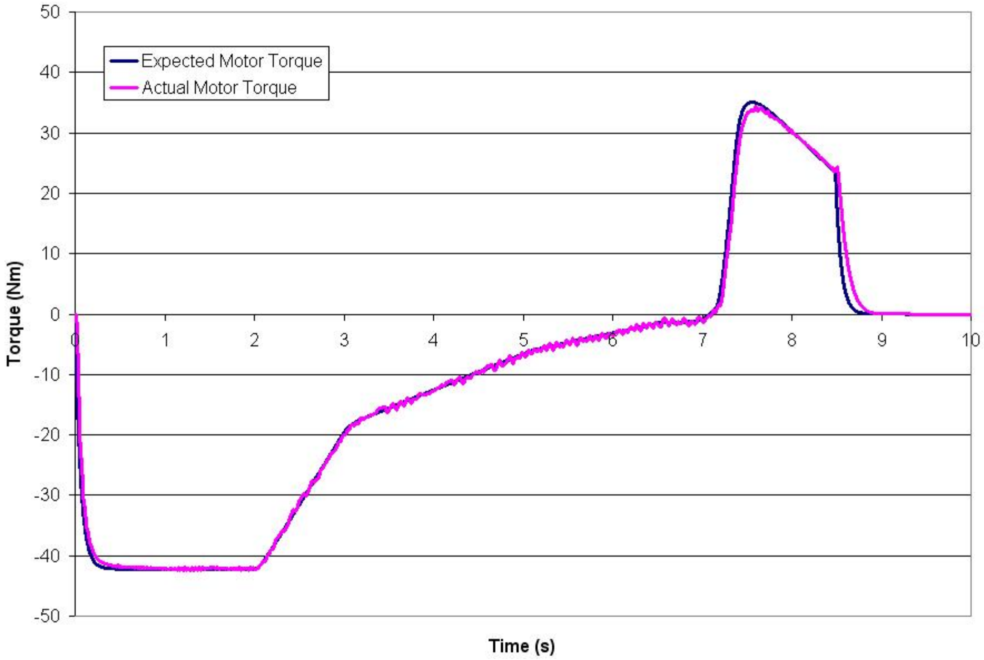

Figure 4.32: Comparison of the actual and expected electric motor torque - brake applied at t = 7s

4.3.5 Comparing the Alternate I and Alternate II Systems

In the previous few sections, simulation results as a whole were shown using both the Alternate I and Alternate II brake booster attenuation systems. The next step is to compare the systems with each other directly. The best way of doing this is by comparing how well each system can follow a requested mechanical braking torque. In Figures 4.33a and 4.33b, two common mechanical braking requests are shown with the corresponding Alternate I and Alternate II simulation response. It is clearly shown that the Alternate II system has a smaller steady state error when compared to the Alternate I curve. However, the greatest improvements are seen during the transients (from 5 to 8 seconds). The Alternate II system can smoothly follow the requested torque with little error, whereas the Alternate I system uses discrete steps to follow the requested curve which introduces greater error.

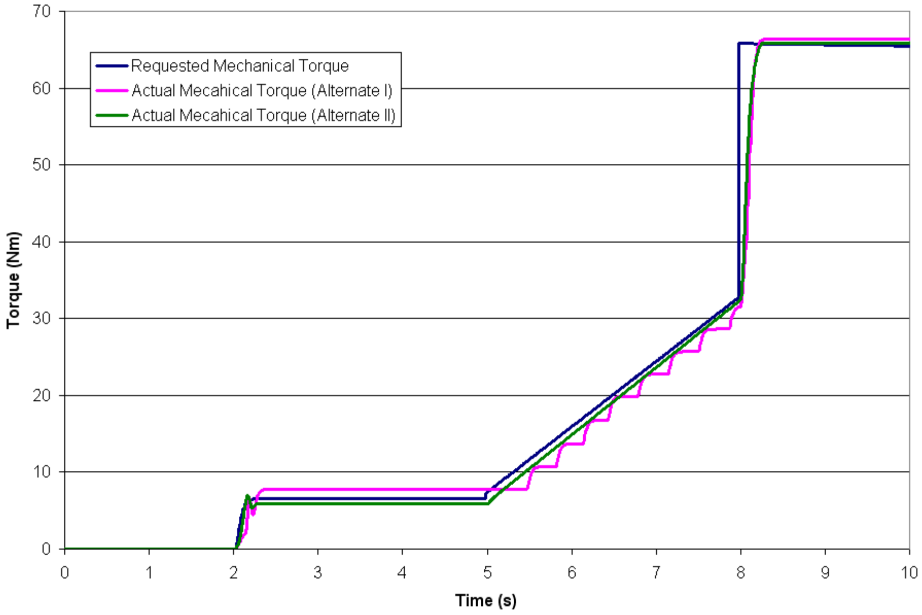

(a) Test 1

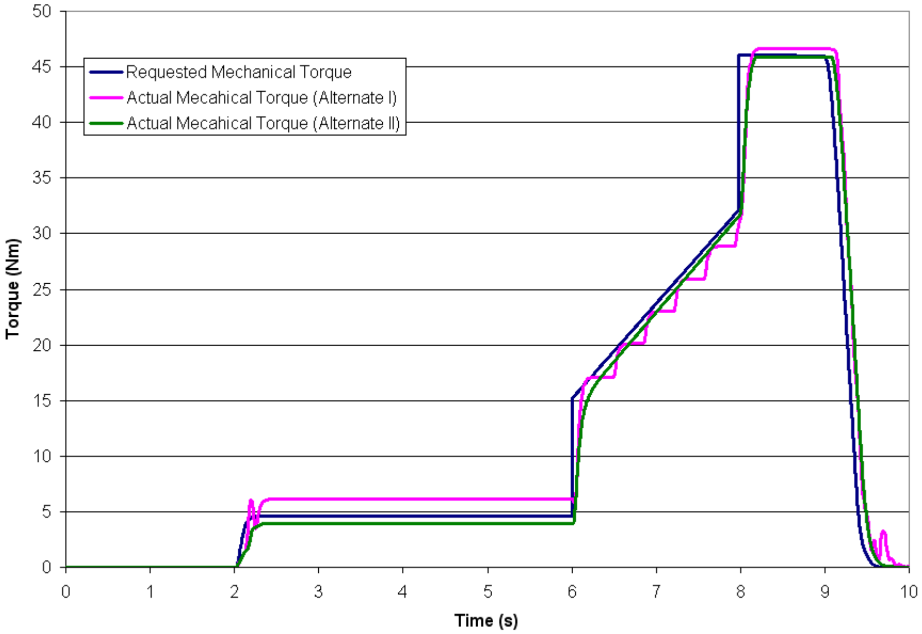

(b) Test 2

Figure 4.33: Comparison of the alternate I and alternate II systems

4.4 Physical Prototype

In 2004, Michael Kiers created a regenerative braking testbench while completing his master's thesis at the University of Waterloo [24]. This testbench has been redesigned to incorporate mechanical braking components to study the interaction between regenerative braking and mechanical braking and to test a new brake booster design and control algorithm that would increase regenerative braking efficiency. The power electronics has also been redesigned by Samy Ghania and an array of sensors has been added to the testbench by Simon Stark. An overview schematic of the testbench can be seen in Figure 4.34 and a detailed component description can be found in Appendix C.

4.4.1 Sensor and Data Acquisition System

To correlate the simulation results with the physical results of the testbench, a comprehensive sensor and data acquisition (DAQ) system was required to measure and record all important data. Part of the sensor system was also required for controlling different aspects of the regenerative braking process and to ensure safe operating conditions for the energy storage system. All sensors used have output voltages that range from 0 volts to 5 volts.

Throttle Position Sensor

To control the driving speed and torque of the induction motor, an accelerator pedal with a built in angular potentiometer has been selected (Figure 4.35a). Depending on the position of the accelerator pedal, a voltage from 0 volts to 5 volts is output from the potentiometer and used as an input for the vector control of the induction motor. This input serves as a torque demand for the motor.

Brake Pedal Force Sensor

The brake pedal force sensor consists of a load cell that has been incorporated in line where the driver's foot pushes on the brake (Figure 4.35b). This sensor is used to calculate the expected braking torque required by the driver during braking events. This expected

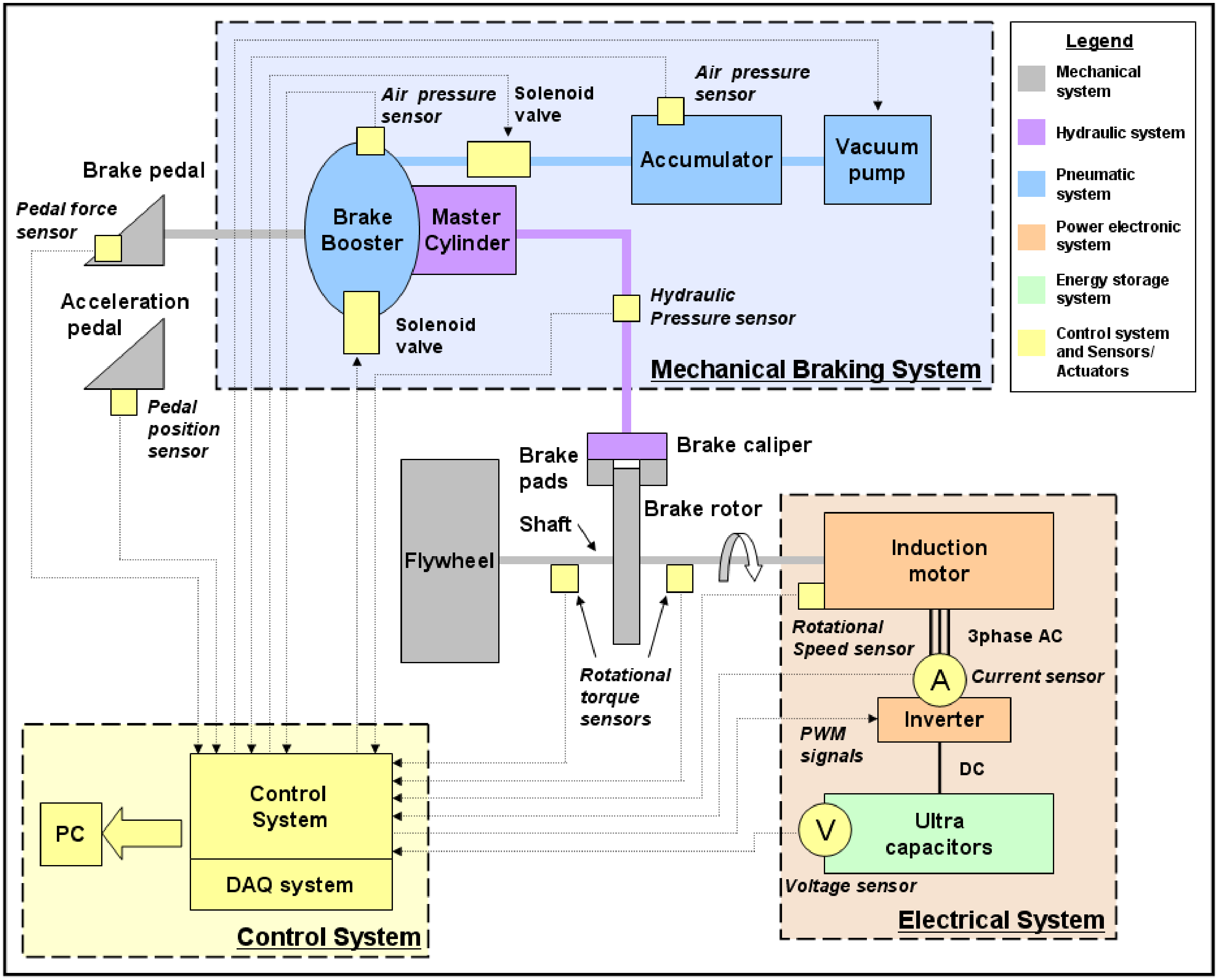

Figure 4.34: Testbench overview

braking torque is then split between regenerative braking and mechanical braking by the overall controller.

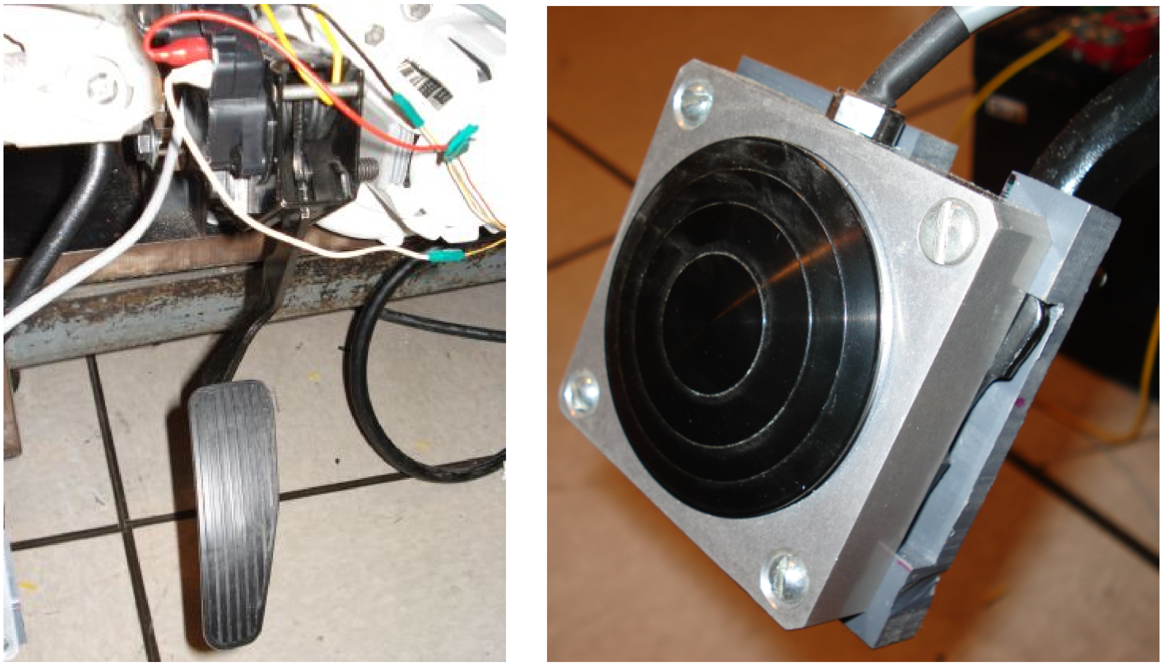

(a) Throttle position sensor

(b) Brake pedal force sensor

Figure 4.35: Testbench pedal sensors

Pressure Sensors

There are two air pressure sensors and one hydraulic pressure sensor used for the brake attenuation system, each relying on the piezoresistive effect for their operation (Figure 4.36). The hydraulic pressure sensor is used to correlate simulation data with the physical system and also used to control the amount of mechanical braking generated. A T fitting was used in the brake lines in order to implement the hydraulic pressure sensor. The first air pressure sensor is located in the constant pressure chamber of the brake booster and is used to control the vacuum. Vacuum is supplied by a vacuum pump and accumulator. The second air pressure sensor is located in the dynamic pressure chamber, and is not for control. It is used to compare the simulated brake booster dynamic chamber pressure with the physical system. For both air pressure sensors, a signal conditioning chip had to be made by the author in order to reduce the background noise and amplify the output voltage to range from 0 to 5V. The circuit diagram for the conditioning chip is shown in Figure 4.37.

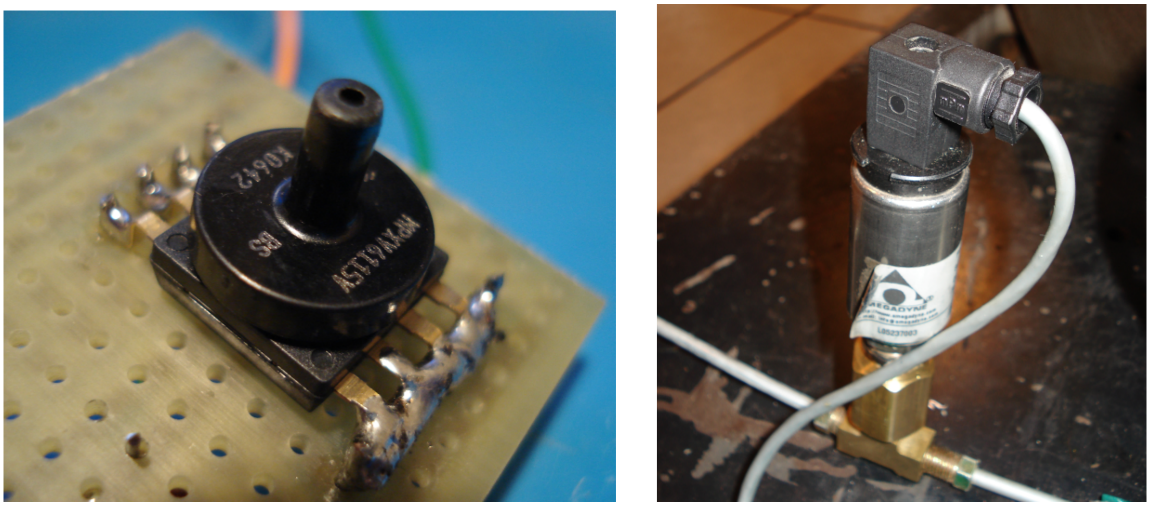

(a) Air pressure sensor (b) Hydraulic pressure sensor

Figure 4.36: Testbench pressure sensors

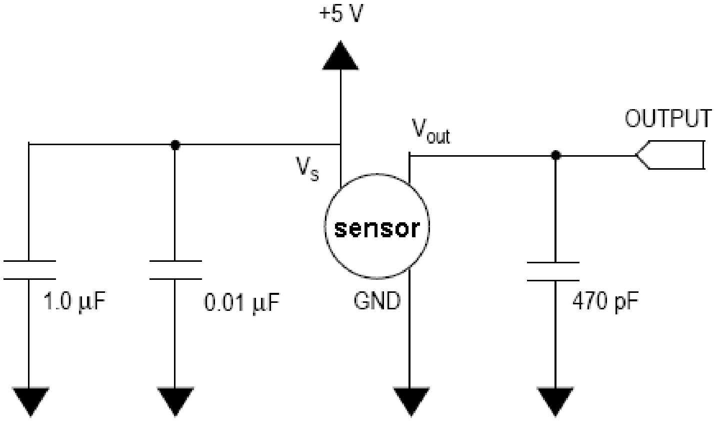

Figure 4.37: Conditioning chip circuit diagram

Torque Sensors

Torque sensors were required to measure the regenerative and mechanical braking torques to verify system performance. To accomplish this task, two 45 degree strain rosettes were installed with the middle strain gauge parallel to the shaft. One was installed between the electric motor and the mechanical brake (Figure 4.38a) and the other was installed between the mechanical brake and flywheel. By measuring the strain between the motor and the mechanical brake using the first strain rosette, the torque applied by the motor could be calculated. By measuring the strain between the mechanical brake and the flywheel using the second strain rosette, the total torque could be calculated. At that location, the cumulative strain from both the mechanical brake and motor torque could be measured. Since wires cannot be used from the strain gauges to our DAQ system because of the rotating shaft, a Microstrain Agile-Link 2.4 GHz Wireless Base Station with a V-Link Wireless Voltage node was used. The wireless node shown in Figure 4.38b was purchased with a half bridge configuration and was able to condition the signals from the strain rosettes and send them to the base station where the signals could be output into the DAQ system.

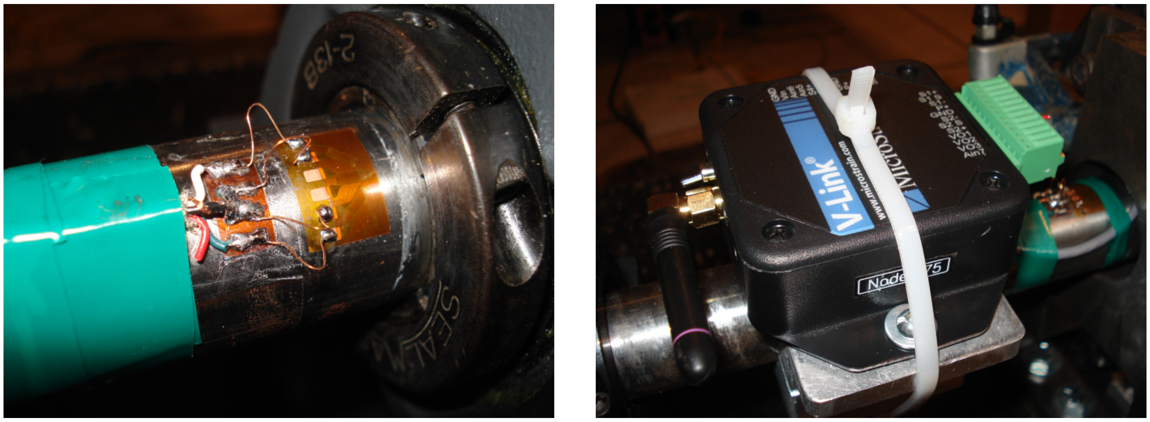

(a) Strain gage (b) Wireless node

Figure 4.38: Torque sensors

Current Sensors

Two current sensors are required to measure two of the three output AC phases from the inverter and then are fed back into the vector control algorithms to calculate the error as part of the electric motor controller. These sensors are current transformers and can measure the current using the induction effect (Figure 4.39a). The sensors can measure from 0 to 10 amps, which is higher than the 5.7 amp rated current of the motor.

Voltage Sensors

The voltage sensor is used to measure the state of charge of the ultracapacitor pack. It is used to determine when regenerative braking or driving of the motor can be allowed. If the voltage is too low, driving the motor will be stopped so that the ultracapacitors will not be discharged too much. If the voltage is too high regenerative braking will be prohibited so that the ultracapacitors will not overcharge.

Speed Sensor

The angular speed of the motor shaft is required as a feedback for the vector control of the induction motor. An optical encoder is used to precisely measure the transient speed of the motor during operation (Figure 4.39b). Optical encoders use a rotating encoder disk with transparent and non transparent fields positioned between a light emitting diode (LED) and a photo diode. This results in the photo diode receiving alternating ‘on’ and ‘off’ light signals that are transformed into an alternating voltage signal proportional to the speed of the motor shaft [56]. To convert the quadrature signal received from the optical encoder into an analog signal, a US Digital ETACH2 High Speed Encoder to Analog Tachometer was purchased.

Data Acquisition System

To log the sensor data, a Labjack U12 DAQ system shown in Figure 4.40 was used during testing. This unit was able to log data from eight different channels at once and also came with 5V power source outputs that were used for powering many of the sensors. The layout of the data acquisition system is shown in Figure 4.41. When using eight channels

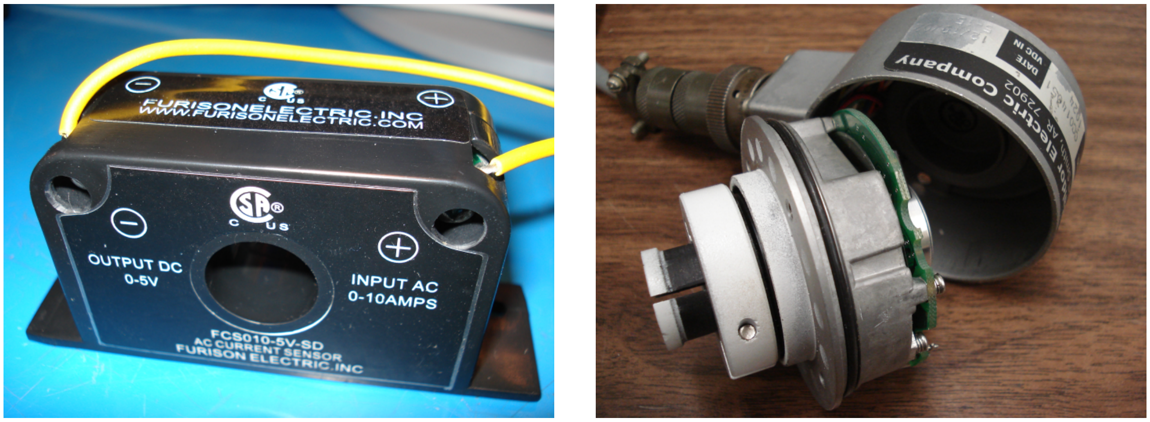

(a) Current sensor (b) Speed sensor

Figure 4.39: Testbench sensors

the Labjack had a maximum sampling rate of 2 Hz which was lower than the 10 Hz desired, but the price of the Labjack more than made up for the low sampling rate.

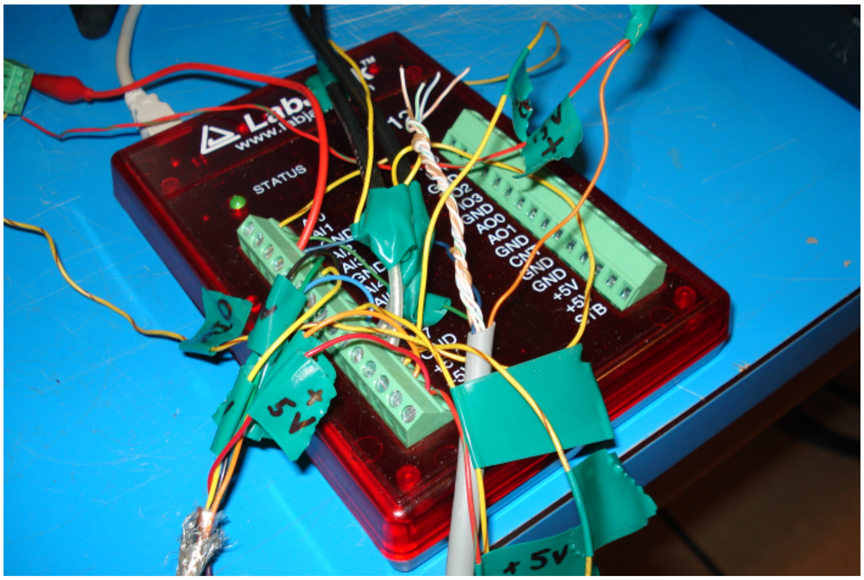

Figure 4.40: Data acquisition system

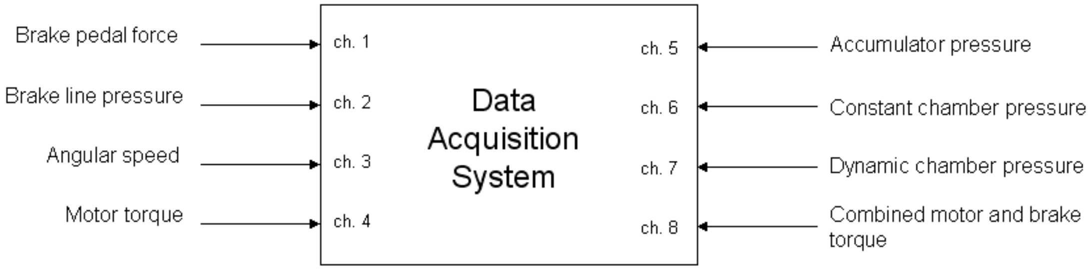

Figure 4.41: Layout of the data acquisition system

4.4.2 Control Systems

The three control systems were physically implemented using a personal computer (PC), a digital signal processor (DSP) and a National Instruments (NI) I/O device. The overall controller and the mechanical brake controller were both operated using the Real-Time Workshop built into Matlab 7.3.0 (R2006b) and the NI card. This allowed the PC to perform all the required calculations while the NI card allowed sensor signals to be input and requested torque signals to be physically output from the control systems. Since the inverter required switching frequencies of 1 kHz, a DSP was used to control the signals sent to the inverter. Algorithms created in Matlab were downloaded into the DSP's memory allowing it to function. The DSP was able to input requested motor torque and sensor signals from the NI card. An overview of the physical control system is shown in Figure 4.42.

The DSP used for the testbench was a Digital Spectrum eZDSP F2812. It was used to output the PWM signal to the inverter using the vector control described earlier in this chapter and feedback from the shaft speed encoder and current sensors. The DSP has 14 analog to digital converter (ADC) pins which would allow the sensor signals such as the throttle position sensor to be used to control the motor.

The I/O device used in the control system was a National Instruments PCI-2024E multifunction I/O device. This device contained 16 analog inputs, 2 analog outputs and 8 digital inputs/outputs which were used to monitor and control the distribution of braking

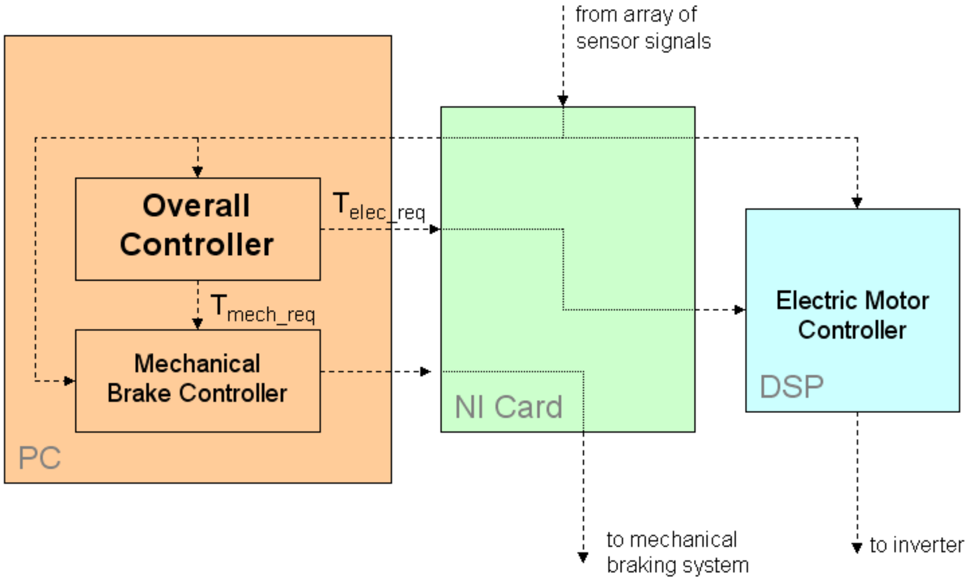

Figure 4.42: Physical control system overview

torque and the brake booster attenuation system. This system used feedback from all the sensors mentioned above and used outputs that control both solenoid valves, the vacuum pump and the electric motor requested torque.

4.4.3 Electrical System

The main function of the electrical system was to drive the flywheel up to the rated speed of the motor and then use that kinetic energy stored in the flywheel to recharge the ESS during braking. To accomplish this task, three major components were required. They are the induction motor, the inverter and the ultracapacitor stack.

Induction Motor

The electric motor used to accelerate the flywheel during driving mode and act as a generator during braking mode was a Baldor ZDWNM3609T three-phase AC induction motor. It has a power rating of 2 hp or 1.49 KW at 460 V and 60 Hz. The full load current of the motor is 5.8 A and the rated motor speed is 1725 rpm [7]. The electric motor was mounted securely to the mechanical testbench described below using four 5/16-18 x 1-1/4 A307A Hot Dipped Galvanized Hex Bolts [8].

Inverter Module

The inverter used for the induction motor is a Powerex PS21965-4 Dual-In-Line Intelligent Power Module. It is rated for 20 A and 600 V. This module is IGBT-based and is equipped with under-voltage, over-current and over-temperature protection. An application circuit was designed and built for this module by Bluestar Engineering [13] to filter and condition the PWM signal received from the DSP. This circuit also enabled the voltage, current and temperature sensors to function properly and allowed easy connection for the PWM signals, the bus voltage and the three phase alternating current used to drive the motor. Figure 4.43 shows the application circuit drawing along with the completed inverter module.

Ultracapacitor Stack

The energy storage system used to power the motor during acceleration and store electric energy during regenerative braking consisted of 154 Maxwell BCAP0008 ultracapacitor cells arranged in series. The ultracapacitor stack is shown in Figure 4.44. Each cell has a capacitance (C) of 1800 F and a maximum voltage of 2.5 V [32]. When connected in series, the ultracapacitor stack had a capacitance of 11.7 F and a maximum voltage (V_{max}) of 385 V with a maximum allowable drop in voltage of $\frac{V_{max}}{2}$ to not undercharge the ultracapacitor stack. Using Equation 4.16 this translates into a system that can discharge 650.3 kJ of electrical energy when used between V_{max} and $\frac{V_{max}}{2}$. Balancing boards were also connected between each cell to protect the ultracapacitor from over-voltage during rated system use and were capable of providing up to 300 mA of current to reduce over-voltage when required [32].

$$E = \frac{1}{2}C\left(V_{max}^2 - \left(\frac{V_{max}}{2}\right)^2\right) \tag{4.16}$$

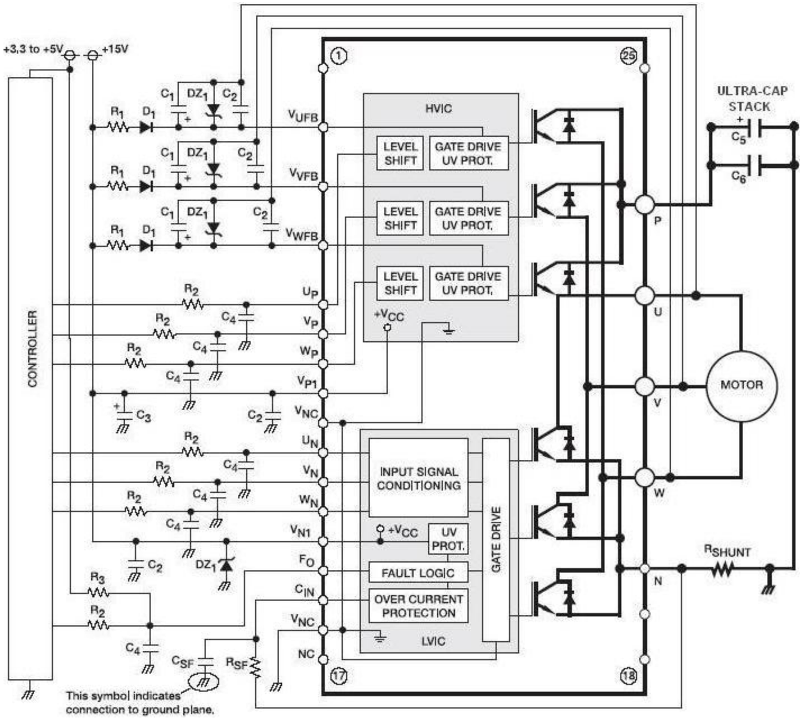

(a) Application circuit drawing

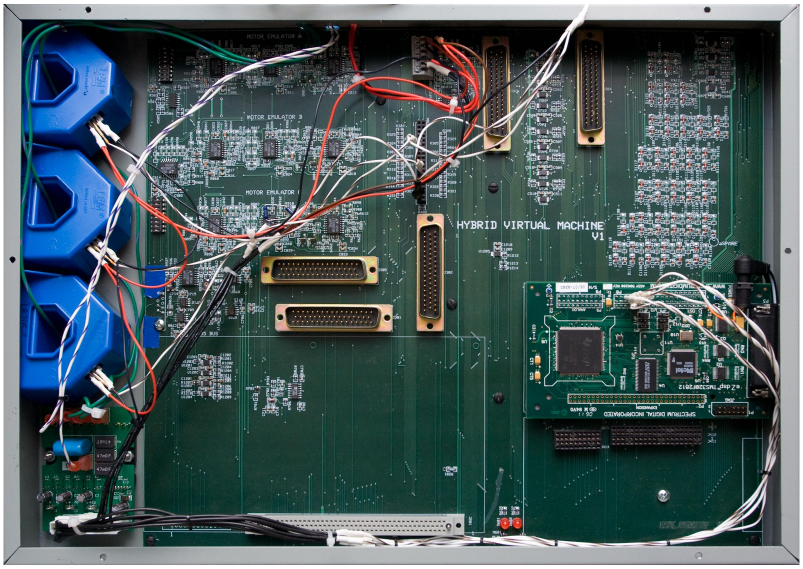

(b) Inverter module

Figure 4.43: Inverter setup

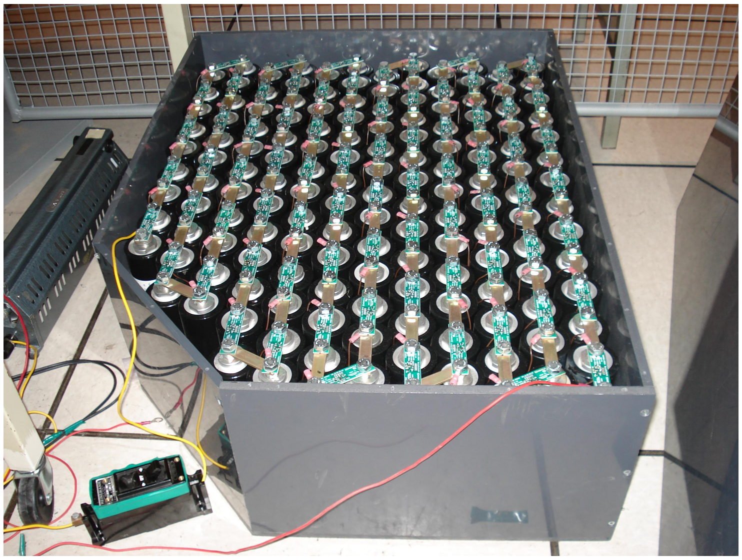

Figure 4.44: Ultracapacitor stack

Vacuum Pump

In conventional spark ignition vehicles, the pressure drop in the intake manifold is used to create the vacuum in the constant pressure chamber of the brake booster. To simulate this vacuum, a 12V Hella UP28 rotary vane compressor vacuum pump and 4 litre accumulator were incorporated into the testbench. This pump was chosen because of its lightweight design and it could easily be implemented into the E03 RGB project vehicle if required. A Schmidt trigger was used to control the vacuum pump to maintain the accumulator pressure between 40 kPa and 50 kPa, which corresponds with pressures typically found in automotive applications (Figure 4.45). One of the air pressure sensors mentioned above was used as a feedback for the vacuum pump control.

4.4.4 Mechanical System

The physical mechanical system consisted of a mechanical bench with a flywheel attached to a shaft and coupled with an induction motor. The shaft was supported by bearings, and a mechanical disc brake was attached between the flywheel and induction motor. There was

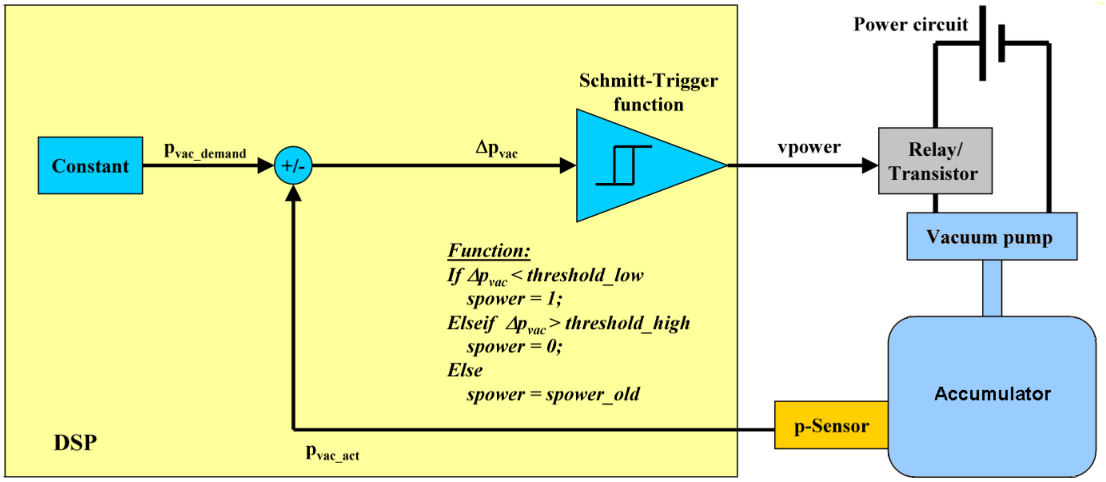

Figure 4.45: Vacuum pump control [49]

a brake pedal attached to one corner of the bench with the corresponding brake booster and master cylinder. A computer aided design (CAD) drawing of the initial mechanical system configuration is shown in Figure 4.46. It is important to realize that when manufacturing the testbench most standard mechanical components use imperial units. For this reason imperial units have been used in calculations related to the mechanical braking system.

Mechanical Bench and Flywheel

The existing mechanical bench and flywheel shown in Figure 4.47 were used from the 2004 experiment. The flywheel was designed to simulate the scaled down kinetic energy of a Plymouth Voyager [24]. Kiers [24] chose the ratio of the peak engine power from the Voyager to the peak power of the induction motor to calculate the scaling factor.

$$ScalingFactor = \frac{peak\ electric\ motor\ power}{peak\ engine\ power} = \frac{1.5kW}{134kW} \tag{4.17}$$

The next step was to relate the velocity (v) of the Plymouth Voyager with the rotational velocity (ω) of the flywheel. Kiers used the driven wheel rotational velocity from the

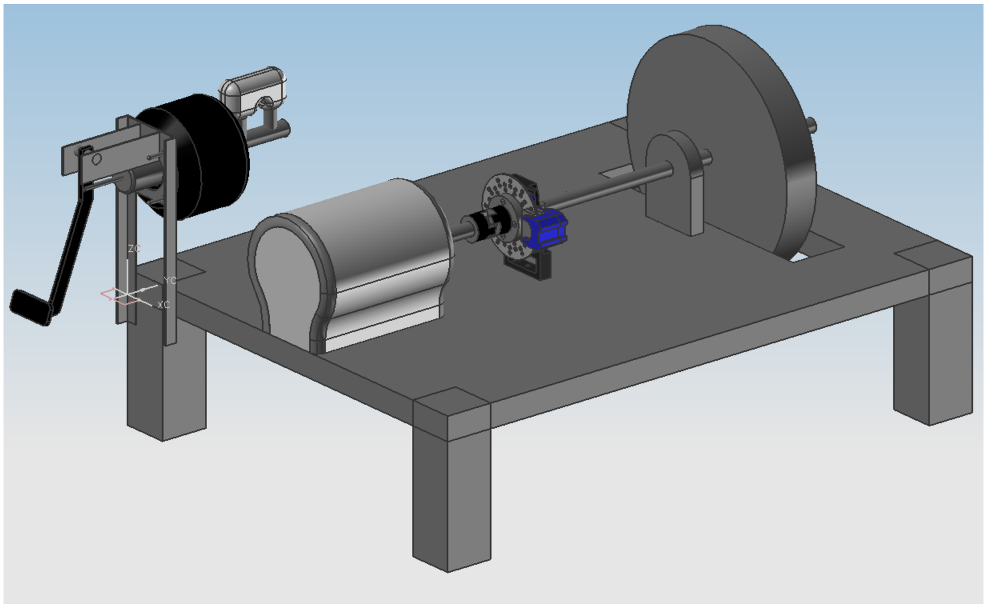

Figure 4.46: Initial testbench configuration

Voyager and set that equal to the flywheel speed. This resulted in a vehicle speed of 120 km/h to correlate with a rotational velocity of 101 rad/s of the flywheel [24].

The final requirement was to calculate the dimensions and inertia of the flywheel. To do this, the kinetic energy of both the vehicle and the flywheel were equated using the scaling factor and correlated velocity/rotational velocity values.

$$
\begin{aligned}
E &= \frac{1}{2}mv^2 \\
E &= \frac{1}{2}J\omega^2
\end{aligned}
\tag{4.18}
$$

From these equations the required polar moment of inertia (J) was calculated to be 20.206 lb·in·s^2 (2.283 kg·m^2) [24]. The size of the flywheel was then determined assuming

Figure 4.47: Original configuration of the testbench

the use of a disk shaped flywheel and using Equation 4.19.

$$J = \frac{1}{2}\rho\pi r^2 t \tag{4.19}$$

Steel was chosen for the flywheel material and the final flywheel dimensions were chosen to optimize the weight and size of the flywheel (Table 4.5).

Once the flywheel was sized, a mechanical bench was designed to support the weight and vibration of the flywheel and induction motor. A 1 inch steel slab, 2 feet wide by 3 feet long, was used for the base. Two reinforcing steel square tubes were welded to the

Variable	**Value**
Radius (r)	9 inches
Thickness (t)	2.7 inches
Weight (w)	193 lbs
Density (ρ)	0.283 lb/in^3

Table 4.5: Properties of the flywheel [24]

base on each side and 2 inch square steel bars (1/8 inch thick by 6 inch tall) were used for the corner legs [24].

Mechanical Braking System

The braking system incorporated components from many different applications to try and brake the flywheel as realistically as possible. The brake pedal, brake booster, master cylinder and valve body were from a 2002 Chevrolet Cavalier and were mounted on an adjustable bracket attached to the testbench. The bracket allowed the brake pedal to be raised and lowered for operator comfort. Since only one brake is required to brake the flywheel, three ports from the valve body were blocked, allowing a standard stainless steel 3/16 inch brake line to be attached to the remaining open port and run to the brake caliper.

To scale down the braking system to the same size as the flywheel, a design process was conducted that used a simple sum of moments about the flywheel to size the brake rotor. Under good road conditions it is estimated that the Chrysler Pacifica can brake from 120 km/h to 0 km/h in four seconds with a master cylinder pressure of 800 psi applied by the driver. It has been shown above that the vehicle speed of 120 km/h correlates with a flywheel angular speed of 101 rad/s. To scale down the brake caliper it was decided that a Yamaha Warrior single piston brake caliper would be used with an estimated brake pad friction coefficient. Knowing the information above, along with the data in Table 4.6, it was possible to solve for the radius of the brake rotor. Equation 4.20 shows how the radius was calculated.

Variable	**Value**
Braking time (t)	4 seconds
Area of the caliper piston ($A_{caliper}$)	0.695 in^2
brake pad friction coefficient (μ)	0.4
Polar moment of inertia of the flywheel and shaft (J)	21 lb·in·s^2
Change of angular velocity ($\Delta\omega$)	101 rad/s
Master cylinder pressure (P_{mc})	800 psi

Table 4.6: Properties of the mechanical brake system

$$\sum M = J\alpha$$

$$\mu_{pad} A_{caliper} r_{caliper} P_{mc} = J\,\frac{\Delta\omega}{\Delta t} \tag{4.20}$$

$$r_{caliper} = J\,\frac{\Delta\omega}{\Delta t} \mu_{pad} A_{caliper} P_{mc}$$

Solving for Equation 4.20 gives a brake rotor radius of 2.38 inches. With further investigation a 310 stainless steel brake rotor with a radius of 2.5 inches was acquired from the mini baja team and was deemed acceptable to use for the testbench.

Once the brake caliper was selected, an upright was designed and machined out of cold rolled 1018 steel to support and locate the brake caliper and withstand any torques that may be applied to the caliper during braking events. Figure 4.48 shows a CAD rendition of the mechanical brake system on the testbench with the first bearing removed to allow visualization of the brake. Manufacturing drawings of the mechanical brake system are shown in Appendix B.

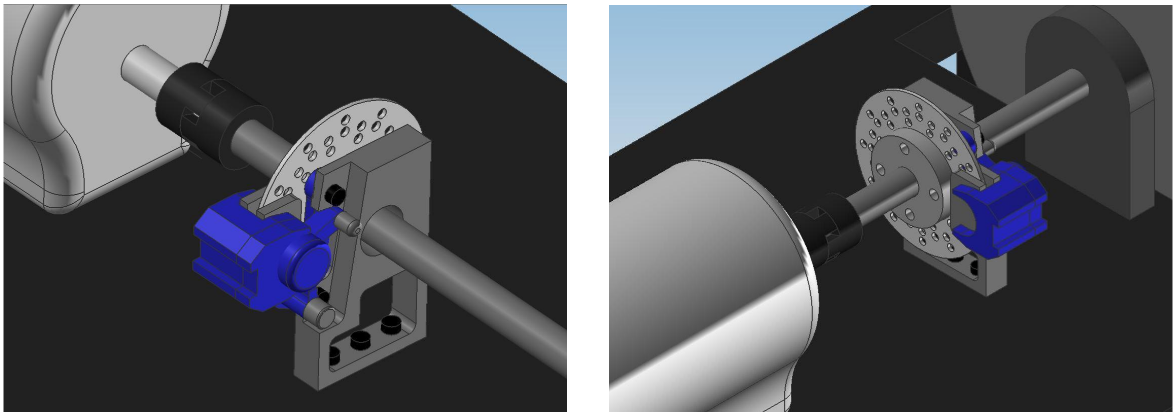

(a) Rear view (b) Front view

Figure 4.48: Mechanical brake arrangement

Shaft and Connections

To attach the flywheel, braking system and electric motor a 1 1/8 inch 1045 turned ground and polished steel shaft was selected. The shaft material has a yield strength of 85 ksi [23] and should be able to handle all applied loads and torques for the testbench. The flywheel and brake hub were attached to the shaft using 1/4 inch 1018 cold rolled parallel keys that are 2.7 and 1 inch long respectively. All keyways were machined into the shaft as double-ended, end-milled keyway and were 1/8 inch deep. Stresses in the keyway and shaft were calculated using basic machine design techniques and stress concentration factors [37].

Stresses in Key

$$\tau_{xy} = \frac{F}{A_{shear}}$$
$$\sigma_x = \frac{F}{A_{bearing}} \tag{4.21}$$

Where the applied force (F) can be found from the quotient of the shaft torque (T) and the shaft radius (r). The shear area of the key (A_{shear}) which in this case is the product of the key's width and length and $A_{bearing}$ is the area of contact between the key side and the shaft or the hub. For a square key it will be the product of the length and half the height.

Assuming a maximum shaft torque of 1800 in·lb (approximately 200 N·m) the stresses in the brake rotor key can be calculated using Table 4.7 and compared to the Von Mises failure criteria (Equation 4.22). If the yield strength of the material (which is 85 ksi) is larger than the Von Mises stress, then no plastic deformation will occur [47]. It was found that the maximum Von Mises stress in the key would be 33.9 ksi resulting in a safety factor of 2.5 (Equation 4.23).

$$\sigma_{VM} = \frac{1}{\sqrt{2}}\sqrt{(\sigma_x - \sigma_y)^2 + (\sigma_y - \sigma_z)^2 + (\sigma_z - \sigma_x)^2 + 6(\tau_{xy}^2 + \tau_{yz}^2 + \tau_{zx}^2)} \tag{4.22}$$

$$FS = \frac{\sigma_{yield}}{\sigma_{VM}} \tag{4.23}$$

Stresses in Shaft

$$\begin{gathered} \tau_{xy} = K_{ts}\frac{Tr}{J} \\ \sigma_x = K_t\frac{Mc}{I} \end{gathered} \tag{4.24}$$

Where K_{ts} and K_t are the torsion and bending stress concentrations respectively created by the presence of the keyway, M is the bending moment created by the flywheel, c is the distance from the neutral axis to the outer fiber of the shaft and I is the area moment of inertia of the shaft.

Assuming the same maximum shaft torque as above, the Von Mises stress in the shaft was calculated to be 33.8 ksi resulting in a safety factor of 2.5 for the shaft.

Variable	**Value**
Radius (r)	9/16 in
Polar moment of inertia (J)	0.157 in^4
Distance from N.A. to outer fiber (c)	9/16 in
Area moment of inertia (I)	0.079 in^4
Bending moment (M)	217.125 in·lb
Stress concentration for torsion (K_{ts})	3
Stress concentration for bending (K_t)	2.3
Yield strength of the shaft(σ_{yield})	85 ksi

Table 4.7: Properties of the shaft and stress concentrations

Lastly, the shaft and flywheel were supported by three Seal Master NP-18T pillow block bearings rated for 543 lbs. at a speed of 1750 rpm [46] and a three-jaw spider shaft coupling was used to couple the shaft to the motor and allow for slight misalignments.

4.4.5 Brake Booster Attenuation System (Alternate I)

It was decided that the first brake booster attenuation system would use Alternate I. To allow for the pressure in the constant pressure chamber of the brake booster to be modified independently of the brake pedal force, two direct-acting, two-way, normally-closed solenoid valves were used outside of the brake booster. One solenoid valve will connect the constant pressure chamber to the dynamic pressure chamber and when activated will momentarily equalize the pressure between the two chambers which in turn will open the air valve and vacuum valve of the brake booster and allow atmospheric air to enter the constant pressure chamber. This will decrease the pressure differential between the two chambers and reduce the boost created by the brake booster. The other solenoid valve will connect the constant pressure chamber of the brake booster with an accumulator that will be held between 30 kPa and 40 kPa absolute pressure. When this valve is activated, it will draw air from the constant pressure chamber which will lower the pressure in the chamber and increase the boost created by the brake booster. (Figure 4.49).

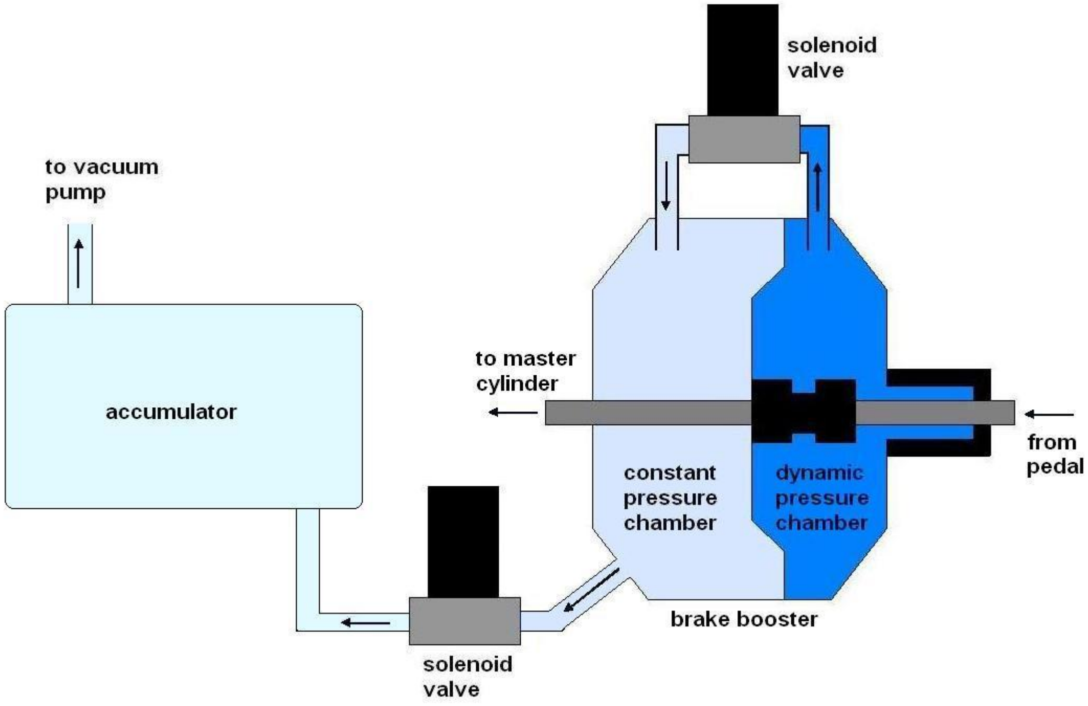

Figure 4.49: Brake booster attenuation concept

A solenoid valve is an electro-mechanical valve for use with liquid or gas that is controlled by applying or stopping an electrical current through a solenoid. A solenoid is a coil of wire which produces a magnetic field when an electrical current is passed through it [5].

There are many different types of solenoid valves. There are 2-way valves that have one inlet and one outlet and there are also 3, 4 and 5 way valves that have a combination of either multiple inlets, outlets or both [40]. For this application, a 2-way valve was chosen because there is only one inlet and one outlet required.

Solenoid valves can either be normally open (NO) or normally closed (NC). A normally closed valve is forced closed by a spring and is electrically activated to be open. The normally closed valves were used for the brake booster attenuation system, because under most conditions the valve will be closed and hence energy will be saved.

There are also two major types of operating mechanisms for solenoid valves. The first is the direct acting valve in which the magnetic plunger is acting directly on the valve to open or close the valve orifice. The pressure and flow of this type of valve depends directly on the orifice size and the coil power [51]. The second is referred to as a pilot operated valve. This type of valve is equipped with a diaphragm in which there is one bleed orifice and one pilot orifice. The plunger is acting on the pilot orifice allowing it to open or close. If this orifice is opened, pressure is released from the pilot chamber resulting in overpressure in the bottom of the diaphragm which is lifted by the line pressure opening the main orifice. When the pilot orifice is closed, full line pressure is applied in the pilot chamber through the bleed orifice which creates a seating force for the diaphragm closing the main orifice. For both of these types of valves, the plunger is usually connected to a spring which forces the plunger and in turn the valve to seal [51].

For the brake booster attenuation system, a direct acting valve was chosen because a pressure differential is not required for the valve to operate. Figure 4.50 shows the basic principles and operation of a direct-acting, 2-way, normally-closed solenoid valve.

When selecting the solenoid valves for this application, there were many other considerations that needed to be addressed. The first was specifying what type of coil to use for the valves. Since the valves will be used for an automotive application, it was decided that a 12V DC coil would be the easiest to implement into the Pacifica project. The next parameters that were examined were the flow characteristics and the response times of the valves. It was known that the larger the flow factor of the valve, the faster the pressure in the constant pressure chamber could be changed. However, as the flow factors increase, so does the size of the valves, causing the response times of the valves to also increase creating lag in the system. The flow of a solenoid valve is the quantity of

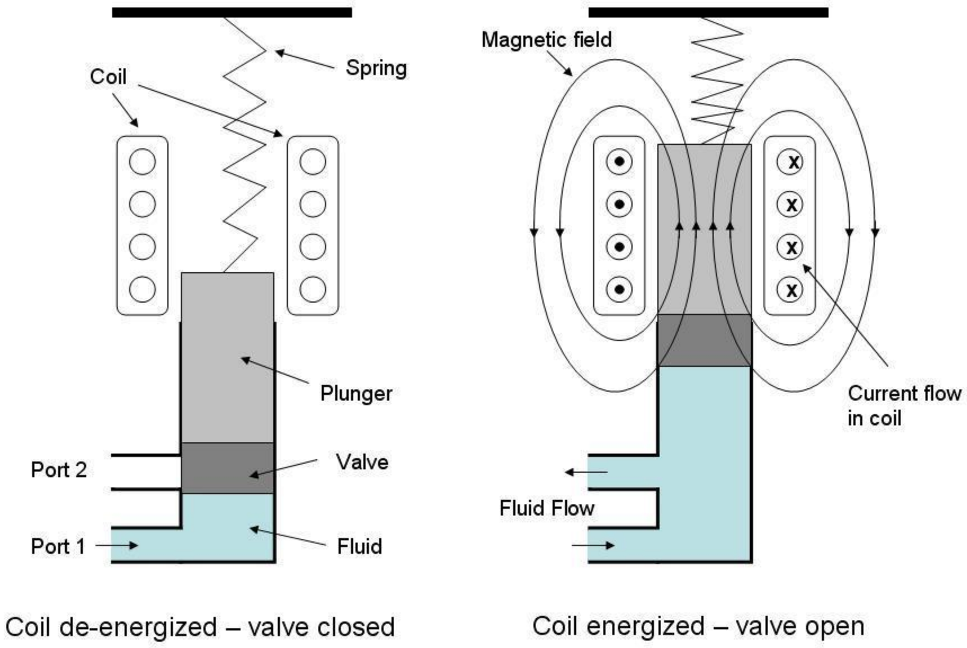

Figure 4.50: Operation of a direct-acting, two-way, normally-closed solenoid valve

fluid per unit time flowing through the valve. In order to use a simple formula to calculate and compare the different types of valves, all variables pertaining to the calculation of flow have been reduced to a common variable: the flow coefficient C$_v$. This factor depends on the design of the valve and the outlet tube size. Knowing the flow factor supplied by the manufacturer the flow rate, Q in l/min can be found using Equation 4.25 [51].

$$Q = \begin{cases} N_2 C_v P_1 \left(1 - \frac{2\Delta P}{3P_1}\right) \sqrt{\frac{\Delta P}{P_1 \cdot SG_{gas} \cdot T_1}} & P_2 > \frac{1}{2}P_1 \\ \\ 0.471\ N_2 C_v P_1 \sqrt{\frac{1}{SG_{gas} \cdot T_1}} & P_2 < \frac{1}{2}P_1 \end{cases} \tag{4.25}$$

Where P_1 and P_2 are the upstream and downstream pressures across the valve respectively, and $\Delta\ P$ is the difference between those two pressures in bars. The gas specific gravity is denoted by SG_{gas} and T_1 represents the upstream temperature in Kelvin. The constant, N_2, was used to convert the flow to l/min when measuring pressure in bars and temperature in Kelvin ($N_2 = 6950$) [9].

From the simulations created in the section on the virtual prototype, it was found that a solenoid valve with a flow rate greater than 5 l/s would be acceptable. The flow factor that corresponds with this value is $\mathrm{C}_v = 1.7$ for an average pressure drop value of 0.3 bar where the upstream pressure is 1 bar and the temperature is 298 K.

Also from the simulations, it was determined that the response times for the valves opening and closing should be less than 50 ms to ensure the pressure changing lag is within acceptable values. Figure 4.51 shows the results of the simulations conducted where the response time and flow factor were varied to determine appropriate values.

Once the criteria for selecting the solenoid valves was determined, the next step was to source a valve that would meet the demanding requirements. After a long search, a solenoid valve from SMC Pneumatics Limited was selected for the system. This direct-operated, 2-way, VCA series valve had a 12V DC coil, could withstand low vacuum conditions, had a flow factor of 1.9 and could cycle at 10 Hz.

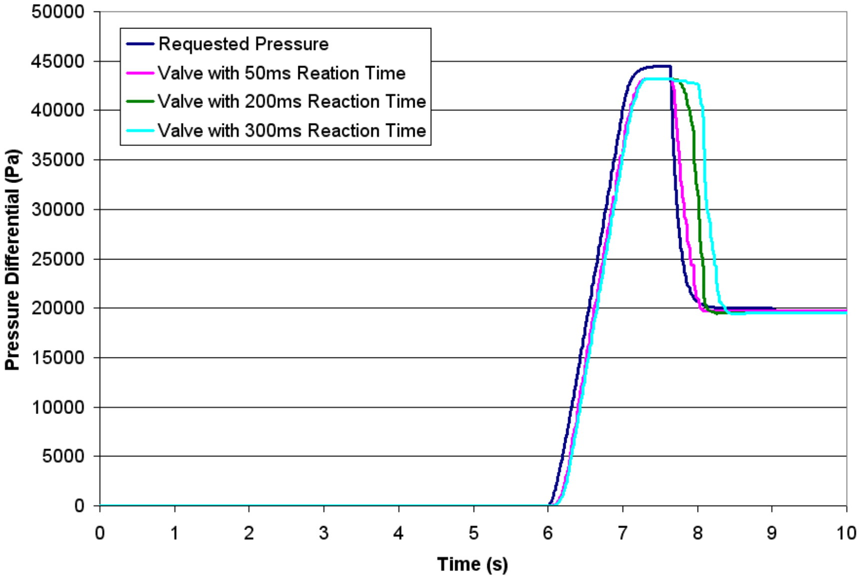

(a) Variation in valve reaction time

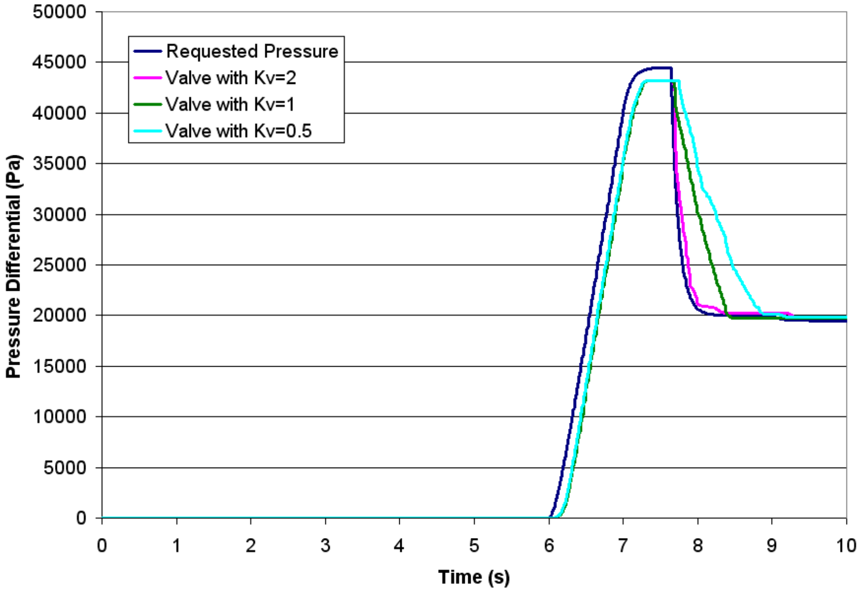

(b) Variation in valve flow rate

Figure 4.51: Comparing properties of different solenoid valves

4.5 Physical System Results

The mechanical braking system and sensor setup were completed before the power electronics were operational. This led to the issue that the first mechanical braking and brake booster attenuation tests had to be completed without the use of the electric motor. Since the electric motor could not be used to turn the flywheel it was also not possible to measure the torque generated by the mechanical braking system. To overcome this issue, the brake line pressure of the system was used to correlate the actual mechanical braking system with the simulation results.

4.5.1 Standard Brake System Functionality

Upon the completion of the mechanical testbench, preliminary braking tests were conducted to ensure the braking system was functioning properly. During these tests the brake booster attenuation system was not activated and the system functioned as a standard automotive braking system. The first test conducted was used to ensure the brake booster was not damaged during the installation of the brake booster attenuation system. During this test an increasing brake force was applied to the brake pedal which is expected to cause an increasing pressure differential between the two chambers of the brake booster. The results from this test are shown in Figure 4.52a. As the pedal force increases, the pressure differential increases to a maximum differential which occurs when the pressure in the dynamic pressure chamber reaches 1 atmosphere. These results show that the brake booster was operating correctly.

The second test conducted on the mechanical brake system was to ensure that the force from the brake booster was transmitted to the master cylinder and creating hydraulic brake line pressure. As in the previous test, an increasing brake pedal force was applied with an expected increase in brake line pressure. Figure 4.52b demonstrates that the mechanical brake system does function as expected.

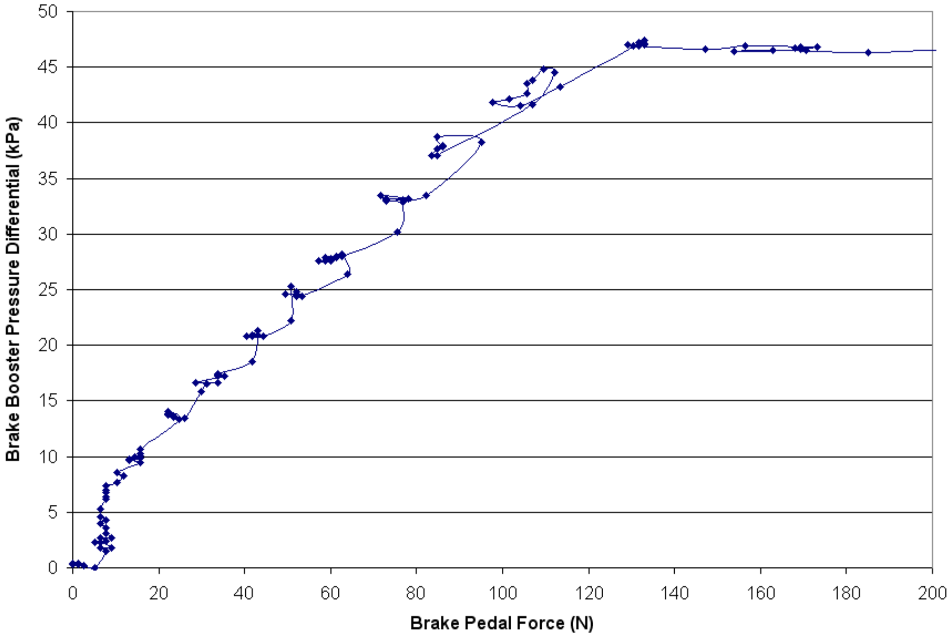

(a) Initial test demonstrating brake booster functionality

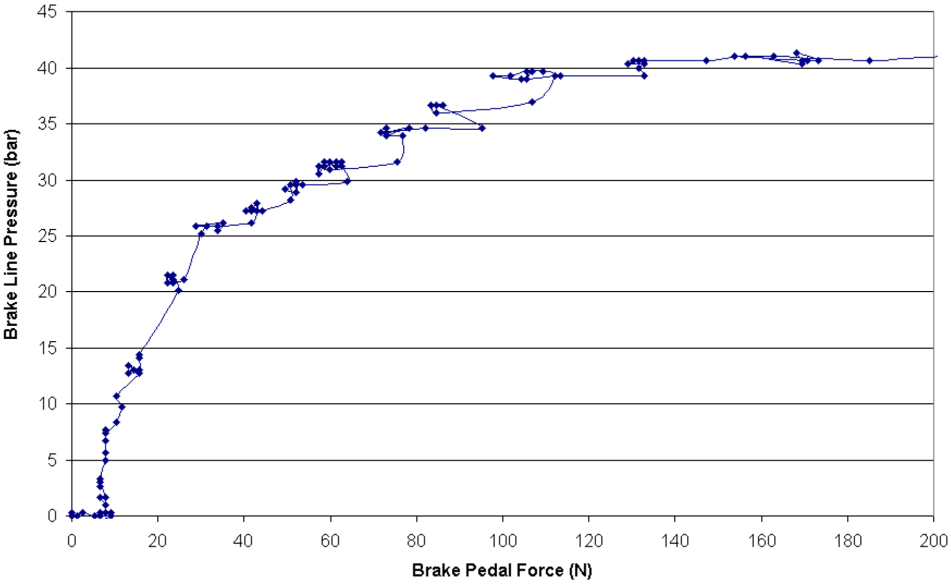

(b) Initial test demonstrating brake system functionality

Figure 4.52: Initial brake functionality tests

4.5.2 Brake Booster Attenuation (Alternate I) System Functionality

Once the brake system was operational, the next step was to test the brake booster attenuation (Alternate 1) system. The initial tests were used to demonstrate that the system could decrease and increase the brake line pressure independent of the brake pedal force. A test was completed that used the brake line pressure from a brake pedal input and reduced the brake line pressure in steps, followed by increasing the brake line pressure back to the initial pressure level. The results from this are shown in Figure 4.53.

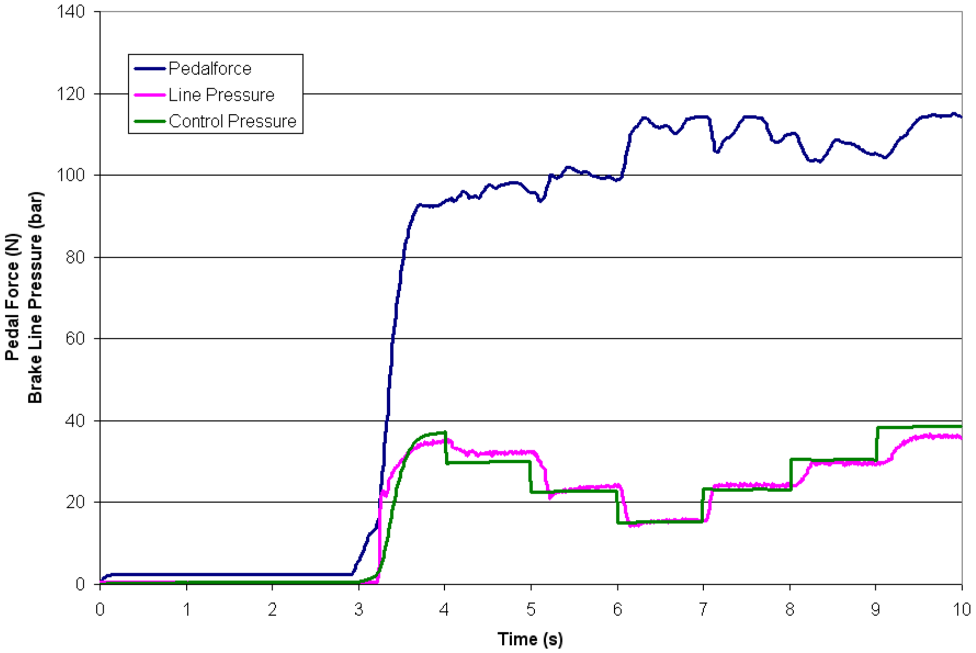

Figure 4.53: Initial test demonstrating brake booster attenuation system feasibility

Once the brake booster attenuation system was functional, the next characteristic to test was the reaction time of the system and the ability of the system to attenuate mechanical braking torque to zero. The results from this test are shown in Figure 4.54. To do this test, the brake pedal was applied with no initial boost after 1 second. The valve to the accumulator (valve 1) was then fully opened at 4 seconds resulting in full boost being applied. After the maximum pressure was reached, valve 2 was opened at 7 seconds causing the boost to drop to zero. From the figure, the time response of the system from zero boost to full boost and from full boost to zero boost was approximately 0.4 seconds which was less than the 0.6 second requirement, thus demonstrating the feasibility of the system. However the system was not able to completely drop the brake line pressure to zero because some of the pedal force was still transferred through the brake booster to the master cylinder. Since the system was able to drop the brake line pressure below 10 percent of the full value, this was deemed acceptable for the functionality of the system.

During the last two tests the physical feel of the brake pedal was being evaluated. It was found that during the first test the driver was unaware of the brake booster attenuation system functioning. However, during the second test the driver could feel the brake pedal become more firm during the full attenuation phase of the test. It was decided that the firm feel felt by the driver was very subtle and thus acceptable.

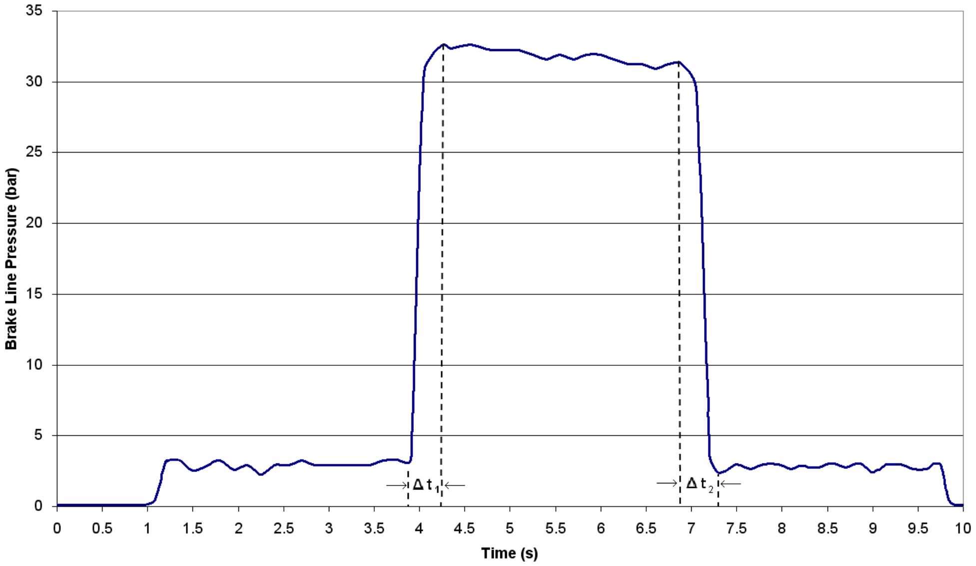

Figure 4.54: Response time and attenuation range of the system

4.6 Results using the Virtual and Physical Prototypes

One of the more valuable outcomes of creating both virtual and physical prototypes is the ability to validate simulation results with physical findings. This was an important step which corroborated the testing results completed using the virtual prototype.

4.6.1 Standard Brake System Comparison

Two tests were carried out to see how well the simulation modelled the actual physical system without using the brake booster attenuation system. The first test was to compare the pressure in the dynamic chamber of the brake booster versus pedal force and the second test was to compare the brake line pressure versus pedal force. Both tests were conducted without using the brake booster attenuation system. The results from these tests can be seen in Figures 4.55 and 4.56.

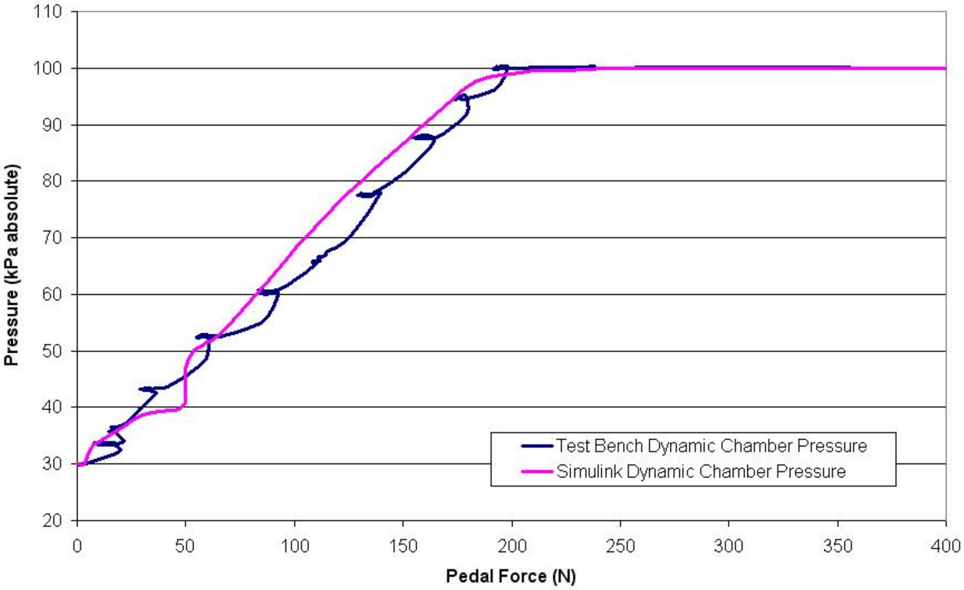

Figure 4.55: Comparison of the actual and simulation dynamic chamber pressure

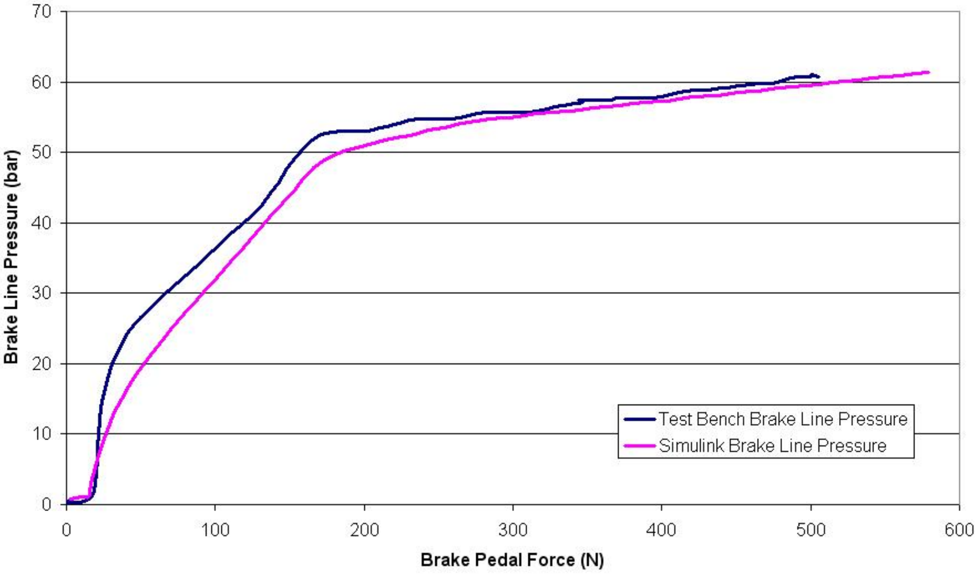

Figure 4.56: Comparison of the actual and simulation brake line pressure

From the figures, it was shown that the Simulink simulation results correlated very well with the actual standard mechanical braking system test results taken from the testbench. For both tests, the simulated and actual pressures had small errors which would result in minor inaccuracies.

4.6.2 Solenoid Valve Comparison

Earlier in this chapter, simulations of the solenoid valves were used to decide the flow rate and response time of the actual solenoid valves bought for the testbench. Once the testbench was completed, the valves were first tested to see how well they correlated with the expected response found from the simulation. The results from this test can be found in Figure 4.57. The test was conducted using the brake booster attenuation system. The initial rise in the pressure differential was caused by the brake pedal being applied and the internal valves creating a pressure differential between the dynamic and constant pressure chambers of the brake booster. This was similar to what was done in the previous subsection. This had already been tested, and as expected, the actual brake

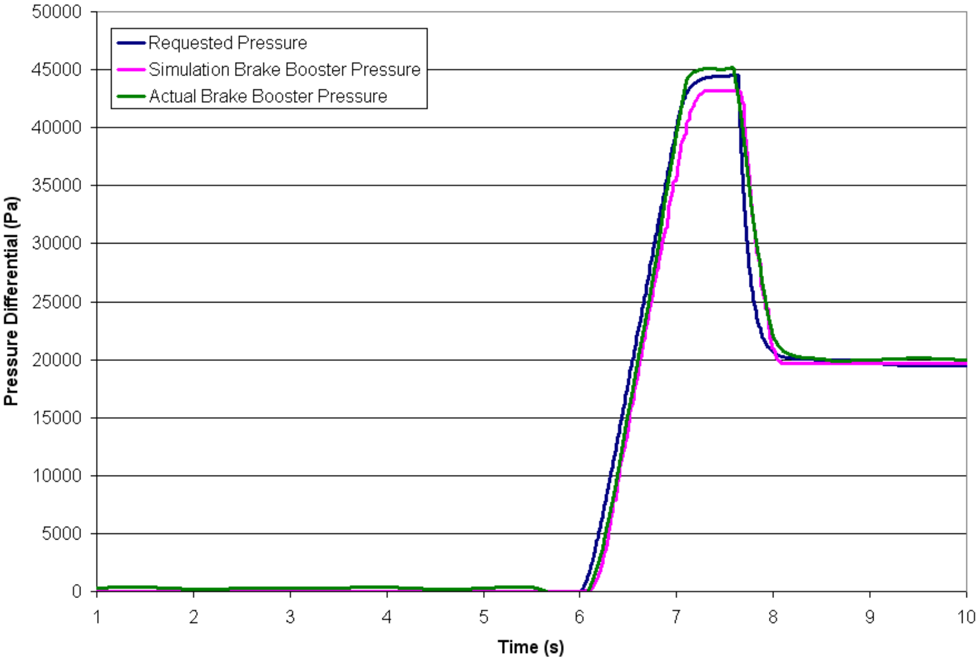

Figure 4.57: Comparison of the actual and simulation solenoid valve response

booster pressure differential followed the requested and simulation pressure differentials very well. The next step of the test involved activating the brake booster attenuation system to reduce the pressure differential using the solenoid valve. During this portion of the test, both the actual and simulation decrease in pressure differential were very similar, which confirmed that the flow rate of the actual valve and the simulation valve were similar and further work on the brake booster attenuation system could be continued.

4.6.3 Brake Booster Attenuation Comparison (Alternate I)

The first tests of the Alternate I brake booster attenuation system were conducted using typical mechanical braking requests found during the simulations. The results from the first two tests can be seen in Figures 4.58 and 4.59. Both tests showed that the actual brake booster attenuation system brake line pressure tracks the requested and simulation brake line pressures well. However, differences were seen between the actual brake line

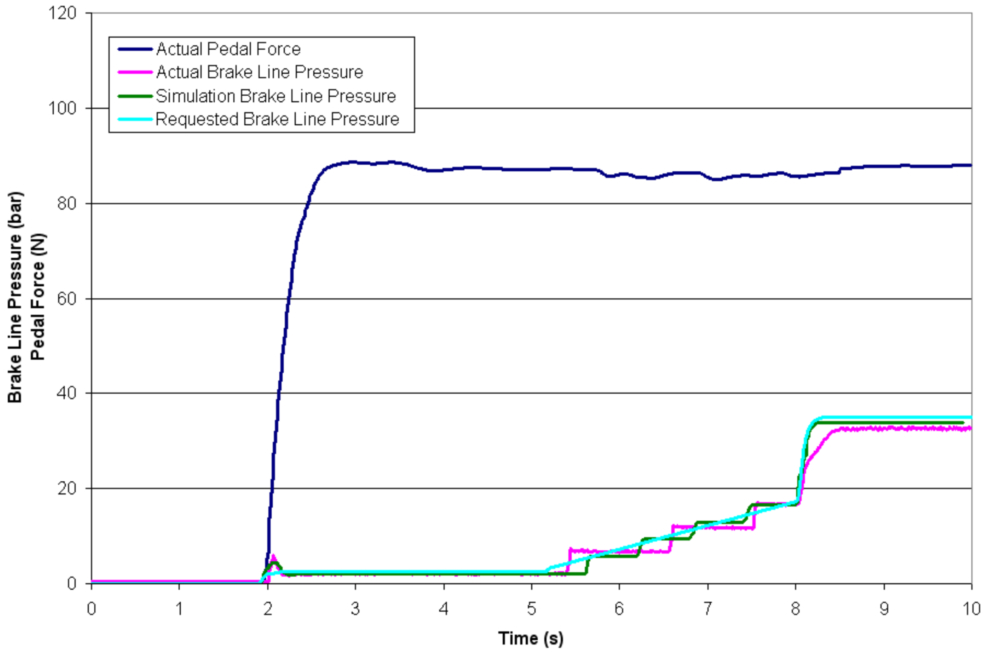

Figure 4.58: First brake booster attenuation system test

pressures and the expected brake line pressures from the simulations. From the results of the first figure during the ramp section of the control signal (from 5-8 seconds), it was observed that the actual brake line pressure followed the control signal more accurately than the simulation. The inaccuracy of the simulation brake line pressure during the ramp section of the control signal was most likely caused during the conversion of the brake pedal force into the brake line pressure in the simulation. Even though the simulation brake line pressure did not follow the control signal as well, it reacted faster by using four steps during this ramp period where the physical prototype used only three steps. The discrepancy during the step portion of the control signal (from 8-10 seconds) was most likely caused by assuming an infinite volume for the accumulator in the simulation. In reality, a 4 litre accumulator was used, which resulted in a slower change in the actual brake line pressure. Similar findings were found for the second figure.

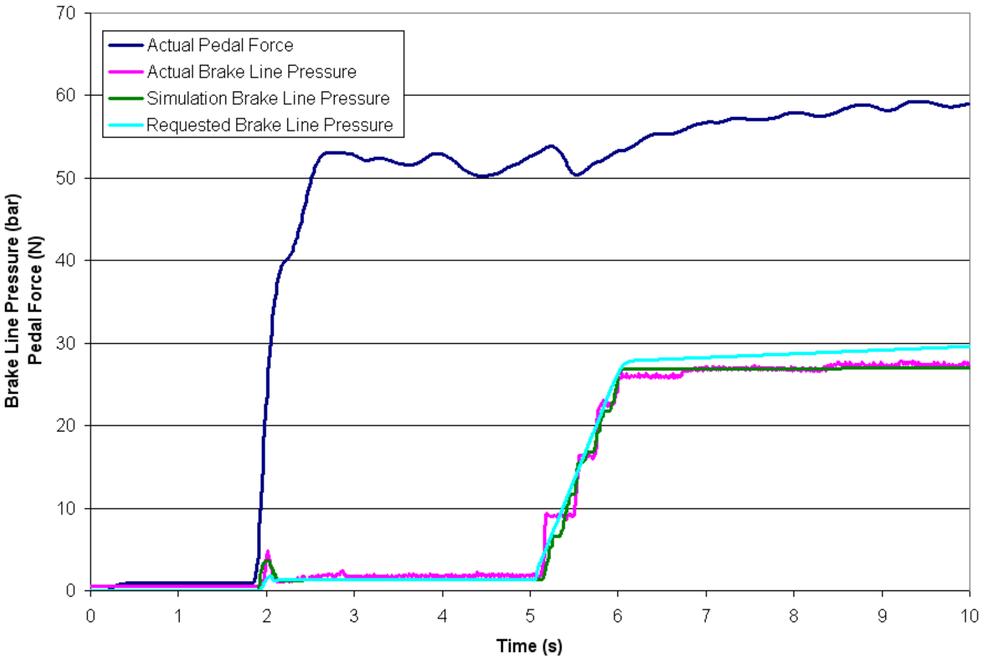

Figure 4.59: Second brake booster attenuation system test

Chapter 5

Full Scale Application to the Pacifica

5.1 Introduction

The main focus of the E03 RGB project was to convert a 2004 Chrysler Pacifica into a hybrid electric vehicle that used ultracapacitors to store energy from the regenerative braking process. The first phase of the project involved installing a 67 kW Siemens AC induction motor to the prop shaft of the standard transmission using a gear reduction of 6.52:1 [39]. This involved removing the rear driveshaft resulting in the ICE being able to drive the front wheels only. The induction motor was also able to drive the front wheels by providing torque through the back of the transmission to the front differential with a gear ratio of 1.71:1. During braking the induction motor could apply regenerative braking to the front axle through the reduction gearbox and front transaxle. An overview of the first phase of the project is shown in Figure 5.1.

5.1.1 Scaling up the System

When designing the mechanical/regenerative testbench, the mechanical and electrical torques generated were downsized to match the scale of the flywheel. In order to implement the system on a full sized vehicle, some of the components and control algorithms would have to be scaled up to match the requirements of a full sized vehicle.

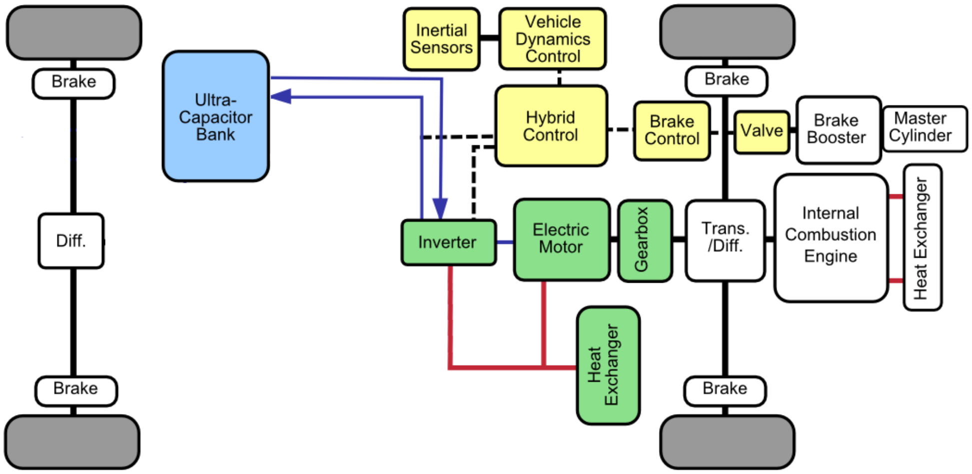

Figure 5.1: E03 RGB phase 1 overview

5.1.2 Hardware

Few modifications would be required to scale the testbbench hardware up the the Chrysler Pacifica hardware. The brake pedal, brake booster and master cylinder used on the testbench were standard automotive braking components and thus already proper size. This meant that the only hardware that would have to be scaled up to function on the the Chrysler Pacifica are the brake calipers and brake rotors. Since the Pacifica uses brakes on all four wheels adding three more brake calipers and rotors would be required. The physical dimensions of the Chrysler Pacifica brake calipers, brake rotors and tires are shown in Table 5.1 and were later used in simulation to calculate the torque generated by the braking system.

Parameter	**Value**
Rotor radius (front)	0.16 m
Rotor radius (rear)	0.14 m
Caliper piston area (front brakes)	0.003 m^2
Caliper piston area (rear brakes)	0.002 m^2

Table 5.1: Estimated properties of the brake calipers and rotors

5.1.3 Control Systems

The same control strategy used for the testbench can be used for the Chrysler Pacifica. However, the increase in the mechanical braking torque on the Pacifica and the torque increase of the electric motor used on the Pacifica will require changes to be made to the information input into the control systems. Since the scaling factor of the testbench was 1/100th of a full size vehicle, the scaling factor used to calculate the driver requested torque from the force applied to the brake pedal will have to be increased. To do this as accurately as possible a stock Chrysler Pacifica should be instrumented with a pedal force sensor and an accelerometer. The accelerometer can measure the braking force and hence braking torque which can then be correlated with the brake pedal force. Since the mechanical braking controller uses brake line pressure as a feedback to calculate torque there is also a scaling factor between the brake line pressure and the torque generated. Knowing the brake rotor radius and the brake caliper piston area, a friction coefficient can be estimated and the scaling factor that relates the braking torque with the brake line pressure can be found using Equation 5.1.

$$\begin{gathered} T_b = \mu_{pad} A_{caliper} r_{caliper} P_{mc} \\ Scaling\ Factor = \mu_{pad} A_{caliper} r_{caliper} \end{gathered} \tag{5.1}$$

For the electric motor, the parameters used in the electric motor controller will have to be replaced with the parameters for the 67 kW Siemens A 312V67 MG AC induction motor used in the Pacifica. For the overall controller, the torque curve of the Siemens motor will be required to calculate the maximum regenerative braking torque available at the current speed of the vehicle. Since the motor torque passes through two different gear reductions, this will need to be considered when calculating the torque created by the motor. Figure 5.2 shows the torque curve for the Siemens motor before the gear reductions and after the gear reductions.

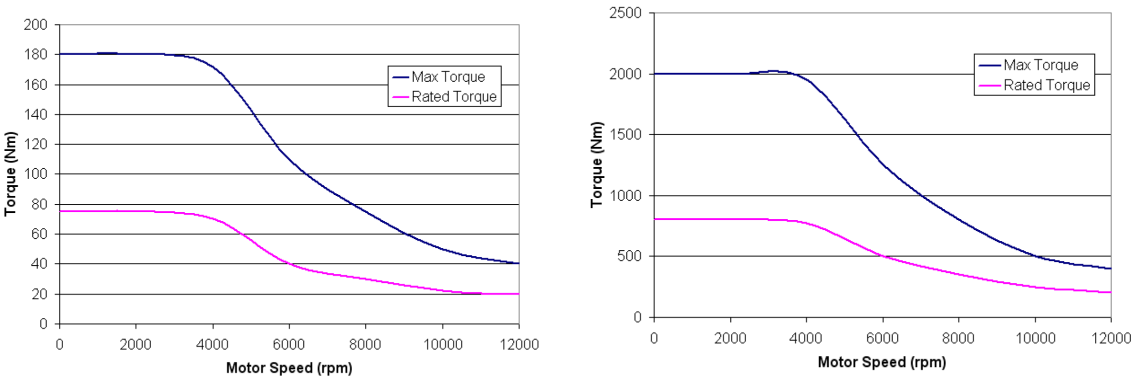

(a) Motor torque before gear reduction (b) Motor torque after gear reduction

Figure 5.2: Electric motor torque generated before and after gear reductions [39]

5.1.4 Full Vehicle Simulation

To test how the brake booster attenuation system would function in the Chrysler Pacifica, the simulation model discussed in Chapter 4 was modified to simulate the longitudinal braking of a Chrysler Pacifica. An overview of the system is shown in Figure 5.3 and the physical parameters used for the Chrysler Pacifica are shown in Table 5.2. The difference between the testbench and the Pacifica is that instead of combining the torque and applying to one flywheel, the Pacifica model combines the mechanical and regenerative braking torques and applies them to the front axle, where as it only applies mechanical braking torque to the rear axle. These braking torques are then converted to braking forces and are used to calculate the deceleration of the vehicle. There was also a linear proportioning valve modelled in the simulation that proportions the brake line pressure received by the rear brake calipers relative to the maximum pressure allowed in the system. Equation 5.2 relates the brake line pressure to the rear brake calipers (P_{rear}) with the brake line pressure from the master cylinder (P_{mc}) and the maximum pressure allowed in the system (P_{max}). Since there are four brake calipers in this simulation the mass of the brake fluid was increased, which may result in larger than required time response of the brake booster attenuation system.

$$P_{rear} = \frac{P_{max} - P_{mc}}{P_{max}} P_{mc} \tag{5.2}$$

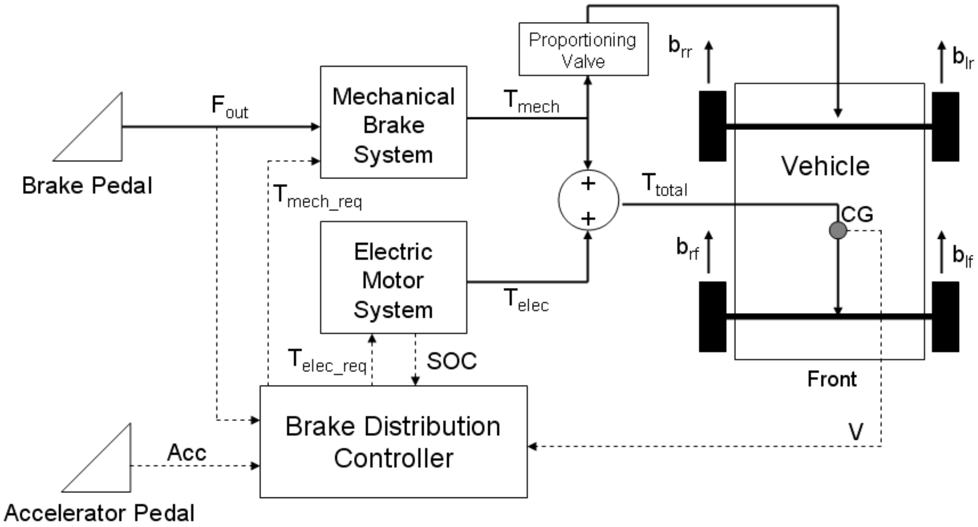

Figure 5.3: Schematic of Pacifica simulation

Parameter	**Value**
Mass (m_{veh})	2325 kg
Distance from the CG to the front axle (a)	1.359 m
Distance from the CG to the rear axle (b)	1.595 m
Height of CG (h)	0.650 m
Track width (t)	1.676 m
Effective tire radius (r_e)	0.353 m

Table 5.2: Estimated properties of the Pacifica HEV [39]

When simulating the electric motor system the internal parameters of the Siemens AC induction motor were not available to develop a full motor model. Therefore it was assumed that the motor could produce any torque within its torque curve. The purpose of the full vehicle simulations was not to optimize the power electronics or the electric motor but to demonstrate that the brake booster attenuation system could be scaled up to a full size vehicle.

5.2 Full Vehicle Brake Booster Attenuation Results

5.2.1 Time Response of Pacifica Brake System

One of the primary concerns with scaling the brake booster attenuation system up to a full sized vehicle was the time response increase caused by the additional brake line fluid used for the other three brake calipers. In order to test the time response of the system, a simulation was conducted that applied a step brake function at t= 6s that lasted until t= 8s. This simulation was the worst case scenario and assumed that someone was able to apply the brake pedal almost instantaneously. From these results the time response of the system to increase and decrease torque could be observed from the graph. The results are shown in Figure 5.4 and it was observed that the time response of the system increasing torque was 0.52 seconds and decreasing torque was 0.42 seconds. Both of these values are less than the maximum allowed time response of 0.6 seconds.

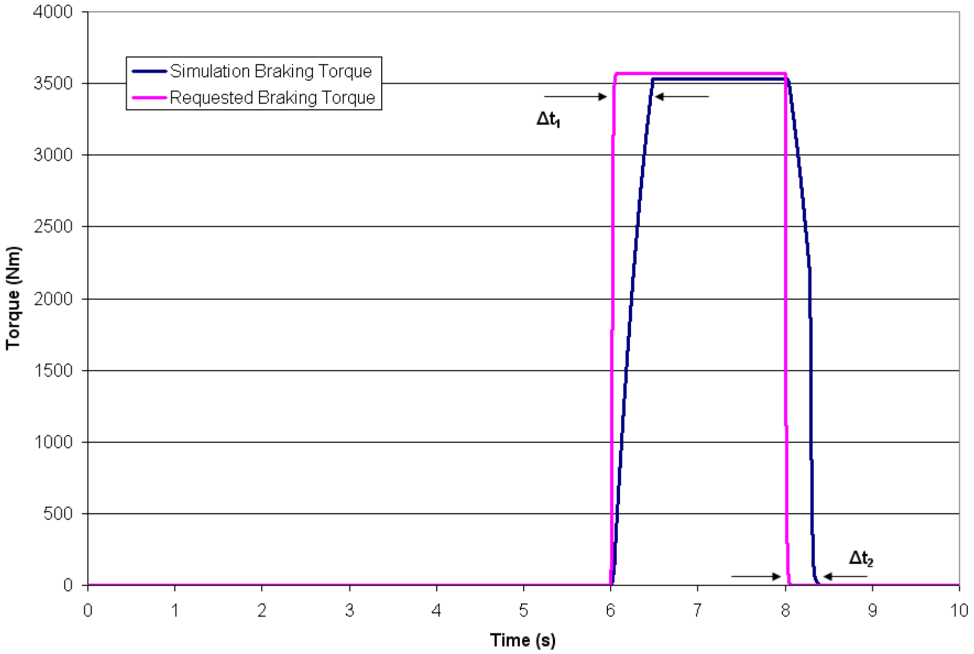

Figure 5.4: Time response of the Pacifica braking system

5.2.2 Brake Booster Attenuation System Functionality

Once it was concluded that the mechanical brake system could function within the desired time response, the next test was to evaluate how well the mechanical braking system could track a desired mechanical braking torque signal. To test the response a simulation was conducted that accelerated the Pacifica up to approximately 50 km/h in six seconds. At this point the brakes were applied and the vehicle was slowed. The mechanical braking results from this test are shown in Figure 5.5.

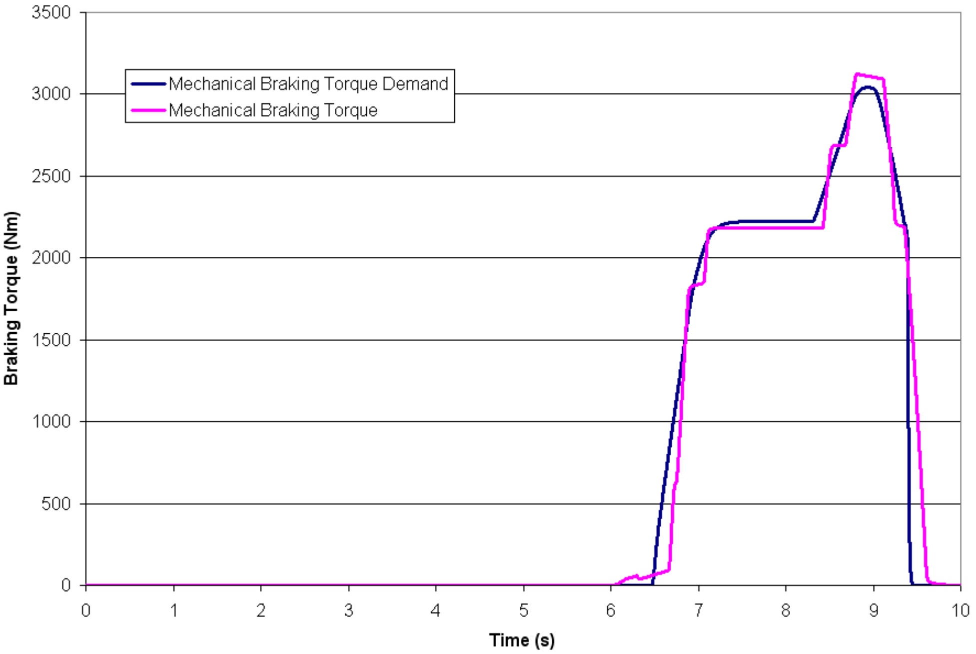

Figure 5.5: Comparison of the mechanical and desired mechanical braking torque

The figure shows that the mechanical braking torque was able to follow the desired mechanical braking torque well. The time response of the system was well within acceptable limits and the error was less than 10 percent during the main braking event.

To see how the mechanical braking torque was proportioned between the front and rear axle, Figure 5.6 was also created from the simulation. These results verified that the brake proportioning system modelled in the simulation was functioning as intended.

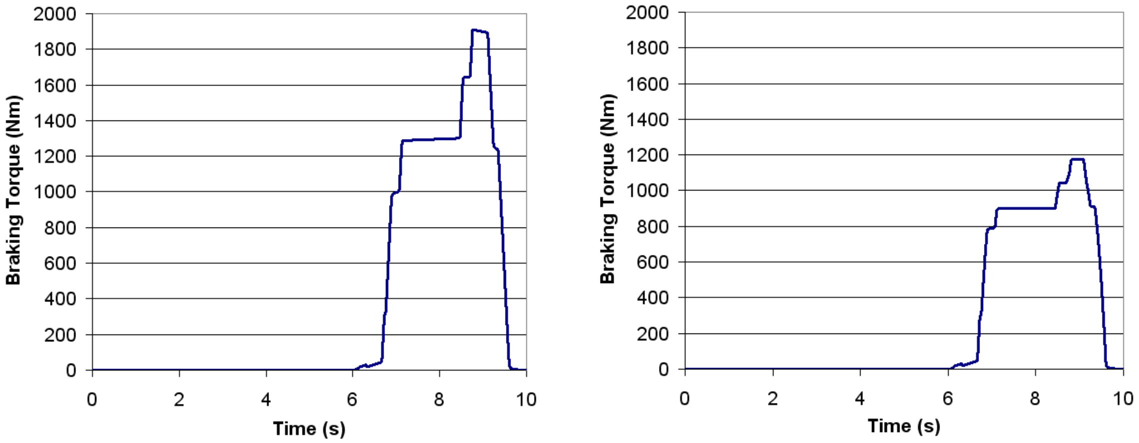

(a) Front axle braking torque

(b) Rear axle braking torque

Figure 5.6: Brake proportioning between the front and real axle

5.2.3 Blending of the Braking Systems

It is important that the regenerative braking system be transparent to the driver. To test this criteria the simulation used above was re-run. The results shown in Figure 5.7a, were used to demonstrate that the mechanical and regenerative braking torques could be blended together to follow a desired braking torque signal.

In the figure a small fluctuation can be seen during the constant torque portion of the braking event. This occurs at around nine seconds and corresponds with an increase in the mechanical braking and a decrease in the regenerative braking. To check whether or not the driver could notice these fluctuations the acceleration of the vehicle was observed. Figure 5.7b shows the velocity of the vehicle over the simulation and the acceleration experienced during braking. It has been found that the typical driver does not notice acceleration fluctuations that are less than 0.3 m/s^2 [18]. From the figure, the largest acceleration fluctuation which occurs at around nine seconds was found to be 0.18 m/s^2. This is less than the maximum value and should not be noticed by the driver.

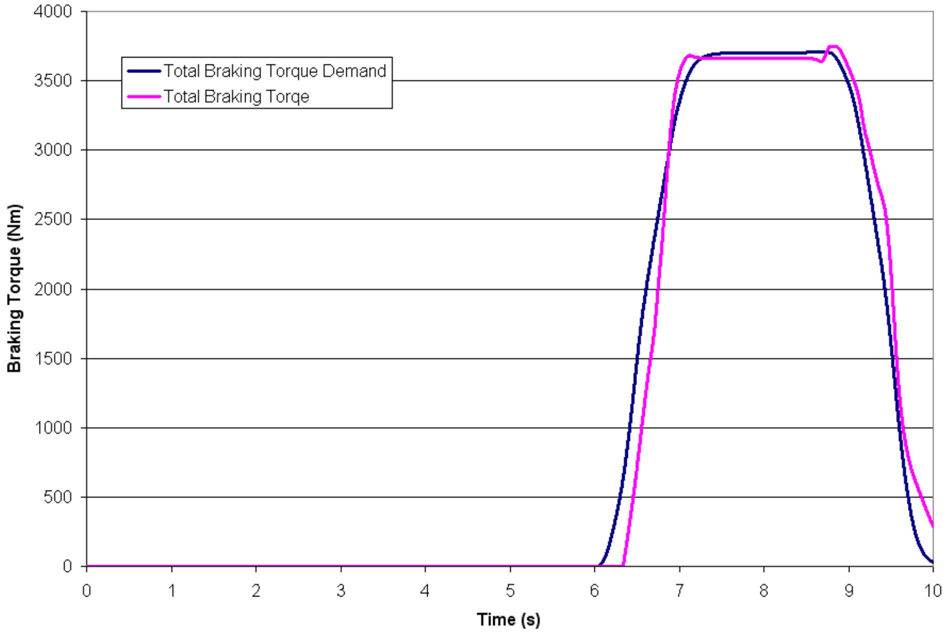

(a) Comparison between total braking torque and desired braking torque

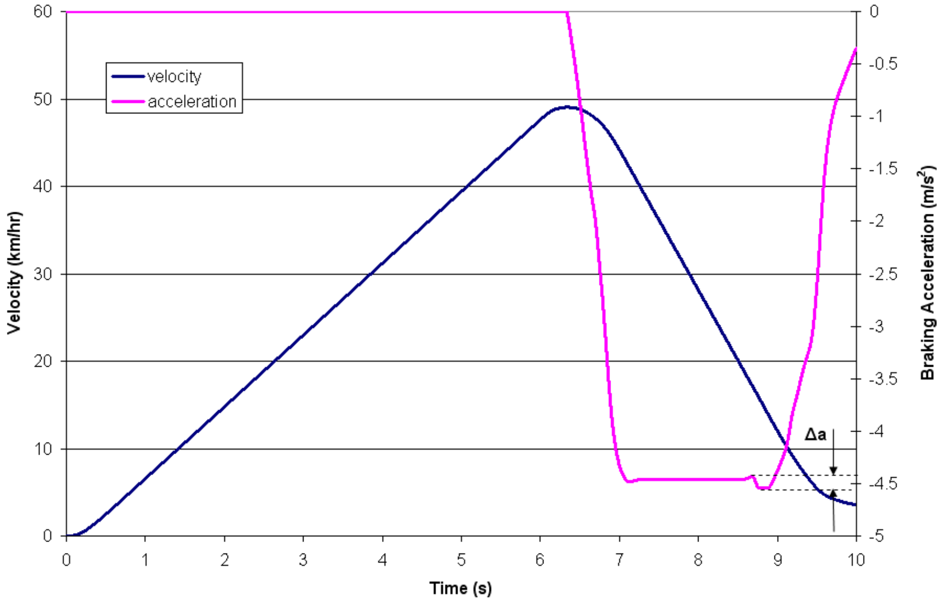

(b) Acceleration values from the simulation

Figure 5.7: Blending of the mechanical and regenerative braking systems

Chapter 6

Conclusions and Recommendations

6.1 Conclusions

Hybrid electric vehicles are an option consumers are given to reduce vehicle emissions and their annual fuel costs. However, the cost of these vehicles has a negative effect on the number sold. To improve the viability of hybrid electric vehicles, it is important to design and develop new hybrid electric systems using a systematic and cost effective process. An alternative to electro-hydraulic braking was demonstrated using physical and virtual prototyping. This brake booster attenuation system demonstrated its feasibility as one possible solution.

Through the results, it was shown that the brake booster attenuation system could meet the requirements stated in the project definition phase. The system's time response is less than the maximum value allowed, the system can attenuate the mechanical braking torque independent of the driver's pedal force and the system can be used to improve the regenerative braking efficiency of the system. It was also shown using the simulation that the concept could be scaled up and implemented in a full sized vehicle.

During this design process, creating both virtual and physical prototypes proved to be invaluable. Virtual prototypes were time and cost efficient methods of testing concepts and ideas, while the physical prototypes gave physical insight into the design. However, using the two prototypes in conjunction proved to be the most valuable aspect of the process. Virtual and physical prototypes were both used to determine feasibility of the conceptual design followed by the construction of more advanced virtual and physical prototypes to demonstrate the functionality of the system.

During the design process, both prototypes could be used in combination to improve the overall design. Results from the physical system were used to fine tune the virtual model to respond as realistically to the physical prototype as possible. By doing this, it was then possible to tune the controller of the system using the virtual prototype, which is time efficient and has tight control over the input variables. These control algorithms were then transferred to the physical prototype with a high degree of confidence and they worked as intended.

From an overall perspective, the physical prototype was a very useful design tool. It allowed for an understanding of the system that would not have been possible with just the virtual prototype. These prototypes can prove to be great educational resources for students and offer significant added value to the research. The physical prototype also demonstrated the importance of interdisciplinary cooperation and education. Integrating both mechanical and electrical systems allowed beneficial collaboration among peers from different disciplines which resulted in better understanding and development of the systems.

In conclusion, virtual and physical prototyping are cost and time efficient methods to demonstrate feasibility of a conceptual design. These prototypes can then be used as an effective method of demonstrating that the system can meet the requirements of the project definition. They can be used as a way of solving design problems that may arise during the preliminary design phase and can be easily adapted to test new concepts that may be created. These prototypes can also be used in combination as a powerful tool to validate and develop the system in an efficient and confident manner.

6.2 Recommendations

6.2.1 Improvement of the Testbench

The electric motor system of the physical mechanical/regenerative braking testbench never operated as intended. The vector control could not be implemented correctly into the system, which made regenerative braking not possible. For this reason, the mechanical braking torque and regenerative braking torque could not be blended with the physical testbench. In order to test how the transparency of the blending of the mechanical and regenerative torques, vector control will have to be implemented into the electric motor system of the physical testbench.

Alternate II was never implemented into the physical brake booster attenuation system. From the simulation results, it was concluded that the Alternate II brake booster attenuation system could track the mechanical control torque more accurately and smoothly than the Alternate I system. It would be interesting to test the brake booster attenuation system using the proportional control valves (Alternate II) to see if the results from the simulation would correlate with the physical results.

It would also be interesting to test if the solenoid valves used in Alternate I could be over-driven (operated at a frequency above the maximum frequency). This should cause the solenoid to float between the open and closed state producing a flowrate that is less than the maximum flowrate but greater than zero. If this could then be controlled, the solenoid valves could be used to simulate the proportional control valves of Alternate II.

6.2.2 Production Brake Booster Design

It is evident from the testbench that in order for the brake booster attenuation system to succeed in production-manufactured vehicles, the system needs to be redesigned as a compact electro-mechanical unit that will easily fit under the hood of a vehicle. It is recommended that a three chamber brake booster concept be created. The third chamber in the brake booster should allow for the accumulator to be packaged into the brake booster.

The volume of the constant pressure chamber should be reduced to increase the response time of the brake booster and to reduce the length of the brake booster which has been increased by the addition of the accumulator. The brake booster will function as it did on the test bench so there will be two valves required for the proper operation of the electro-mechanical brake booster.

6.2.3 Student Education

In many academic situations, physical prototypes are often not completed for either cost or time constraints. However, the author believes these physical prototypes give a physical insight into the project that can not always be obtained from simulations, and can actually be used to improve the simulation results. The physical prototypes educate students in manufacturing processes, trouble shooting and product sourcing, along with introducing the students to varied disciplines. The author strongly recommends that students create physical prototypes when possible to improve the quality of their education.

Appendix A

Matlab Simulink Models and Constants

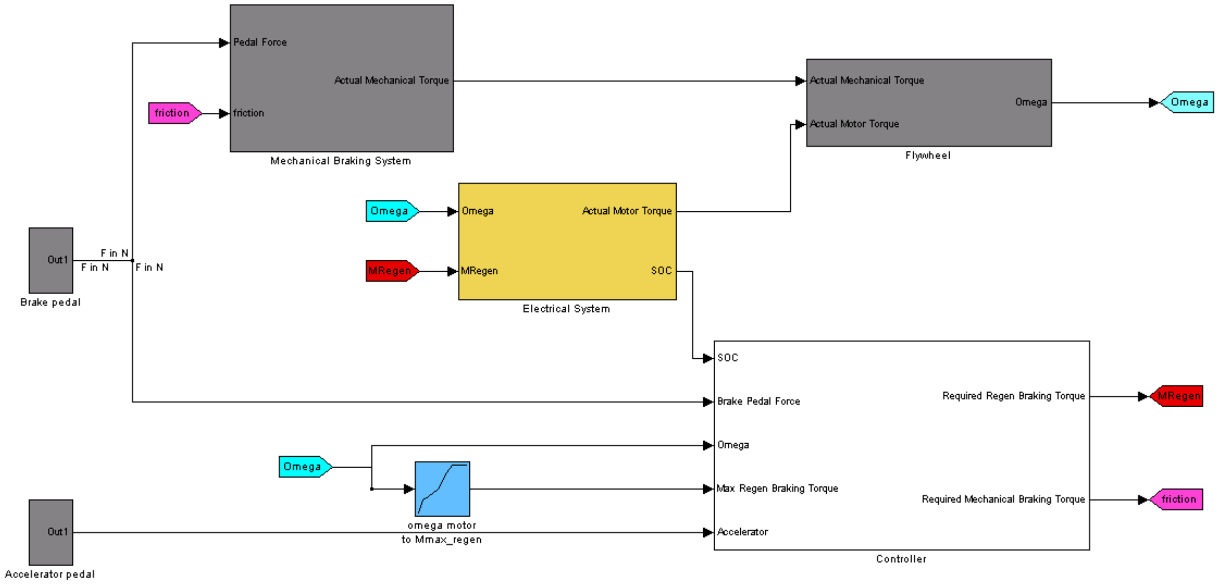

Figure A.1: Simulink model overview

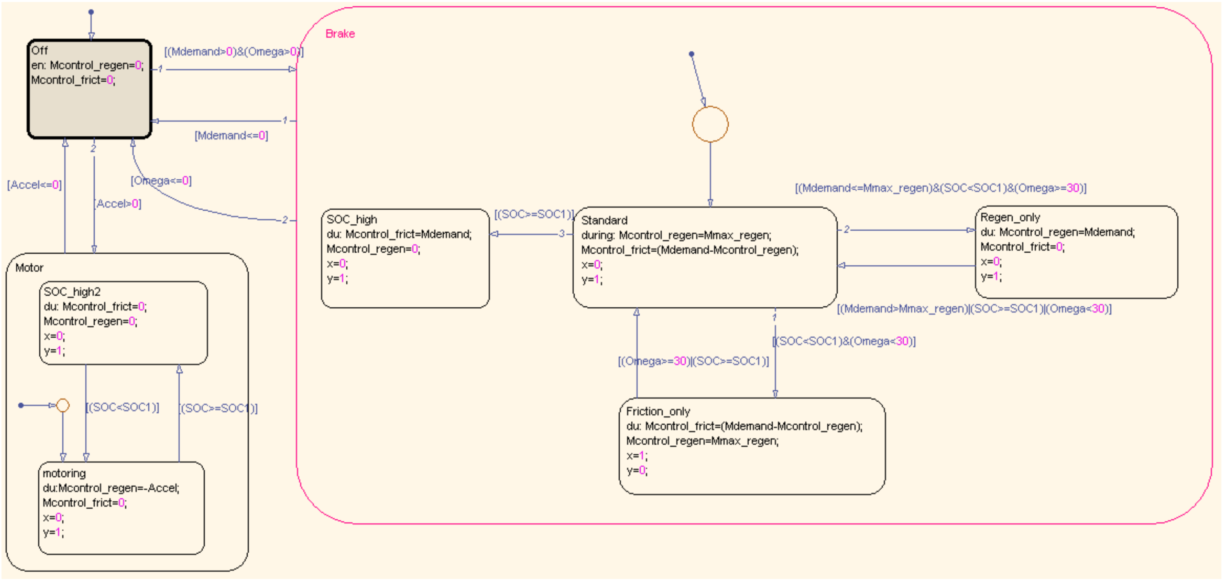

Figure A.2: Overall controller

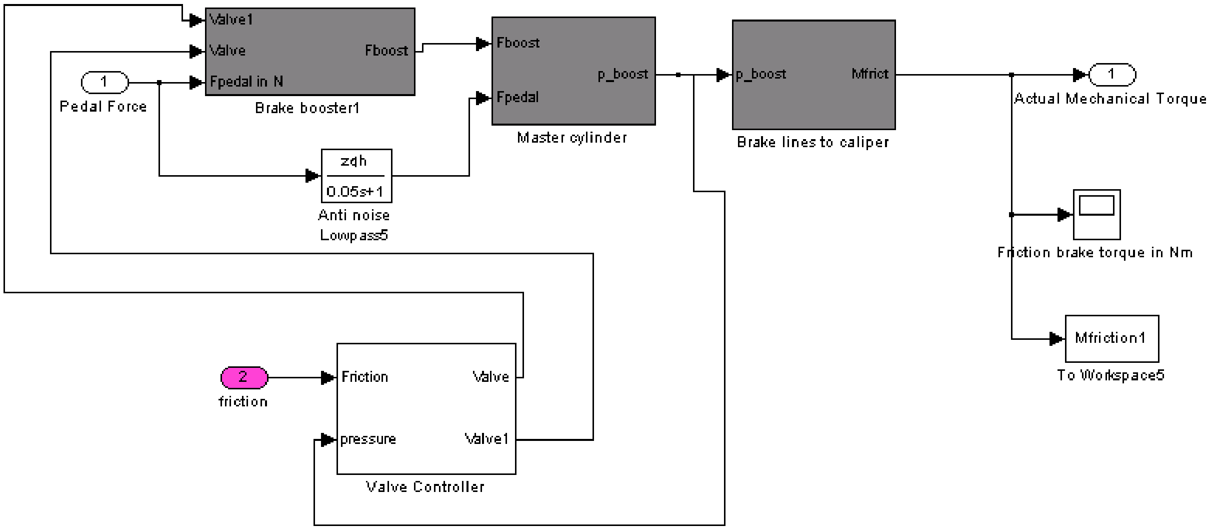

Figure A.3: Mechanical brake system overview

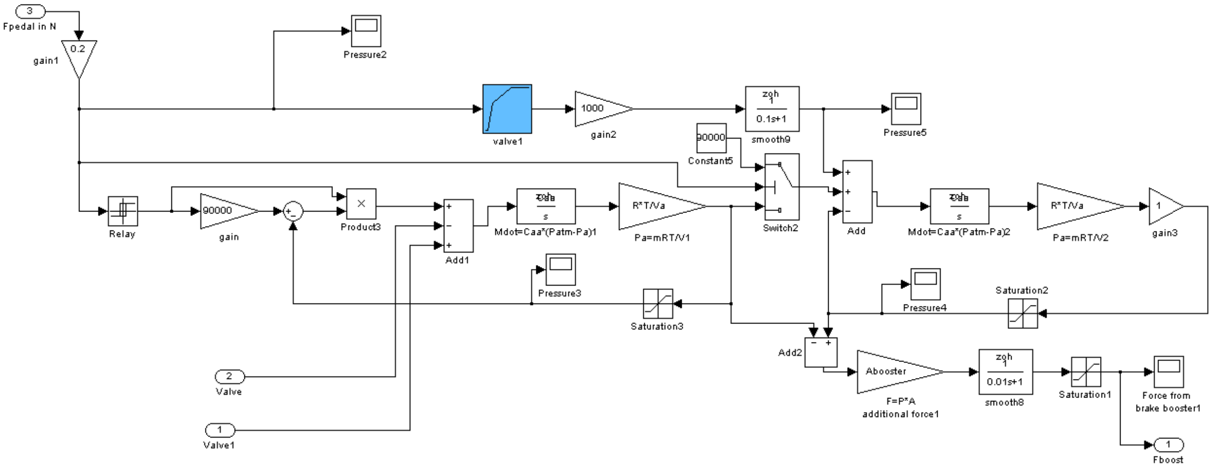

Figure A.4: Brake booster

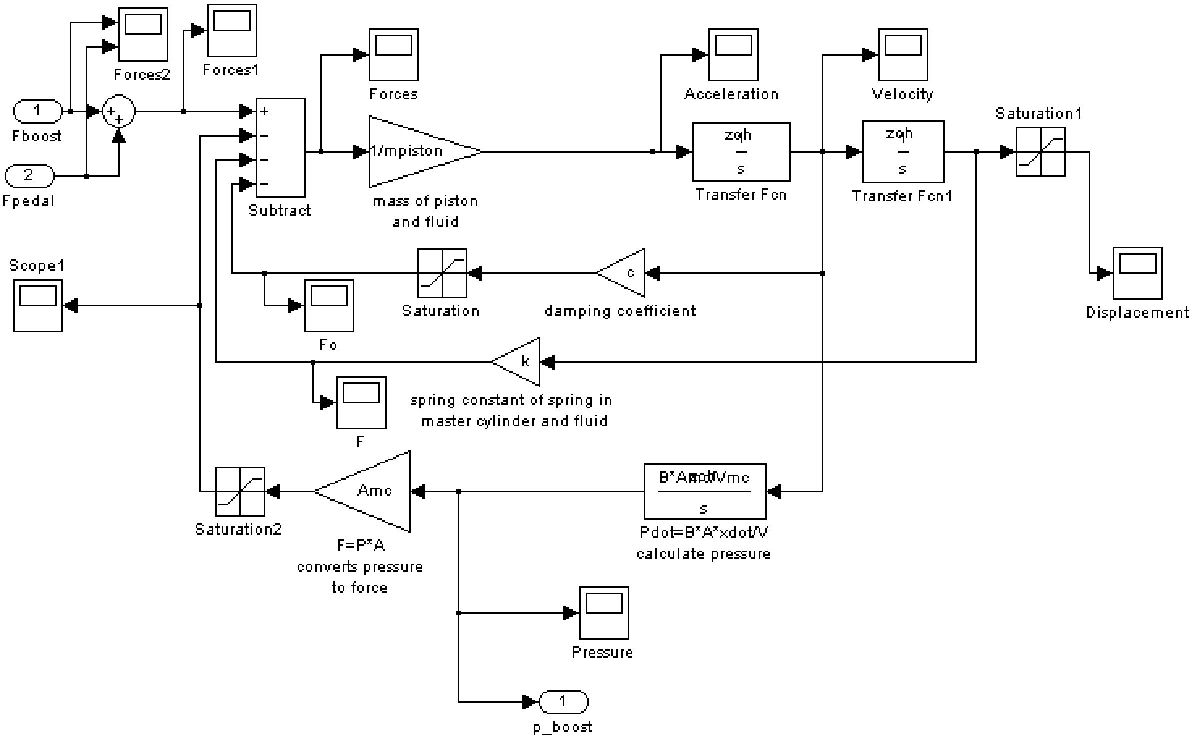

Figure A.5: Master cylinder

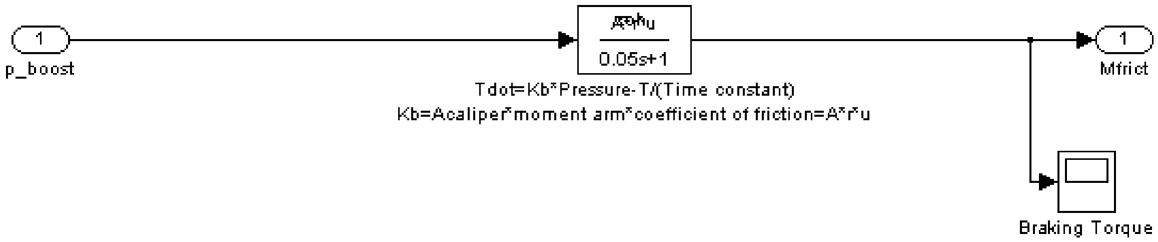

Figure A.6: Brake caliper

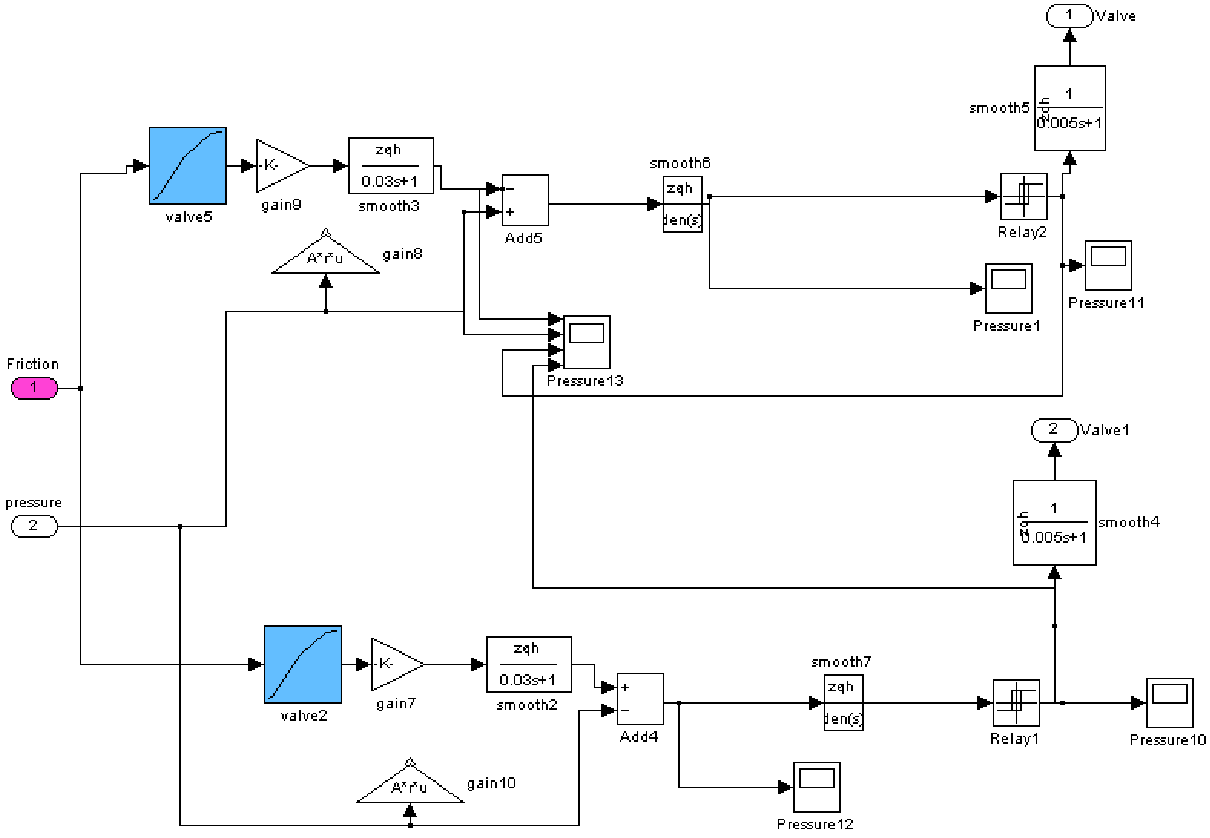

Figure A.7: Mechanical brake controller

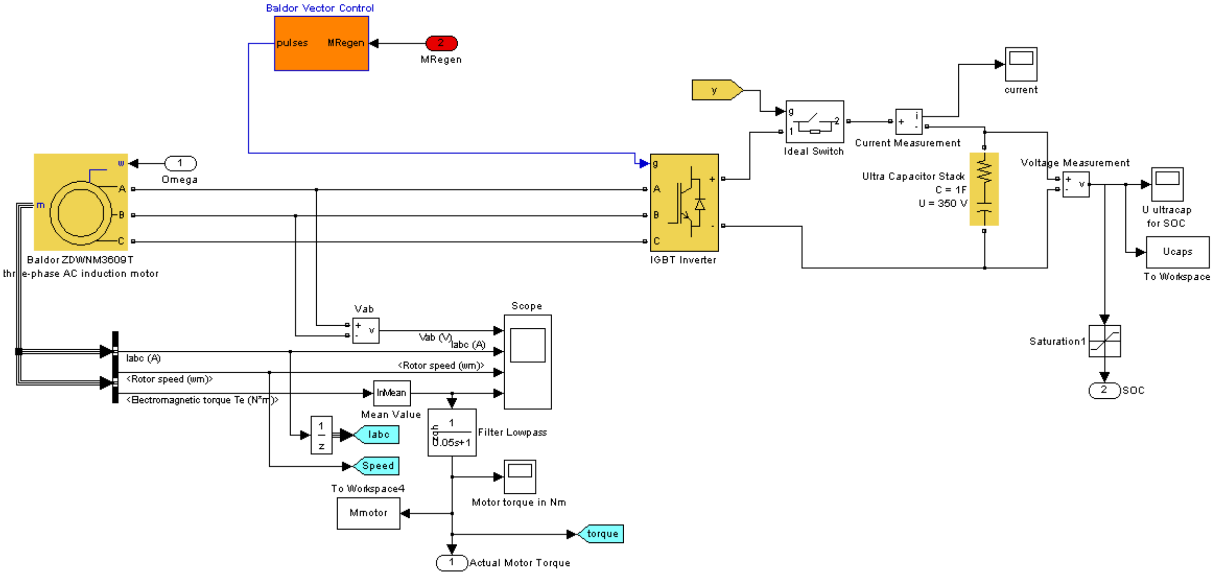

Figure A.8: Electric motor system

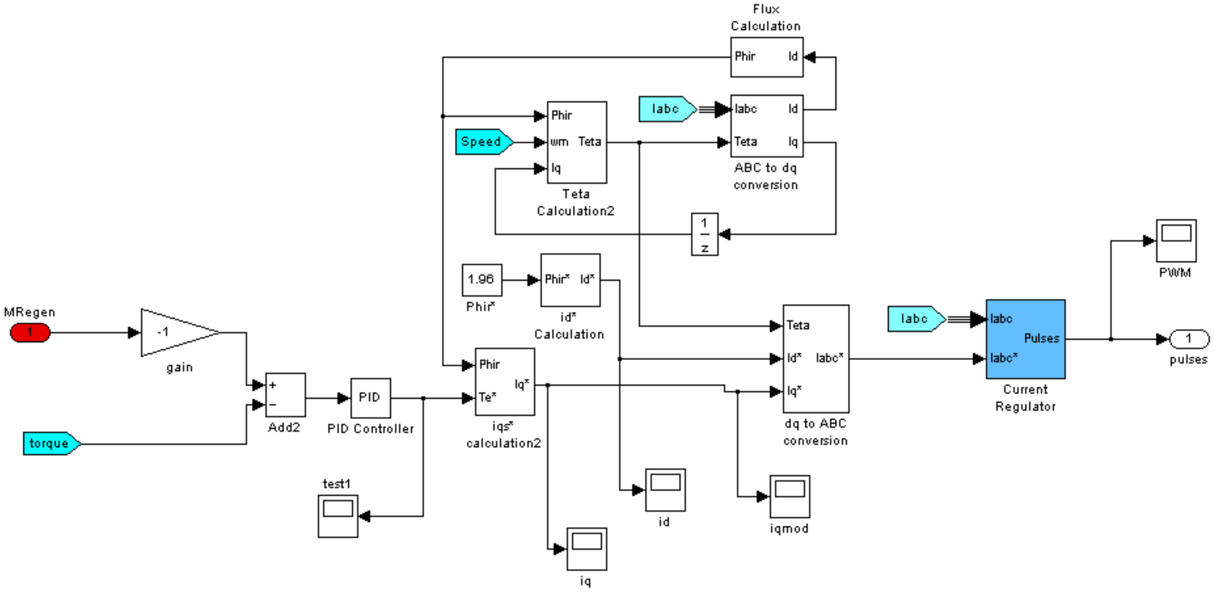

Figure A.9: Electric motor controller

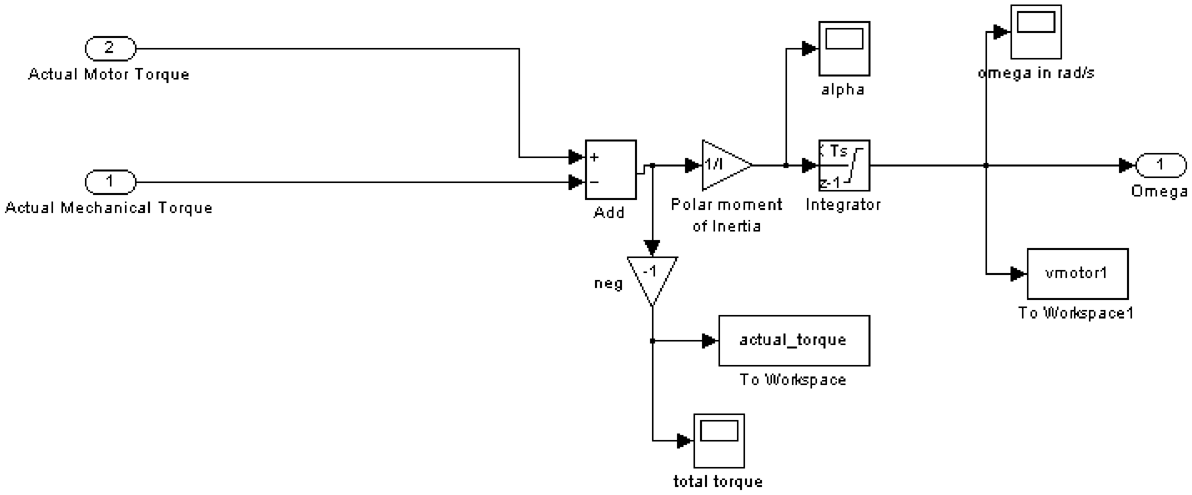

Figure A.10: Flywheel

Variable	**Value**
Amplification of pedal force ($\frac{l_a}{l_b}$)	4
Brake pedal time lag (τ_p)	0.03 s
Brake booster diaphragm area (A_d)	0.04 m^2
Ideal gas constant (R)	287.05 $\frac{Nm}{kg\ K}$
Temperature (T)	300 K
Volume of constant chamber (V_{vo})	0.008 m^3
Volume of dynamic chamber (V_{ao})	0.002 m^3
Brake fluid damping coefficient (C_{mc})	400 $\frac{N\ s}{m}$
Master cylinder spring constant (k_{mc})	100 $\frac{N}{m}$
Master cylinder piston and brake fluid mass (m_{mc})	0.5 kg
Master cylinder spring constant (k_{mc})	100 $\frac{N}{m}$
Brake fluid bulk modulus (β_{mc})	1.5 e^9 $\frac{N}{m^2}$
Master cylinder volume (V_{mc})	0.001 m^3
Brake caliper radius ($r_{caliper}$)	0.064 m
Brake pad friction coefficient (μ_{pad})	0.4
Brake fluid time lag (τ_b)	0.05 s
Flywheel and shaft polar moment of inertia (J)	2.283 kg m^2

Table A.1: Simulation constants

Appendix B

Testbench Manufacturing Drawings

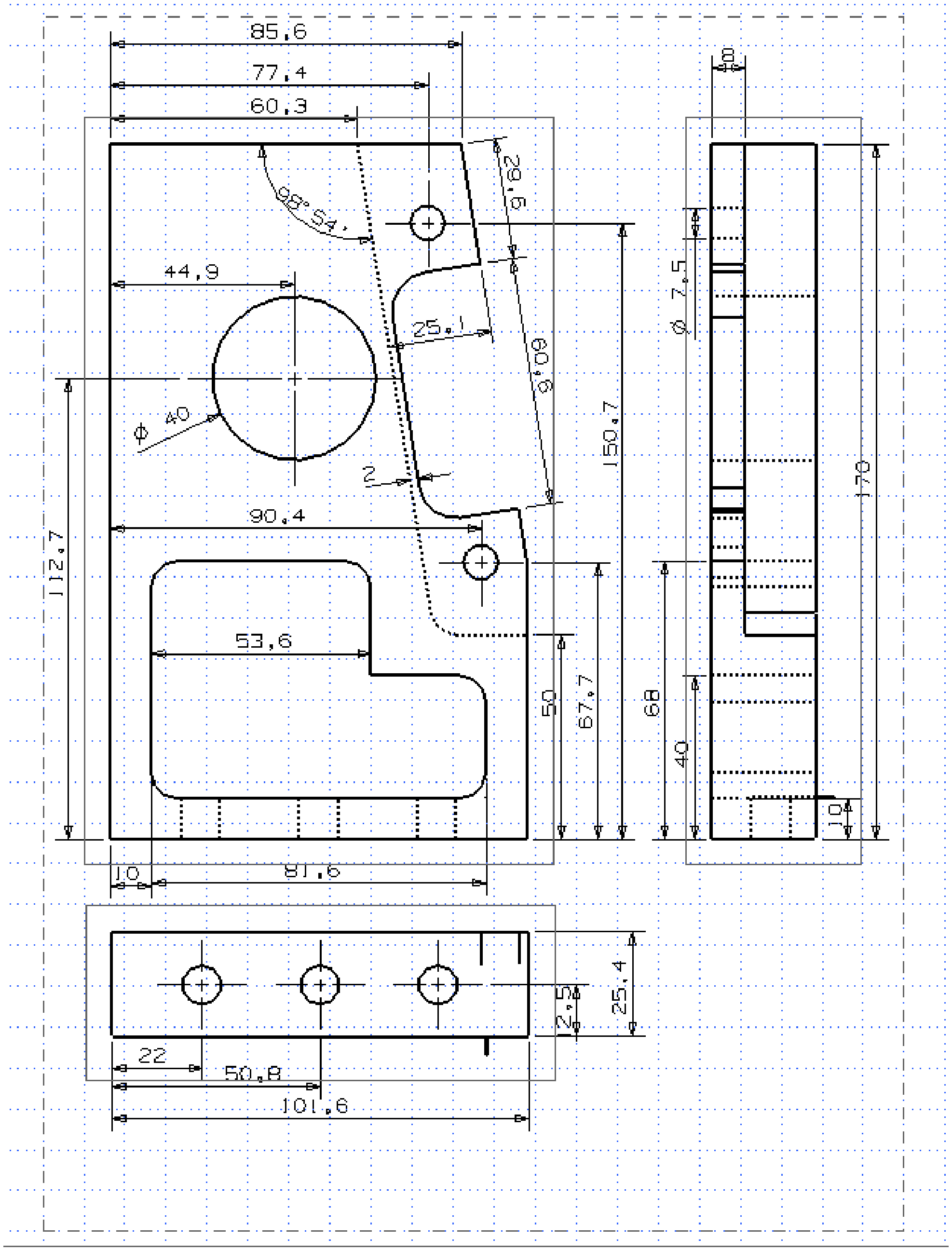

Figure B.1: Upright used to support the brake caliper

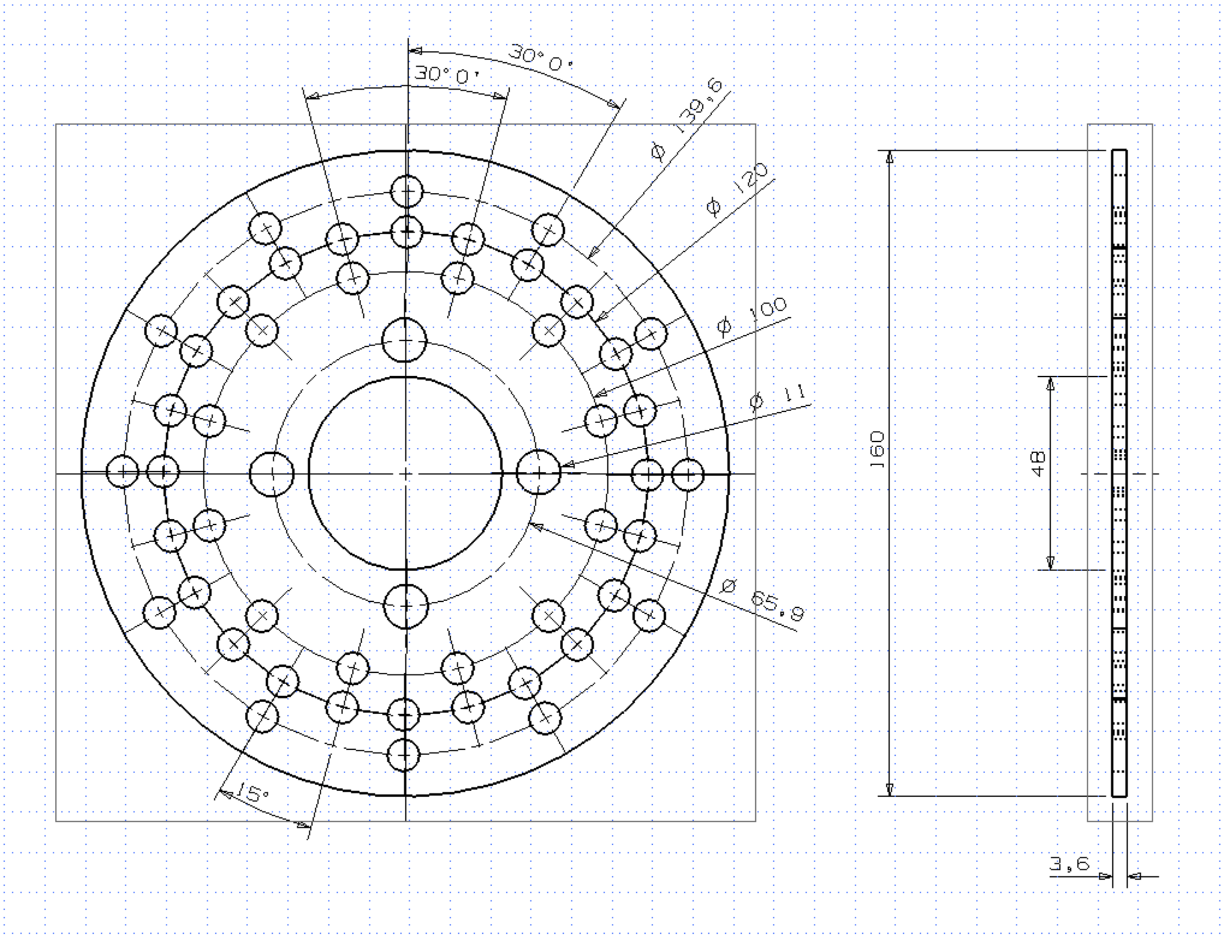

Figure B.2: Brake rotor

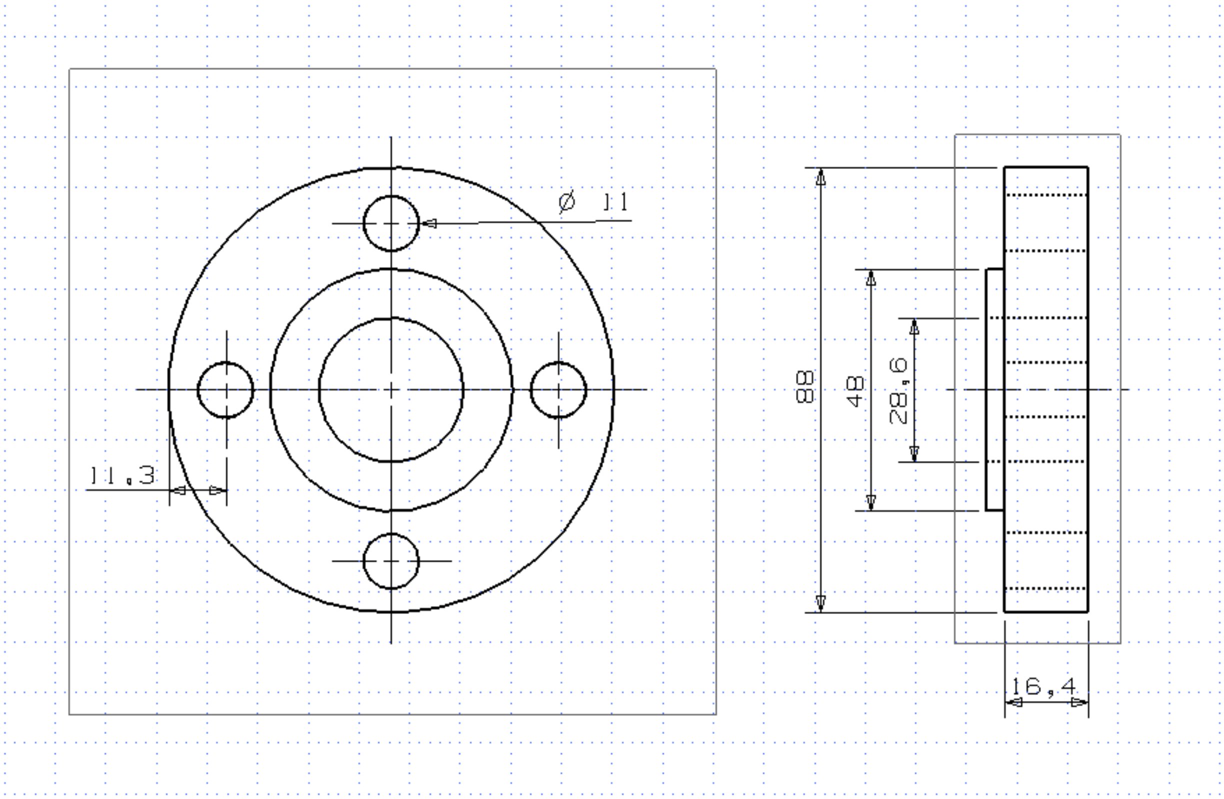

Figure B.3: Brake hub

Appendix C

Testbench Component Description

Component	**Model**	**Serial Number**
Induction Motor	Baldor ZDWNM3609T Vector	F0301238050
Ultracapacitor	Maxwell BCAP0008 Boostcap Ultracapacitor	00 9502 02 082
IGBT Inverter Module	POWEREX Intelligent Power Module PS21965-4	CM15MD-12H
Digital Signal Processor	Spectrum Digital eZdsp TMS320F2812	C2B 0709031
Multifunction I/O Device	National Instruments PCI-2024E	183032C-01
Data Acquisition System	LabJack U12 Firmware V1.100	100047118
Relay	Tyco KRPA-11DG-12	T0100640
Solenoid Valve	SMC Pneumatics VCA41A-6G-10-03N-F	0900941597563
Vacuum Pump	Hella UP28 Vacuum Pump	009217-00
Speed Sensor Converter	ETACH2-R High Speed Encoder to Analog Tachometer	0908456134
Current Sensor	Furison Electric FCS010-5V-SD	N/A
Brake Pedal Sensor	Vericom Computers, Inc. Load Cell	24110
Hydraulic Pressure Sensor	MEGADYNE PX4000C6-5KGST	L05237003
Air Pressure Sensor	Freescale MPXV6115VC6U Integrated Pressure Sensor	K0642
Throttle Position Sensor	CTS Electronic Pedal Sensor 503 Series	CTS 3642
Encoder	Baldor Optical Encoder	CC01405
Strain Gauge	Vishay Rectangular Rosette CEA-XX-125UR-350	N/A
Torque Sensor Node	MicroStrain V-Link 2.4 GHz Wireless Voltage Node	
Torque Sensor Base Station	MicroStrain Agile-Link 2.4 GHz Wireless Base Station	
Bearing	SealMaster NP-18T	P-105

Table C.1: Components of the testbench

References

[1] Y. Aoki, K. Suzuki, H. Nakano, K. Akamine, T. Shirase, and K. Sakai. Development of hydraulic servo brake system for cooperative control with regenerative brake. *SAE Technical Paper Series*, 01(0868), 2007.

[2] Electric Drive Transportation Association. Hybrid sales figures and tax incentives. Available on: `http://www.electricdrive.org/index.php?tg=articles&topics=7`, 2007.

[3] Autoshop 101. *Brake Booster*, 2007.

[4] I. Batarseh. *Power Electronic Circuits.* John Wiley and Sons, Ltd., West Sussex, England, 2003.

[5] W.K. Chen. *The Electrical Engineering Handbook.* Elsevier Academic Press, Inc., San Diego, California, 2005.

[6] S.R. Cikanek and K.E. Bailey. Regenerative braking system for a hybrid vehicle. *American Control Conference*, 2002.

[7] Baldor Electric Company. Baldor AC motor specification page. Available on: `http://www.baldor.com/products/ac_motors.asp`, 2007. Date Acessed: October 26, 2007.

[8] Fastenal Company. Fastenal hex head specification page. Available on: `http://www.fastenal.com/web/home.ex`, 2007. Date Acessed: October 26, 2007.

[9] Swagelok Company. Valve sizing. Technical report, Swagelok Company, 2002.

[10] B.E. Conway. *Electrochemical Supercapacitors.* Luwer Academic / Plenum Publishers, New York, New York, 1999.

[11] NEC Corporation. An introduction to vector control of AC motors using the V850. Application note, NEC Corporation, 2002.

[12] M. Ehsani, Y. Gao, S.E. Gay, and A. Emadi. *Modern Electric, Hybrid Electric, and Fuel Cell Vehicles - Fundamentals, Theory, and Design.* CRC Press, Ltd., Boca Raton, Florida, 2003.

[13] Bluestar Engineering. 35 Kingsbridge Garden Circle, Unit: 1014, Mississauga, Ontario. L5R 3Z5.

[14] G. Genta. *Motor Vehicle Dynamics: Modeling and Simulation.* World Scientific, Warrendale, Pennsylvania, 2004.

[15] J.C. Gerdes and J.K. Hedrick. Brake system requirements for platooning on an automated highway. *American Control Conference*, 1996.

[16] R. Bosch GmbH. *Automotive Handbook 7th Edition.* Robert Bosch GmbH, Plochingen, Germany, 2007.

[17] H. Heisler. *Vehicle and Engine Technology.* Butterworth-Heinemann, Woburn, Massachusetts, 1999.

[18] R. Hodkinson and J. Fenton. *Lightweight Electric / Hybrid Vehicle Design.* Reed Education and Professional Publishing Ltd., Woburn, Massachusetts, 2001.

[19] I. Husain. *Electric and Hybrid Vehicles - Design Fundamentals.* CRC Press, Inc., New York, New York, 2003.

[20] HybridCars.com. Cars. Available on: `http://www.hybridcars.com/cars.html`, 2007.

[21] The MathWorks Inc. Design and simulate state machines and control logic. Available on: `http://www.mathworks.com/products/stateflow/`, 2007. Date Acessed: September 14, 2007.

[22] W.D. Jonner, H. Winner, L. Dreilch, and E. Schunck. Electrohydraulic brake system - the first approach to brake-by-wire technology. *SAE Technical Paper Series*, (960991), 1996.

[23] Keystone Manufacturing. *TruKey Shafting*, 2007.

[24] M. Kiers. Automotive regenerative braking utilizing electrochemical capacitor energy storage. Master's thesis, University of Waterloo, 2004.

[25] J. Larminie and J. Lowry. *Electric Vehicle Technology Explained*. John Wiley and Sons, Ltd., West Sussex, England, 2003.

[26] J. Lee. Rotating inertia impact on propulsion and regenerative braking for electric motor driven vehicles. Master's thesis, Virginia Polytechnic Institute and State University, 2005.

[27] J. Lepka and P. Stekl. 3-phase AC induction vector control - design of motor control application. Application note, Freescale Semiconductor, 2005.

[28] R. Limpert. *Brake Design and Safety*. Society of Automotive Engineers, Inc., Danvers, Massachusetts, 1999.

[29] D.B. Maciuca, J.C. Gerdes, and J.K. Hedrick. Automatic braking control for ivhs. Technical report, University of California, Berkeley, 2003.

[30] D.B. Maciuca and J.K. Hedrick. Advanced nonlinear brake system control for vehicle platooning. Technical report, University of California, Berkeley, 2003.

[31] A. Masrur and C. Mi. Sae world congress. In *Fundamentals of Hybrid Electric Vehicles Seminar*, 2007.

[32] Inc. Maxwell Technologies. Electric double layer capacitor: Boostcap ultracapacitor. Technical report, Maxwell Technologies, 2002.

[33] S.B. Lambert M.I. Marei, S.J. Samborsky and M.M.A. Salama. IEEE vehicle power and propulsion conference (VPPC). In *On the Characterization of Ultracapacitor Banks Used for HEVs*, 2006.

[34] E. Michels. US patent 5711204: Electronically controlled brake booster and method of operation. Available on: `http://www.google.com/patents?vid=USPAT5711204/`, 1998. Date Acessed: December 8, 2007.

[35] J.M. Miller. *Propulsion Systems for Hybrid Vehicles.* The Institution of Engineering and Technology, London, England, 2004.

[36] E. Nakamura, M. Soga, A. Sakai, A. Otomo, and T. Kobayashi. Development of electronically controlled brake system for hybrid vehicle. Technical report, Toyota Motor Corporation, 2002.

[37] R.L. Norton. *Machine Design: An Integrated Approach.* Pearson Prentice Hall, Upper Saddle, New Jersey, third edition edition, 2006.

[38] AUTO21 Network Centre of Excellence. AUTO21 network centre of excellence - home. Available on: `http://www.auto21.ca/home_e.html`, 2007.

[39] E. Oh. Vehicle dynamics controller for a hybrid electric vehicle. Master's thesis, University of Windsor, 2005.

[40] Inc. Omega Engineering. Solenoid valves for process applications. Available on: `http://www.omega.com/techref/pdf/Solenoid_Valve_Select.pdf`, 2007. Date Acessed: September 26, 2007.

[41] M. Panagiotidis, G. Delagrammatikas, and D. Assanis. Development and use of a regenerative braking model for a parallel hybrid electric vehicle. *SAE Technical Paper Series*, 01(0995), 2000.

[42] PBR. *Hydraulic Brake System Guide*, 2007.

[43] H. Raza, Z. Xu P. Ioannou, and B. Yang. Modeling and control design for a computer controlled brake system. Technical report, Institute of Transportation Studies, 1995.

[44] R.Q. Riley. *Alternative Cars in the 21st Century.* SAE International, Warrendale, Pennsylvania, 2003.

[45] H.P. Schoner. Automotive mechatronics. *Control Engineering Practice*, 12:1344–1351, 2004.

[46] Seal Master. *Seal Master - Gold Bearing Products*, 2007.

[47] J.E. Shigley, C.R. Mischke, and R.G. Budynas. *Mechanical Engineering Design*. McGraw-Hill Companies, Inc., New York, New York, seventh edition edition, 2004.

[48] D.E. Smith, J.W. Miller, and D.K. Irick. Challenge X control strategy development. Technical report, University of Tennessee, 2005.

[49] S.Stark. Design and simulation of a regenerative braking test bench control system. Master's thesis, University of Waterloo and University of Applied Sciences Karlsruhe, 2007.

[50] P. Stekl. Washing machine three-phase AC induction motor drive. Application note, Freescale Semiconductor, 2006.

[51] Fluid Automation Systems. Kv flow factor. Available on: `http://www.fas.ch/index.asp?Langue=english`, 2007. Date Acessed: September 26, 2007.

[52] P.C. Todd. Snubber circuits: Theory, design and application. Technical report, Texas Instruments Incorporated, 2001.

[53] R.E. Uhrig. Using plug-in hybrid vehicles to drastically reduce petroleum-based consumption and emissions. *The Bent of Tau Beta Pi*, 2005.

[54] D.G. Ulman. *The Mechanical Design Process*. The McGraw-Hill Companies, Inc., New York, NY, 2003.

[55] M.H. Westbrook. *The Electric and Hybrid Electric Car*. The Institution of Electrical Engineers, London, England, 2001.

[56] J.S. Wilson. *Sensor Technology Handbook*. Elsevier Academic Press, Inc., San Diego, California, 2005.

[57] M.C. Wu and M.C. Shih. Simulated and experimental study of hydraulic anti-lock braking system using sliding-mode PWM control. *Mechatronics*, 13:331–351, 2003.